1-1-2013

The X-Ray and Spectropolarimetric View of Mass Loss and Transfer in Massive Binary Stars

Jamie Renae Lomax
University of Denver

THE X-RAY AND SPECTROPOLARIMETRIC VIEW OF MASS LOSS AND TRANSFER IN MASSIVE BINARY STARS

A Dissertation

Presented to

the Faculty of Natural Sciences and Mathematics

University of Denver

In Partial Fulfillment

of the Requirements for the Degree

Doctor of Philosophy

---

by

Jamie R. Lomax

August 2013

Advisor: Dr. Jennifer L. Hoffman

Author: Jamie R. Lomax
Title: The X-ray and Spectropolarimetric View of Mass Loss and Transfer in Massive Binary Stars
Advisor: Dr. Jennifer L. Hoffman
Degree Date: August 2013

Abstract

The majority of massive stars are members of binary systems. In order to have a better understanding of their evolutionary pathways, the mass and angular momentum loss from massive binaries needs to be well understood. Self consistent explanations for their behavior need to be valid across many wavelength regimes in order to illuminate key phases of mass loss to completely determine how it affects their evolution. In this dissertation I present the results of X-ray and specropolarimetric studies on one Roche-lobe overflow binary (β Lyr) and two colliding wind binaries (V444 Cyg and WR 140).

In β Lyr a repeatable discrepancy between the secondary eclipse in total and polarized light indicates that an accretion hot spot has formed on the edge of the disk in the system. This hot spot may also be the source of the bipolar outflows within the system. The existence of a hot spot and its relationship to bipolar outflows is important in understanding the mass transfer dynamics of Roche-lobe overflow binaries.

The absorption of the 2.0 keV spectral fit component in V444 Cyg suggests that the shock has a large opening angle while analysis of the X-ray light curves places the stagnation point farther away from the O star than theoretically expected. Combining this with evidence of polarimetric variability in V444 Cyg's optical emission lines shows that the effects of radiative inhibition or braking are significant for this close binary and may be important in other colliding wind systems.

Long term X-ray monitoring of the shock formed by the winds in WR 140 shows conflicting evidence for unexpected intrinsic hard X-ray emission. Spectral analysis shows that the low energy thermal tail is causing the observed higher energy emission. On the other hand, light curve analysis of the absorption feature near periastron passage suggests that there may be intrinsic hard X-ray emission from the system. WR 140's polarimetric behavior is consistent with the formation of dust near periastron passage, better polarimetric monitoring of the system is needed.

The work presented in this dissertation is one small step toward a better understanding of the processes involved in mass loss in binary systems. Continued studies of these three objects, in addition to other important systems, will provide important new constraints on the mass loss structures that influence the future evolution of massive binary systems.

Acknowledgements

I would like to first acknowledge my adviser, Dr. Jennifer L. Hoffman, for teaching me how to be a scientist and introducing me to the world of optical spectropolarimetry. Her guidance, support, and encouragement throughout my graduate student years has been exceptional. I have been fortunate to have my dissertation work supported through the NASA Harriett G. Jenkins Pre-doctoral Fellowship Program and Sigma Xi's Grants-in-Aid of Research Program. These programs afforded me many opportunities which undoubtedly strengthened my dissertation in numerous and immeasurable ways: two summers at NASA's Goddard Space Flight Center and several observing trips. I am indebted to my NASA mentor, Dr. Michael F. Corcoran, for teaching me the basics of X-ray astronomy, and Dr. Yael Nazé for her support and introducing me to Belgian chocolate and Liège waffles. My dissertation committee, Drs. Jennifer L. Hoffman, Alvaro Arias, Robert Stencel, Toshiya Ueta, and Michael F. Corcoran, has offered many helpful suggestions for my research, dissertation, and career over the years. My friends deserve a special thanks since without their support my graduate student experience would have been much less enriching. Through the efforts of my ski sister Alexa Hart I am now a fan of tea and have had more fun times than I can recount. Kathy Geise was always around for support and guidance. Without Azure Avery I'd have less sanity, less bacon, and possibly a few less images of a tooth in my life. I would like to thank Luke Sawle, Dain Bassett, AJ Sigdel, Leah Huk, and Rachael Tomisino for their conversations and laughs. Finally, I am most and forever grateful to my parents, James and Candace Lomax, for their endless love and support. I love you!

Contents

List of Tables

List of Figures

Chapter 1

Introduction

1.1 Why Massive Binary Stars?

Up to 70% of all massive (a star with initial mass greater than approximately 8 $M_{\odot}$) stars are members of binary systems where their evolution will be strongly affected by their companion at some point in their lives (Sana et al. 2012). Between 30 and 50% of all massive binaries are members of close systems (Podsiadlowski et al. 1992) in which the stars are close enough to interact (initial orbital periods under 1500 days), allowing them to exchange and lose material through mass streams, accretion, and stellar winds (Sana et al. 2012). Not only are these interactions important to the future evolution of binary systems, affecting all future stages of evolution (e.g. the development of common envelopes and novae; their evolution to Wolf-Rayet and X-ray binaries; and the type of supernovae they will eventually explode as), but they also play a key role in the chemical evolution of the interstellar medium (ISM) because massive stars are the only source of elements heavier than iron (de Mink et al. 2009; 2010). However, the roles of different binary evolution

scenarios remain poorly understood due to a lack of observational measurements (Sana et al. 2012). Additionally, our inadequate understanding of mass loss processes and rates further complicates the issue for systems with strong stellar winds. These problems hinder our ability to fully understand how massive binary systems inject and replenish material in the ISM and to accurately determine the progenitor stars of different supernova types.

1.1.1 A Brief Overview of Massive Single Star Evolution

The exact lower mass cut off for massive stars is dependent on a many parameters. Besides mass, metalicity and rotation rate cause it to be somewhere in the 7-11 $M_{\odot}$ range (Poelarends et al. 2008). As long as a star meets this initial lower mas cut off it will end its life as a supernova. However, in binary systems the lower limit is more ambiguous since their interactions play a large and important roll in their mass loss via shell stripping (discussed in Section 1.4) during Roche-lobe overflow (Wellstein et al. 2001).

These stars start their lives on the main-sequence, where they spend millions of years burning hydrogen into helium in their core. Once the core hydrogen has been exhausted, the star cools and contracts. This contraction then heats a shell of material around the core and ignites that hydrogen. This causes the star to then expand and slowly heat up. Eventually, temperatures are high enough to ignite the helium core and burn it into carbon. Helium core burning occurs for approximately 10% of the time the star was on the main-sequence. This process repeats and continues; the carbon core will burn to neon which will burn into oxygen, then silicon before finishing at an inert iron core. Each successive core burning takes less time than the last (carbon $10^3 - 10^4$ years; neon $10^2 - 10^3$ years; oxygen less than a year).

By the time silicon burns the timescale to form the iron core is a matter of days. At this point iron is incapable of undergoing fusion to form a new core because it takes energy, instead of releasing it, to form another core. Since core burning has stopped, energy is no longer being injected into the outer layers of the the star. The star can no longer hold itself up and a catastrophic, sudden collapse occurs where the star goes supernova.

This simplified view of massive star evolution is complicated by several important mechanisms. Rotation of massive starts can affect their evolution in several ways. First, rotation reduces luminosity and the central temperature of a star while increasing its central density (Sweet & Roy 1953, Roxburgh 2004). This is important since the central temperature must reach certain levels to burn each successive core. Eddington-Sweet flows and shear instabilities, which do not appear in non-rotating stars, are important mechanisms for the transport of energy, matter, and angular momentum throughout a massive star (Meynet & Maeder 2000, Heger et al. 2000) and are brought on by rotation. In fact, rotational mixing was added to massive star models when some main-sequence stars were discovered to have an enhancement of helium and nitrogen at their surface (Schonberner et al. 1988, Gies & Lambert 1992). However, a direct link between rotation rate and surface abundance has yet to be found for several reasons. There is a lack of surface abundance determinations for anything other than slow rotators and the effects of binary evolution (see Section 1.1.2 for an overview of the major evolutionary channels in massive binary stars), magnetic fields, and mass loss via winds need to be subtracted from observations. Many of these processes dominate in massive stars; as previously stated, most massive stars are members of binaries systems and have strong stellar winds (Section 1.5).

Mass loss from massive stars is also known to be an important processes that can heavily affect their evolution. In fact, it has been shown that a substantial portion of a star's initial mass can be removed by their winds (De Loore et al. 1977). Therefore, it is important to have very accurate determinations of mass loss rates at every evolutionary stage in order to inform stellar evolutionary calculations. However, our understanding of mass loss is complicated by several factors. Hot star winds are not smooth; they are clumped (Hillier 1991, Moffat 2008, Owocki et al. 1987). Additionally, massive stars in binary systems can loose large amounts of material during phases of Roche-lobe overflow (Sections 1.1.2 and 1.4).

Regardless of these complicating factors, massive stars become several different types of supernovae through core collapse. Supernovae are classified by their spectral features. Type I supernovae show no hydrogen in their spectra while type II have hydrogen. Type II are further subclassed based on features in their light curves (IIP have a plateau and IIL have a linear decay after peak brightness) and their spectra (IIn have narrow emission lines). Type I supernovae are also subclassed based on the absence of silicon (Ib) and helium (Ic) in their spectra (a third sublcass of Type I supernovae are the Ia's which are thermonuclear in nature and not thought to form through massive star evolution and core collapse). Often core collapse supernovae exhibit features from more than one of these major classification schemes. For example Type IIb supernovae first appear to have hydrogen in their spectra and are therefore classified as a Type II. However, their spectra quickly evolve to resemble a Type Ib instead (SN 1993J for example; see Section 1.1.3). Additionally, it is often difficult to distiguish between Type Ib and Ic supernovae so they are usually lumped into one Type Ib/c category. While it remains unclear which massive stars become which type of supernovae, the progenitors for Type Ib/c supernovae

are generally thought to be Wolf-Rayet (WR) stars since they show a deficiency or absence of hydrogen in their spectra.

1.1.2 A Brief Overview of Evolution in Massive Binary Systems

Binary stars follow different evolutionary paths than single stars due to the effects of having a companion which can move material in and around the system (Iben 1991). In the case of close binary stars (see Figure 1.1), the more massive of the two stars will be the first to evolve off the main sequence. As the star expands through this evolutionary phase it can fill its Roche lobe, the region around each star that marked by the gravitational equipotential surface given by

$$\Phi = -G\left(\frac{M_1}{s_1} + \frac{M_2}{s_2}\right) - \frac{1}{2}\omega^2 r^2$$

where $s_1 = \sqrt{r_1^2 + r^2 + 2r_1 r\cos(\theta)}$ is the distance from star 1 to a point a distance r from the system's center of mass, $s_2 = \sqrt{r_2^2 + r^2 + 2r_2 r\cos(\theta)}$ is the distance from star 2 to a point a distance r from the system's center of mass, r_1 is the distance from the center of mass to star 1, r_2 is the distance from the center of mass to star 2, $\omega^2 = \frac{G(M_1+M_2)}{a^3}$, and $a = r_1 + r_2$ is the orbital separation of the system. This first Roche-lobe overflow occurs during one of three evolutionary phases: hydrogen core burning (case A mass transfer), after hydrogen core burning but before the ignition of helium core burning (case B), and during helium core burning (case C)(Kippenhahn & Weigert 1967, Lauterborn 1970). All of these cases cause a transfer of material via a mass stream to the secondary star to occur, creating an accretion disk around the secondary (Iben 1991). In fact, at least 70% of all massive stars are expected to undergo Roche-lobe overflow at some point in their lives (Sana et al.

2012) although the first overflow event (either Case A, B, or C) is responsible for removing most of the matter lost through this process. The secondary stars in these systems then accrete a significant amount of material from the primary stars (Iben 1991, Podsiadlowski et al. 1992, Sana et al. 2012).

Depending on its evolutionary status when the accretion starts, the secondary's future evolution can be affected because it is now more massive and luminous. When accretion occurs during the main sequence the secondary continues to evolve as if it started out with a larger initial mass (Hellings 1983). Additionally the gainer will acquire angular momentum from the mass transfer process, causing them to spin up to a rapidly rotating state (Packet 1981). At some point the mass gainer should reach critical rotation, when a star begins to lose mass due to its rapid rotation, and therefore no longer be able to accept more material. When this occurs and how much material has been efficiently transferred before accretion stops are important unanswered questions in binary star evolution (de Mink et al. 2007).

As a result of this mass transfer process, the originally more massive star (the primary) can be stripped of most of its envelope, resulting in a helium (He) or WR (nitrogen or carbon rich and shows no evidence of hydrogen) star (Sana et al. 2012). The primary star can retain a portion of its hydrogen envelope if both stars have similar initial masses. However, recent observations suggest equal mass systems are a minority in binary evolution (Sana et al. 2012). Therefore, this process should almost always result in the formation of He and WR stars.

Helium and WR stars are expected to be the progenitors of Type Ib/c supernovae due to their lack of hydrogen (Gaskell et al. 1986, Nomoto et al. 1995, Podsiadlowski et al. 1992, Smith et al. 2011). The supernova explosion ultimately leaves the system with a compact remnant (a neutron star or black hole) and a secondary

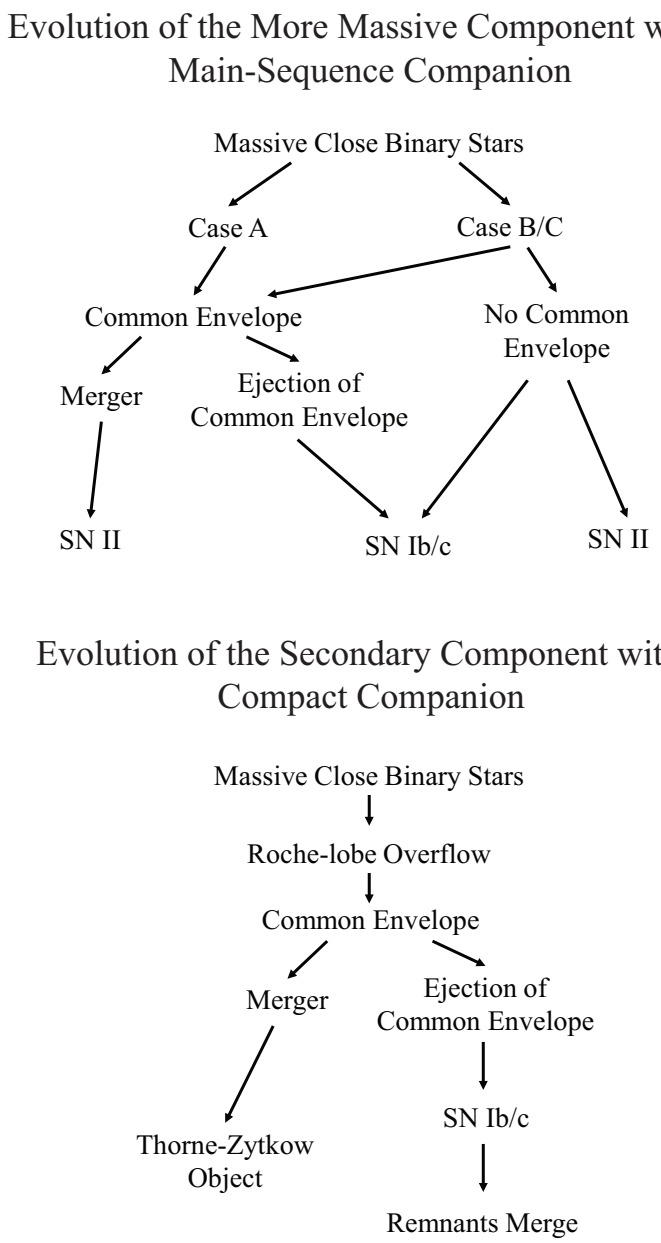

Figure 1.1 Simplified version of the evolutionary paths possible for the massive stars in close binaries. For a more complete set of evolutionary pathways, including those for wide binaries, see Podsiadlowski et al. (1992).

star which then evolves (if it survived the supernovae explosion of its companion), undergoing Roche lobe overflow similar to what the primary star did. This often results in the formation of a common envelope around the system when material is being accreted onto a compact companion (Paczynski 1976). In a wider binaries the common envelope will then be ejected and the system will then produce a second Type Ib/c via the now helium or WR secondary star. The remnants may then merge producing a gamma-ray burst (Izzard et al. 2004). In the case of a close binary, the compact object is expected to spiral in to the center of the secondary star during the common envelope phase. If the compact object is a neutron star, the system is theoretically expected to form a Thorne-Zytkow object, a red-supergiant with a neutron core, although these objects have not yet been observed (Thorne & Zytkow 1975).

1.1.3 Evidence for Binary Progenitors of Supernovae

Mass loss rates in single, massive star evolutionary models are known to be much too high compared to observations (Nieuwenhuijzen & de Jager 1990). In fact, when the clumping of winds in hot star systems is taken into account, mass loss rates may be reduced by up to a whole order of magnitude (Bouret et al. 2005, Fullerton et al. 2006, Puls et al. 2006). (Mass loss rates for O stars and WR stars are on the order of $10^{-7} - 10^{-5}$ $M_{\odot}$ yr $^{-1}$.) Using more appropriate mass loss rates in evolutionary models significantly changes their predictions. If adopted mass loss rates differ by as little as a factor of two the core collapse supernovae progenitor populations are significantly affected; differing mass loss rates for the same stars cause them to become different types of supernovae (Smartt 2009). This results in a disconnect between the number of He and WR stars thought to form through

single star evolution and the number of those stars actually observed. Additionally, the models are then no longer able to produce the observed proportion of Type Ib/c supernovae. Too few WR stars are produced to account for the number of observed Type Ib/c supernovae according to these models. Eruptive events may help alleviate this problem because it provides an additional way for stars to lose mass, but Roche-lobe overflow is thought to be the dominant channel, as opposed to single star evolution, for Type Ib/c supernovae because it removes the hydrogen rich envelope from the surface of the mass losing star (Smith & Owocki 2006, Smith et al. 2011). A large portion of Type Ib/c supernovae are expected to have progenitors whose initial mass is less than the theoretical lower limit to become a WR star (approximately 30 $M_{\odot}$); a problem that Roche lobe overflow also solves by allowing lower mass stars to be stripped of their envelopes (Smith et al. 2011).

Type IIb supernovae start out with hydrogen in their spectra, but rapidly evolve to a state that includes helium lines while the hydrogen lines weaken and disappear. Similar to the Type Ib/c supernovae, the lack of hydrogen in the Type IIb spectra suggests that they might be the result of stripped envelope binary evolution as well. In fact, SN 1993J was classified as a Type IIb and is one of a small number of core collapse supernovae that have been confirmed as coming from a binary system (see the paragraph below). Binary progenitors may also play a role in creating Type IIP supernovae. Observational evidence for a binary progenitor population is not clear, but theoretical work suggests that lower mass stars may evolve to a high enough mass through accretion to produce a Type IIP supernova (Smartt 2009).

Despite a theoretical understanding that at least a portion of Type Ib/c and IIb supernovae are formed through close binary star evolution, few detected SNe are thought to be from a star with a binary companion. SN 1993J (a Type IIb) is per-

haps the best example with convincing evidence for a binary progenitor (see Smartt 2009 for a comprehensive review of the system). Originally classified as a Type II supernova, SN 1993J's specturm evolved to a Type Ib within the first few weeks of detection. The evolution of the system's light curve, which could not be modeled with out including a companion, along with an astrometric argument for a companion star provides strong support for a progenitor within a binary system (Nomoto et al. 1993, Podsiadlowski et al. 1993, Woosley et al. 1994, Maund et al. 2004). Additionally, the spectral energy distribution of the system could only be fit with two component stars (Aldering et al. 1994).

Few other detected supernovae are thought to have arisen through massive binary star evolution. It has been suggested that SN 2001ig may have had a binary progenitor due to its similarity to SN 1993J and the detection of a point source at the supernova location approximately 1000 days post explosion (Ryder et al. 2006). An X-ray variable source near SN 2010O (Type Ib) suggests it may have been a black hole-nitrogen rich WR pair although the WN star was never detected (Nelemans et al. 2010). Finally, the supernova that caused Cassiopeia A was typed at a IIb from a light echo which has been suggested to be the result of a merger (Krause et al. 2008).

1.1.4 Scope of this Dissertation

As previously discussed binary evolution is important not only because of they make up a large portion of all massive stars, but also because mass loss through winds and Roche-lobe overflow strongly affects their future evolution. Therefore a complete understanding of these processes is imperative. For this dissertation I present the results of a study of asymmetries in circumstellar structures that form

from Roche-lobe overflow and strong stellar winds within binary systems. This will determine what happens to material lost from a star in a binary. Since the details of the structures of circumstellar material remain poorly understood, this will better inform models how matter moves in and around systems.

In particular, my work will help answer the following questions on binary star evolution: How does the orbital motion of stars affect the mass loss geometries? How do different mass transfer and mass loss rates affect the structures of material within binary systems and their evolution? How are structures within different systems related to each other? The answers to these questions will help constrain an area of stellar mass loss that is key to determining the evolutionary roll of binaries in massive stars and the formation of supernovae.

In this dissertation, I focus on two types of massive binary systems that current theory suggests will evolve into core-collapse supernovae: those undergoing Roche lobe overflow (see Section 1.4) and those with colliding stellar winds (see Section 1.5). Because these systems are undergoing heavy mass loss and transfer, it is important to understand their current state in order to better inform evolutionary theory and determine the binary progenitors of supernovae. In this dissertation, I combine X-ray spectroscopy and optical spectropolarimetry to study the mass and angular momentum loss from these types of systems in order to better understand the physics behind such processes. Correlating these two gives a detailed picture of the characteristics of the mass flows within and out of a system by creating a three dimensional view of the locations of the warm and hot gas in binaries. This provides powerful new information about the structure of winds, wind-wind interaction regions, and Roche lobe overflow geometries and what processes cause distortions or variability of those regions.

1.2 Tools: Spectropolarimetry

Spectropolarimetry is a technique used to distinguish between scattered and direct light within a spectrum. Light from a star becomes polarized when it interacts with gas and dust. Electron scattering is the dominant source of intrinsic polarization for the massive binary stars studied within this dissertation because they are hot systems: β Lyrae 13,300 K loser + 32,000 K gainer (Harmanec 2002); V444 Cyg 40,000 K O star + 35,000 K WN star (Underhill & Fahey 1987, Hamann & Schwarz 1992); WR 140 35,000 K O star + 70,000 WC star (Taranova & Shenavrin 2011). Electron scattering is known as a 'grey' process because it is not wavelength dependent. When light becomes polarized by electron scattering (sometimes also called Thompson scattering), the polarization pseudo-vectors (they operate just like regular vectors, but the angle of electric field is degenerate because 0° and 180° are the same) align themselves tangentially to the edge of the scattering region (Chandrasekhar 1960, Mihalas 1978). Therefore, a spherically symmetric scattering region will produce no net polarization due to cancellation effects (see Figure 1.2). However, if that symmetry is broken through clumping, in either density or abundances of the material, or a non-spherical scattering region, e.g. a disk, jet, or shock, the pseudo-vectors no longer cancel with each other and a non-zero polarization is measured. The position angle of the polarized light will be oriented 90° from the axis of elongation of the scattering region, giving implicit geometric information about the region without the need to resolve it. This makes spectropolarimetry a useful tool that reveals the locations and orientations of material within massive binary systems.

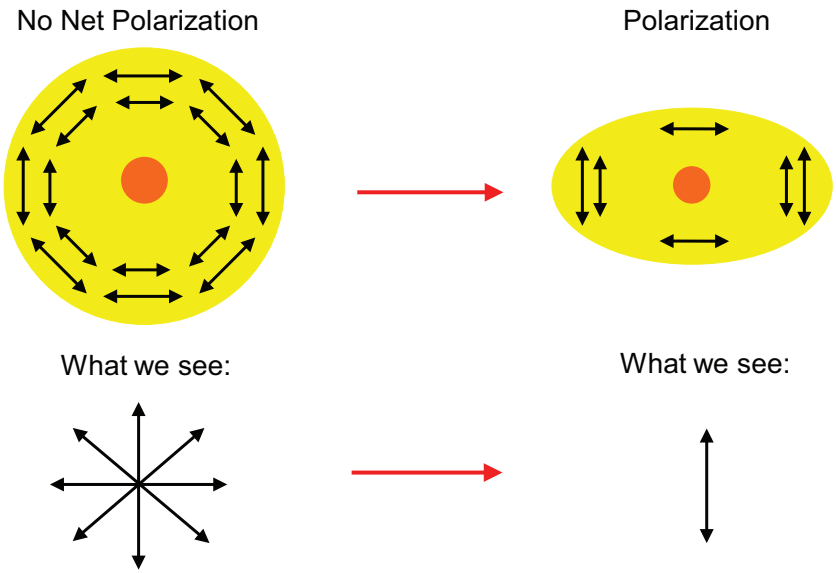

Figure 1.2 For electron scattering, no net polarization is measured from spherically symmetric scattering regions, but aspherical geometries cause the polarization pseudo-vectors to no longer cancel and a net polarization to be measured at a position angle oriented 90° from the direction of elongation of the scattering region. Therefore, the amount and position angle of the polarization allows us to determine geometric information about the scattering regions even if they are unresolved.

In practice, linear polarization is measured through the Stokes vectors which are calculated from the sums and differences of the intensity of light from a source at different angles, measured from north through east, on the sky. The total light, *I*, is just the sum of the intensity measured at 0° and 90° (Stokes 1852, Chandrasekhar 1960). A non-zero difference in these intensities indications the source has some polarization, but because polarization at 45° will produce no net difference the measurement is repeated for 45° and 135° angles on the sky (Stokes 1852, Chandrasekhar 1960). Specifically, the resulting Stokes parameters, *I*, *Q* and *U* are calculated through the following equations

$$I = I_0 + I_{90}$$

$$Q = I_0 - I_{90}$$

$$U = I_{45} - I_{135}$$

which are easily converted into percent polarization and position angle

$$p = \sqrt{q^2 + u^2}$$

$$\theta = \frac{1}{2} \tan^{-1} \frac{u}{q}$$

where $q = Q/I$ and $u = U/I$ (Stokes 1852, Chandrasekhar 1960).

Of course, electron scattering in the material within massive binary systems is not the only source of their observed polarization. Light interacts with the ISM via dust scattering as well, causing an additional wavelength dependent polarization. This must be taken into account if properties intrinsic to the source's scattering

region are the goal. In the optical regime the interstellar polarization (ISP) is described by the modified Serkowski law,

$$\frac{p}{p_{max}} = e^{-k \ln^2 \frac{\lambda_{max}}{\lambda}}$$

where p_{max} is the maximum polarization (in the optical wavelengths) measured at a wavelength of λ_{max}, k is a fitting parameter that controls the curvature of the function, and the position angle is a constant (Serkowski 1965, Wilking et al. 1982). Ultimately, the amount of ISP within an observation is dependent on the sight line and distance to the source. This is because different sight lines cover different amounts of ISM and in general light from a close source has less ISM to interact with than light from a more distance source.

Throughout this dissertation, I have subtracted the ISP from the presented spectropolarimetric observations where possible. However, in cases where no reliable ISP estimate exists variability in the measured polarization can be attributed to the massive binary system from which the light originated. This is because the ISP is not expected to be variable over the timescales that the spectropolarimetric observations contained within this dissertation were conducted.

1.3 Tools: X-rays

Velocity perturbations in the atmospheres and radiatively driven winds of massive stars are thought to give rise to temperatures of millions of degrees (Owocki et al. 1987, Owocki & Puls 1999). This allows for the thermal emission of X-rays. X-ray emission in binary systems can also arise from strong shocks formed by the

collision of the two stars' winds (in the case of colliding-wind binaries) or through accretion onto a compact companion. Thermal X-ray emission from the shock is often observed to be an order of magnitude greater in luminosity than the X-ray emission intrinsic to each star's wind (Pollock 1987). Non-thermal processes, such as inverse Compton scattering, where a low energy UV photon interacts and scatters with a highly energetic electron in such a way that allows it to gain energy and become an X-ray, can also be responsible for hard X-ray emission in colliding wind binaries (Leyder et al. 2010, Sugawara et al. 2011). In Roche lobe overflow systems X-rays may also be emitted from deceleration shocks where the mass stream impacts the disk edge.

X-ray observations must be conducted from a high altitude because Earth's atmosphere absorbs them. Therefore, X-ray instruments are placed aboard satellites and sounding rockets to place them in space, or aboard balloons in order to gain enough altitude for observations to be made. At X-ray energies individual photons are counted as events within detectors. In general when observing X-rays information such as the energy, the time of arrival, polarization, and position of the photon are recorded (or some subset of that information based on the detector's capabilities). How this information is recorded is dependent on the type of detector used by an X-ray telescope. The X-ray satellites used within this dissertation (*Rossi X-ray Timing Explorer*, also known as *RXTE*, and *XMM-Newton*) use two different types of detectors. *RXTE* makes use of an array of five proportional counters in its PCA instrument while *XMM-Newton* uses a CCD based system for its EPIC instrument.

A proportional counter is made up of a grounded chamber of gas that has a high voltage wire (anode) through the center. The chamber has a window which allows incident X-rays to enter while preventing the gas from escaping. An in-

coming X-ray photon interacts with the gas in the chamber via the photoelectric effect, ejecting an electron from the atom in which it is absorbed. If energetic enough, that electron then goes on to ionize other atoms in the gas. As these electrons gravitate toward the anode wire (due to the electric field set up within the gas chamber), they accelerate and use their resulting kinetic energy to ionize additional atoms causing an 'avalanche' of electrons. Since the voltage of the anode is finely tuned, the avalanche never saturates. This retains the proportionality between the energy of an incoming X-ray photon and the charge collected on the anode from the avalanche which allows proportional counters to be used as low resolution spectrometers. *RXTE*'s PCA instrument was designed for monitoring of X-ray sources on time scales as short as microseconds in the 2-60 keV energy range. Over the course of its 16 year lifetime (launched 30 December 1995, decommissioned 5 January 2012) two of its proportional counters within the PCA instrument suffered a loss of their propane layer which was used to prevent photons from outside of the operating energy range from being detected, causing their backgrounds to become unstable and less well understood.

CCDs work through a different mechanism. In this case, an incoming X-ray is photoelectrically absorbed within the semiconductor substrate on the CCD. The substrate has a constant probability of absorbing a photon per unit length such that higher energy photons tend to be absorbed at a greater depth than low energy photons. The photoelectric absorption creates electron-hole pairs in the substrate where the number of electrons is proportional to the energy of the incoming X-ray photon. The electrons are then allowed to drift to pixels by an applied electric field where they are stored before readout. By using CCDs and mirrors *XMM-Newton* (launched 10 December 1999) is able to spatially resolve X-ray sources signifi-

cantly better than *RXTE* was able to do. Additionally, it's large orbit, which takes it a third of the way to the moon, allows for long extended exposures of objects but also causes solar activity to often be detected within observations.

1.4 Roche-lobe Overflow and Beta Lyrae

As a star in a binary system expands through its normal evolution, it can fill a region around it called its Roche-lobe (region around a star in a binary system within which all material is gravitational bound to it, see Figure 1.3). Once this has happened, material pushed outside of the Roche-lobe is no longer gravitationally bound to the star, allowing it to move through the central Lagrange point to the secondary star in the system (Lubow & Shu 1975) and be lost through the L_3 Lagrange point (Sytov et al. 2007). The stream of material formed from the Roche-lobe overflow process causes an accretion disk to develop around the secondary star if the motion of the secondary star prevents the stream from striking its surface (Lubow & Shu 1975). Random motions of the gas within an an accretion disk, and the disk's interaction with magnetic fields cause gravitational energy to be converted into thermal energy, heating the disk material as it spirals toward the secondary star and slowing the gas's inspiral. Hot spots develop where the mass stream impacts the disk edge and are heated due to deceleration shocks formed by the interaction of the infalling material and outer regions of the disk. Jets, possibly similar to those seen in young stellar objects due to the accretion of material onto the star, can form and be a source of mass loss from the system.

One of the three systems I am studying within this dissertation is currently undergoing Roche-lobe overflow as evident by the shape of its light curve. Beta Lyrae

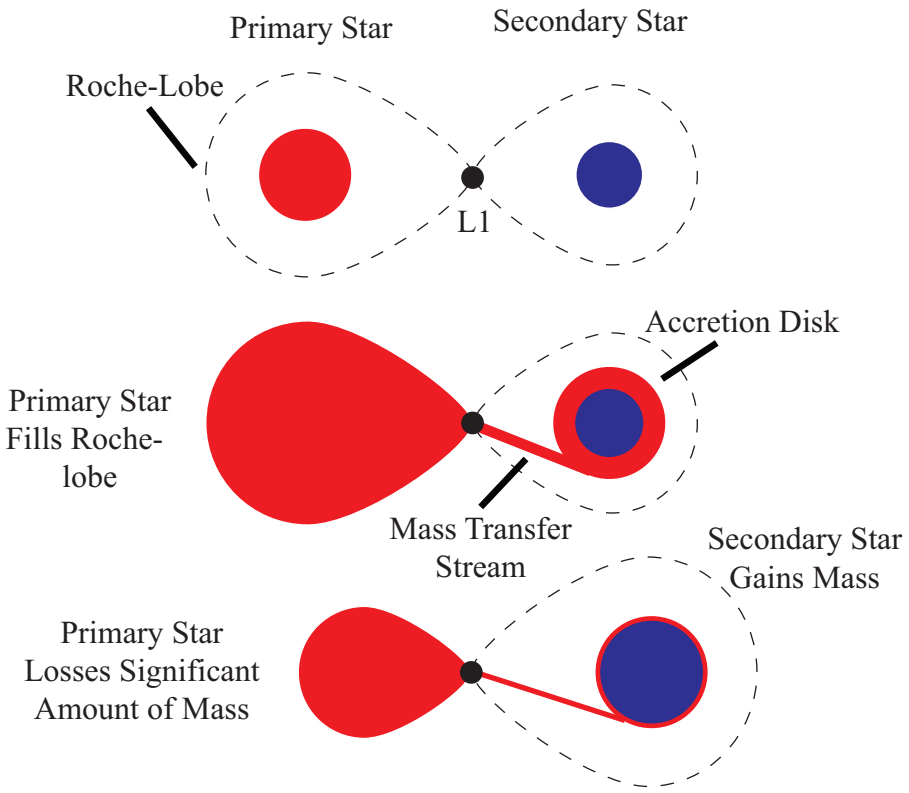

Figure 1.3 Schematic showing a Roche lobe overflow scenario. The dashed lines indicated unfilled Roche-lobes around both stars in a binary system. Once the more massive star has expanded and filled its Roche lobe material can be transfered on a gravitational equipotential surface to the secondary star through the first Lagrange point via the mass stream (Lubow & Shu 1975, Iben 1991).

(hereafter β Lyr) is a semi-detached binary system, with its primary star filling its Roche-lobe. Three-dimensional hydrodynamic modeling and the observed increase in orbital period (19 s yr^{-1}) imply it is actively transferring about 2×10^{-5} M$_\odot$ yr^{-1} from the primary star to the secondary and losing about 10^{-7} M$_\odot$ yr^{-1} from the system (Harmanec 2002, Nazarenko & Glazunova 2006). In fact, the mass transfer has caused a mass reversal to occur. The originally more massive star (approximately 9 M$_\odot$) is now only 3 M$_\odot$, while secondary star has gained enough mass to go from approximately 7 M$_\odot$ to 12.5 M$_\odot$ (De Greve & Linnell 1994). Additionally, the high rate of mass transfer has caused an optically thick accretion disk to form around the secondary main-sequence star (Huang 1963). Jets have also been detected in the system (Harmanec et al. 1996, Hoffman et al. 1998).

Despite its brightness (it is visible with the naked eye), and a long history of observational studies of the object (Goodricke & Englefield (1785) found β Lyrae to have a slightly less than 13 day periodic variability), many questions about mass transfer within the system remain. Many of the characteristics of the mass stream, and jets are still unknown. Specifically, the clumpiness of the material within these structures, the source and extent of the jets, the locations of mass loss within the system and the existence of a hot spot (see Chapter 2) are open areas of research. Addressing these issues is important to understanding the specifics of mass transfer and loss, circumstellar structures and their asymmetries, and the overall evolution of the system.

1.5 Colliding Wind Binaries, V444 Cyg, and WR 140

Colliding wind binaries are generally made up of two O stars, a WR and an O star, or two WR stars with strong winds that form a shock where they collide between the stars. The use of traditional observational diagnostic tools (e.g. radio fluxes, UV P Cygni profiles) to constrain mass loss in CWBs is challenging because the energetic nature of these systems leads to complicating phenomena such as non-spherical mass loss, non-thermal radio emission, and clumpy winds. However, the collision of the two stellar winds causes X-ray emission that outshines that of the winds of the individual stars. This X-ray emission carries information about the mass-loss characteristics of the system such as emission measure (or the amount of material responsible for the observed X-ray flux), density of the shocked gas, and density of the unshocked wind material due to X-ray absorption. However, current colliding wind models cannot reproduce the ranges of X-ray luminosities and temperatures observed from these systems. Models of short period colliding wind binaries often overestimate their X-ray luminosity. Results for the most massive systems are the closest to being consistent with observations (Russell et al. 2011, Parkin & Gosset 2011). Similarly, lower mass systems appear to be less well understood since their models do not reproduce observations and often overestimate X-ray flux as well (Nazé 2009, Pittard & Parkin 2010).

The effects of several processes that can skew the shape and location of the shock from expected values have been begun to be theoretically considered. Radiative inhibition or braking, where the acceleration of a wind is reduced by the radiation from a companion star may be of great importance in close, short-period binaries where the radiation fields from both stars in a system have the chance to

significantly interact with both winds (Stevens & Pollock 1994, Gayley et al. 1997). In fact, including these processes in models has been shown to lower the expected X-ray luminosities and temperatures to a value more consistent with observations for close binaries, and allow for a shock to form in model binaries in which one would otherwise not form due to the ram balance of the two winds (Stevens & Pollock 1994, Gayley et al. 1997). The idea of radiation from non-stellar parts of a binary system affecting the winds has also been considered. Parkin & Sim (2013) modeled the effects of X-ray emission from a shock and found that emission can also slow a wind down. This adds an additional layer of difficulty for modeling and determining when which effects are dominant in colliding wind binaries. Unfortunately, current observations have not been able to provide the same level of detail about colliding wind binaries as models. Stevens & Pollock (1994) noted that the current phase coverage for many close binaries is inadequate and more observations are needed to make reliable constraints on the types physical processes currently being considered in modeling efforts.

Orbital motion has been observed to affect the mass loss structure within several colliding wind binaries and can also play an important role in their shock structure. Both WR 98a and WR 104 have been observed to produce Archimedean spirals as part of their mass loss structures in the infrared (Monnier et al. 1999, Tuthill et al. 1999). While current observations have not detected distortions due to the Coriolis force in the wind-wind collision region, models have shown that the shape of the shock region is distorted into a spiral shape due to its effects (Lemaster et al. 2007, Russell et al. 2011).

Some colliding wind systems are thought to have evolved into the colliding wind state after a period of Roche-lobe overflow. In the case of V444 Cyg, evolutionary

models suggest that Roche lobe overflow left the system with a WN star and a more massive O-type main-sequence star (De Greve & Doom 1988). Initial masses of the stars were 24 and 16 $M_{\odot}$ but now the originally more massive component (WN star) is 12 $M_{\odot}$ and the companion (O star) is 28 $M_{\odot}$ (Hirv et al. 2006). It is thought that the system will eventually evolve into a high mass X-ray binary after the WN star evolves to a WC star (De Greve & Doom 1988). Currently, both components have strong winds which cause a shock to form. The wind-wind collision region is thought to be distorted by the Coriolis force due to its quick period (4.2 days) and circular orbit, and radiative braking and inhibition are thought to be important physical processes within the system (see Chapter 3) (Stevens & Pollock 1994, Gayley et al. 1997). However, none of these effects have been detected and their importance remains an open question.

By comparison, WR 140 is a long period (7.9 years) colliding wind binary whose high eccentricity (0.88) causes the orbital separation of the two stars to vary between 2 AU and 30 AU (Marchenko et al. 2003). This causes measurable changes in the wind collision region (see for example Dougherty et al. 2005) that can be used to determine how shocks are dependent on variations in local conditions (see Chapter 4). The existence of a hard X-ray component (due to inverse Compton scattering) is currently under debate.

1.6 Outline of Dissertation

In Chapter 2 I examine β Lyr's variable spectropolarimetric nature to determine specifics about the mass transfer and accretion structure within the system. I find evidence for the existence of a theoretical 'hot spot' on the disk edge and calculate

its size based on its polarimetric signature (Lomax et al. 2012). This work is already published.

In Chapter 3 I detail the results of my X-ray and spectropolarimetric investigation into the V444 Cyg system. I find that the orientation of wind-wind collision region is significantly affected by the Coriolis force. Evidence for the importance of radiative braking in the system is found through the location of the stagnation point inferred from hard X-ray light curves and the line polarization. This work is yet unpublished but I have received comments all collaborators and will submit the results for publication shortly.

In Chapter 4 I discuss the findings of an 11 year long X-ray study of the WR 140 system that provides key insights into the origin of the observed X-rays. Additionally, I analyze its long-term polarimetric behavior, which seems to be related to dust formation events. This work is currently in preparation for publication.

In Chapter 5 I propose future observations and modeling that will allow us to further understand these systems. In addition, I consider the results found in this dissertation in terms of a better overall understanding of mass loss and transfer in binary star systems.

Chapter 2

Geometrical Constraints on the Hot Spot in β Lyrae

Jamie R. Lomax, Jennifer L. Hoffman, Nicholas M. Elias II, Fabienne A. Bastien, and Bruce D. Holenstein 2012, The Astrophysical Journal, 750, 59

2.1 Abstract

We present results from six years of recalibrated and new spectropolarimetric data taken with the University of Wisconsin's Half-Wave Spectropolarimeter (HPOL) and six years of new data taken with the photoelastic modulating polarimeter (PEMP) at the Flower and Cook Observatory. Combining these data with polarimetric data from the literature allows us to characterize the intrinsic *BVRI* polarized light curves. A repeatable discrepancy of 0.245 days (approximately 6 hours) between the secondary minima in the total light curve and the polarization curve in

the *V* band, with similar behavior in the other bands, may represent the first direct evidence for an accretion hot spot on the disk edge.

2.2 Introduction

Beta Lyrae A (also known as HD 174638, HR 7106 and ADS 11745A; hereafter "β Lyr") is a bright, well-studied semi-detached eclipsing binary star system. The primary star is a B6-B8 II, giant star ("loser") with a mass of 3 $M_\odot$ that is transferring matter to its main-sequence B0.5 V, 12.5 $M_\odot$, companion ("gainer") at about 10^{-5} $M_\odot$ yr^{-1} via Roche lobe overflow (Hubeny & Plavec 1991, Harmanec & Scholz 1993). This process has created a thick accretion disk that obscures the gainer (Huang 1963, Wilson 1974, Hubeny & Plavec 1991, Skulskii 1992). A bipolar flow or jet has also been detected in the system through interferometric and spectropolarimetric methods (Harmanec et al. 1996, Hoffman et al. 1998; hereafter HNF). The system's mass ratio, q, has been placed between 4.2 and 6 with an inclination angle, *i*, of 85° (Wilson 1974). Other studies have suggested $i = 83°$ with $q = 5.6$ and $i = 80°$ with $q = 4.28$ (Hubeny & Plavec 1991, Skulskii 1992). More recent determinations of the orbital inclination place its value at $i = 86°$ (Linnell et al. 1998, Linnell 2000). These large mass ratios are evidence for mass reversal in the system's history. The disk's ability to obscure the gainer is due to the nearly edge-on inclination angle of the system.

The system has a well-established orbital period of 12.9 days that increases at a rate of 19 s yr^{-1} (Harmanec & Scholz 1993). Recent interferometric observations have produced the first images of the system, which show the loser and the disk as separate objects and confirm the orientation of the system axis, near $254°$, previ-

ously inferred from HNF's polarimetric analysis (Harmanec et al. 1996, Zhao et al. 2008, Schmitt et al. 2009). Understanding how mass moves between and around the stars and leaves the system is imperative to understanding the evolutionary future of β Lyr. However, interferometric techniques have yet to resolve the mass stream or bipolar outflows. We have used spectropolarimetry to study the system and begin to unlock the evolutionary clues contained within the circumstellar material.

Light scattering from electrons in the highly ionized circumstellar material in β Lyr produces a variable phase-dependent polarization. Since electron scattering preserves information about the orientation of the scattering region, analyzing polarimetric behavior as a function of wavelength allows us to determine from where in the system different spectral features have arisen. In this way, spectropolarimetric observations of β Lyr can be used to infer the geometrical properties of the scattering material in the system.

Optical polarimetry was used to study β Lyr as early as 1934, but it was not known until 1963 that the system exhibited variable polarization (Öhman 1934, Shakhovskoi 1963). Appenzeller and Hiltner (1967; hereafter AH) were the first to publish interstellar polarization (ISP) corrected broadband *UBV* polarization curves of β Lyr. More recently, HNF published ISP-corrected polarized light curves in the *V* band and Hα and He I $\lambda5876$ emission lines using a subset of the data we present here. HNF used the position angles of the polarized UV continuum and the hydrogen Balmer emission lines to confirm that a bipolar outflow exists in the β Lyr system after their discovery by Harmanec et al. (1996). HNF also interpreted the average position angle of the visible polarized light (164°) to be the physical axis of the binary system, an interpretation which was borne out by the interferometric images presented by Zhao et al (2008) and Schmitt et al. (2009).

In this paper we present new *BVRI* and He I λ5876 polarization curves and polarized light curves of β Lyr. The details of our spectropolarimetric observations and our interstellar polarization corrections are in Section 2.2. Section 2.3 presents and displays our observational results. We analyze our findings in Section 2.4 and summarize conclusions in Section 2.5.

2.3 Observations

This study compiles data from three distinct data sets. The first consists of 69 optical spectropolarimetric observations of β Lyr taken over 6 years with the University of Wisconsin's Half-Wave Spectropolarimeter (HPOL) at the 0.9 m telescope at Pine Bluff Observatory (PBO); the second data set comprises 6 years of broadband optical polarimetric data obtained at the Flower and Cook Observatory; and the third is 3 years of archived broadband optical polarimetric data from AH taken with the 24 inch rotatable telescope at the Yerkes Observatory. To calculate the phase for each observation, we used the ephemeris

$$T_{\rm pri} = \mathrm{HJD}\ 2,408,247.966 + 12.91378E + 3.87196 \times 10^{-6}E^2$$

where *E* is the total number of orbits since the primary eclipse that occurred at HJD 2,408,247.966 (Harmanec & Scholz 1993). This is the same ephemeris used by HNF; it does not significantly differ from the more recent ephemeris presented by Ak et al. (2007).

2.3.1 HPOL Data Set

The first 14 HPOL observations, obtained between 1992 September and 1994 November, used a dual Reticon array detector with a wavelength range of 3200-7600 Å and a resolution of 15 Å (see Wolff, Nordsieck, & Nook 1996 for further instrument information). The remaining 55 observations, taken between 1995 March and 1998 September, used a CCD-based system. This extended the wavelength range, 3200-10500 Å, and increased the resolution to 7.5 Å below 6000 Å and 10 Å above (Nordsieck & Harris 1996). The first 29 observations were previously published in HNF; they have undergone recalibration for use in this study.

Table 2.1 lists the orbital phases along with civil and heliocentric Julian dates for the midpoint of each HPOL observation. Each β Lyr observation covers the full spectral range, with the exception of the four nights indicated in Table 2.1. Two observations, 1995 May 27 and 1995 August 14, used only the red grating (6,000-10500 Å) of the CCD system while the other two, 1997 May 17 and 1997 May 26, used only the blue grating (3200-6000 Å). Each individual observation typically lasted between 45 minutes and an hour (approximately 0.03 to 0.04 days) when both gratings were used.

We used 11 HPOL observations of β Lyr B taken between 1995 May and 1999 November to obtain an ISP estimate. Beta Lyr B is a member of the same association as β Lyr A and is located 45" away (Abt et al. 1962). All of these observations were made using HPOL's CCD-based system. Table 2.1 also lists the civil and heliocentric Julian dates that correspond to the midpoints of each observation of β Lyr B and indicates which grating(s) were used during the observations. The first two observations, 1995 May 21 and 1996 July 3, were previously published in HNF and

have undergone recalibration for this study. We reduced all of the HPOL observations using the REDUCE software package (described by Wolff et al. 1996).

We estimated the ISP by fitting a modified Serkowski law curve to the error-weighted mean of the 11 observations of β Lyr B (Serkowski 1965, Wilking et al. 1982). The parameters for our ISP estimate are $P_{\max} = 0.422\% \pm 0.005\%$, $\lambda_{\max} = 4149$ Å ± 80 Å, $K = 0.699$ and $\mathrm{PA} = 151.16^\circ \pm 0.36^\circ$. We subtracted this ISP estimate from the HPOL β Lyr data. This new ISP correction has significantly improved uncertainties over previous estimates; it is consistent with the HNF estimate ($P_{\max} = 0.419\% \pm 0.013\%$, $\lambda_{\max} = 4605$ Å ± 260 Å, and $\mathrm{P.A.} = 151.0^\circ \pm 0.9^\circ$), which was determined using only the 1995 May 21 HPOL observation. AH found a similar estimate, $P_{max} = 0.42\% \pm 0.04\%$ and $PA = 153.2^\circ \pm 3^\circ$ by taking the weighted mean of the observed polarization of the associated stars β Lyr B, E, and F.

Table 2.1: Date and Phase Information for Midpoints of the HPOL β Lyrae and β Lyrae B Observations

Date	**HJD - 2,400,000**	**Phase[a]**
β Lyr Reticon (through HNF; recalibrated):		
1992 Sep 30	48895.71	0.661
1992 Oct 6	48901.67	0.121
1992 Oct 13	48908.60	0.657
1992 Oct 27	48922.58	0.737
1992 Dec 28	48984.52	0.525
1993 Jul 26	49194.60	0.762
1994 Jun 3	49506.78	0.890
1994 Jun 30	49533.59	0.962

Continued on Next Page...

Table 2.1 – Continued

Date	HJD - 2,400,000	Phase[a]
1994 Jul 22	49555.66	0.668
1994 Jul 29	49562.62	0.206
1994 Jul 31	49564.59	0.358
1994 Sep 8	49603.53	0.368
1994 Sep 20	49615.49	0.292
1994 Nov 7	49663.46	0.000
β Lyr CCD (through HNF, recalibrated):		
1995 Mar 14[b]	49790.89	0.848
1995 May 5	49842.82	0.862
1995 May 26	49863.82	0.485
1995 May 27[c]	49864.78	0.559
1995 May 30	49867.84	0.796
1995 Jun 4	49872.86	0.184
1995 Jul 3	49901.66	0.410
1995 Jul 10	49908.72	0.955
1995 Jul 12	49910.82	0.117
1995 Jul 18	49916.70	0.572
1995 Jul 24	49922.79	0.043
1995 Aug 6	49935.68	0.039
1995 Aug 14[c]	49943.63	0.653
1995 Aug 18	49947.72	0.969
1995 Sep 10	49970.74	0.749
β Lyr CCD (after HNF, final calibration):		
1996 Aug 21	50316.65	0.483
1997 May 17[d]	50585.78	0.283
1997 May 26[d]	50594.80	0.980
1997 Jul 5	50634.82	0.073
1997 Jul 7	50636.72	0.219
1997 Jul 7	50636.80	0.226
1997 Jul 10	50639.67	0.447
1997 Jul 10	50639.77	0.455
1997 Jul 10	50639.87	0.463
1997 Jul 11	50640.68	0.525
1997 Jul 11	50640.79	0.534
1997 Jul 15	50644.66	0.833

Continued on Next Page...

Table 2.1 – Continued

Date	HJD - 2,400,000	Phase[a]
1997 Jul 15	50644.77	0.842
1997 Jul 15	50644.86	0.848
1997 Jul 16	50645.68	0.912
1997 Jul 16	50645.78	0.920
1997 Jul 18	50647.71	0.069
1997 Aug 1	50661.64	0.145
1997 Aug 25	50685.64	0.000
1997 Aug 25	50685.74	0.008
1997 Aug 25	50685.83	0.015
1997 Aug 26	50686.66	0.079
1997 Aug 30	50690.62	0.385
1997 Sep 7	50698.63	0.004
1997 Sep 7	50698.71	0.010
1997 Sep 12	50703.77	0.401
1997 Sep 21	50712.64	0.087
1997 Sep 25	50716.73	0.403
1997 Oct 3	50724.60	0.011
1997 Oct 3	50724.70	0.019
1997 Oct 4	50725.57	0.086
1997 Oct 28	50749.54	0.939
1997 Nov 17	50769.56	0.486
1997 Dec 15	50797.50	0.645
1998 Apr 19	50922.86	0.333
1998 Apr 24	50927.90	0.723
1998 Jun 23	50987.82	0.354
1998 Jul 31	51025.78	0.287
1998 Aug 31	51056.62	0.671
1998 Sep 8	51064.76	0.300
β Lyr B CCD (through HNF, recalibrated):		
1995 May 21	49858.85	···
1996 Jul 3	50267.75	···
β Lyr B CCD (after HNF, final calibration):		
1998 Dec 8[c]	51155.54	···
1998 Dec 11[c]	51158.53	···
1998 Dec 12[d]	51159.52	···

Continued on Next Page...

Table 2.1 – Continued

Date	HJD - 2,400,000	Phase[a]
1999 Aug 30	51420.63	···
1999 Sep 13	51434.64	···
1999 Oct 3[d]	51454.59	···
1999 Nov 1[d]	51483.60	···
1999 Nov 2	51484.57	···
1999 Nov 15[d]	51497.55	···

[a] Phases were calculated using the ephemeris in Harmanec & Scholz (1993).

[b] Table 1 of HNF incorrectly lists this date as 1994 March 14.

[c] These observations used only the red grating; see Section 2.2.1.

[d] These observations used only the blue grating; see Section 2.2.1.

2.3.2 FCO Data Set

Our second data set is made up of 19 *B* band, 88 *V* band and 17 *R* band observations obtained at the Flower and Cook Observatory between 1987 and 1992 with the PEMP instrument (Holenstein 1991, Elias et al. 1996). The length of each observation was between 20 and 25 minutes (approximately 0.01 days). The phases along with the civil and heliocentric Julian dates for each observation are listed in Table 2.2. We have no observations of β Lyr B taken with the same instrument as this data set. Therefore, we used the Serkowski fit to the HPOL β Lyr B observations (see Section 2.2.1) to calculate the ISP contributions at the central wavelengths of

the *BVR* bands and subtracted these estimated values from the observations in this data set. We list these data and ISP subtracted data in Tables 2.3 through 2.5.

Table 2.2: Date and Phase Information for Midpoints of the FCO β Lyrae Observations

Date	**HJD - 2,400,000**	**Phase[a]**
B Band:		
1989 Apr 12	47628.88	0.753
1989 Apr 20	47636.85	0.352
1989 Apr 23	47639.85	0.583
1989 May 29	47675.80	0.366
1989 Jun 5	47682.78	0.907
1989 Jun 12	47689.80	0.448
1989 Jun 19	47696.78	0.989
1989 Jun 30	47707.76	0.840
1989 Jul 2	47709.79	0.994
1989 Jul 25	47732.74	0.772
1989 Jul 29	47736.79	0.081
1989 Aug 31	47769.68	0.632
1989 Sep 3	47772.58	0.844
1989 Sep 4	47773.57	0.922
1989 Sep 5	47774.57	0.999
1989 Sep 9	47778.57	0.308
1989 Oct 5	47804.45	0.318
1989 Oct 8	47807.60	0.550
1992 Jun 4	48777.76	0.543
V Band:		
1987 Aug 11	47018.61	0.563
1987 Aug 13	47020.57	0.718
1987 Aug 15	47022.59	0.872
1987 Aug 16	47023.58	0.949
1987 Aug 18	47025.54	0.104
1987 Aug 18	47025.56	0.104
1987 Aug 20	47027.59	0.259
1987 Aug 21	47028.58	0.336
1987 Aug 22	47029.56	0.413

Continued on Next Page...

Table 2.2 – Continued

Date	HJD - 2,400,000	Phase[a]
1987 Aug 24	47031.58	0.568
1987 Sep 15	47053.57	0.268
1987 Sep 26	47064.55	0.119
1987 Sep 27	47065.54	0.196
1987 Sep 28	47066.55	0.273
1987 Oct 5	47073.55	0.814
1987 Oct 6	47074.53	0.892
1988 Jun 13	47325.80	0.313
1988 Jun 24	47336.80	0.163
1988 Jun 28	47340.61	0.453
1988 Jul 1	47343.62	0.685
1988 Jul 16	47358.66	0.863
1988 Aug 19	47392.69	0.491
1988 Aug 22	47395.68	0.723
1988 Aug 23	47396.59	0.781
1988 Sep 1	47405.62	0.477
1988 Sep 2	47406.58	0.554
1988 Sep 3	47407.59	0.631
1988 Sep 7	47411.56	0.941
1988 Sep 8	47412.55	0.018
1988 Sep 11	47415.55	0.250
1988 Sep 15	47419.55	0.559
1988 Sep 16	47420.55	0.636
1988 Sep 27	47431.54	0.487
1988 Sep 28	47432.50	0.564
1988 Sep 29	47433.53	0.641
1988 Oct 1	47435.57	0.796
1988 Oct 2	47436.54	0.873
1988 Oct 6	47440.56	0.182
1988 Oct 10	47444.52	0.491
1988 Oct 14	47448.52	0.801
1988 Oct 15	47449.57	0.878
1988 Oct 26	47460.47	0.728
1988 Oct 27	47461.57	0.805
1988 Oct 28	47462.53	0.883
1988 Oct 30	47464.50	0.037
1988 Oct 31	47465.49	0.115

Continued on Next Page...

Table 2.2 – Continued

Date	HJD - 2,400,000	Phase[a]
1988 Nov 4	47469.50	0.424
1988 Nov 10	47475.53	0.888
1988 Nov 14	47479.50	0.197
1988 Nov 15	47480.47	0.274
1988 Nov 18	47483.49	0.506
1989 Apr 12	47628.85	0.733
1989 Apr 20	47636.83	0.352
1989 Apr 23	47639.83	0.583
1989 May 29	47675.78	0.366
1989 Jun 5	47682.80	0.907
1989 Jun 12	47689.82	0.448
1989 Jun 19	47696.80	0.989
1989 Jun 30	47707.78	0.840
1989 Jul 2	47709.81	0.994
1989 Jul 25	47732.76	0.772
1989 Jul 29	47736.82	0.081
1989 Aug 31	47769.70	0.632
1989 Sep 3	47772.60	0.844
1989 Sep 4	47773.61	0.922
1989 Sep 5	47774.60	0.999
1989 Sep 9	47778.60	0.308
1989 Oct 2	47801.68	0.105
1989 Oct 23	47822.59	0.709
1992 Jun 13	48786.72	0.239
1992 Jun 18	48791.65	0.625
1992 Jun 21	48794.62	0.838
1992 Jun 28	48801.73	0.398
1992 Jun 29	48802.67	0.476
1992 Jul 6	48809.68	0.017
1992 Jul 8	48811.59	0.152
1992 Jul 19	48822.60	0.002
1992 Jul 29	48832.57	0.775
1992 Jul 30	48833.58	0.852
1992 Aug 2	48836.61	0.084
1992 Aug 3	48837.60	0.161
1992 Aug 5	48839.60	0.316
1992 Aug 8	48842.56	0.548

Continued on Next Page...

Table 2.2 – Continued

Date	HJD - 2,400,000	Phase[a]
1992 Aug 11	48845.56	0.780
1992 Aug 19	48853.54	0.398
1992 Aug 30	48864.56	0.248
1992 Sep 1	48866.60	0.403
1992 Sep 13	48878.55	0.330
R Band:		
1989 Apr 12	47628.90	0.753
1989 Apr 20	47636.81	0.352
1989 Apr 23	47639.79	0.583
1989 May 29	47675.76	0.366
1989 Jun 5	47682.83	0.907
1989 Jun 12	47689.84	0.448
1989 Jun 19	47696.82	0.989
1989 Jun 30	47707.80	0.840
1989 Jul 2	47709.83	0.994
1989 Jul 25	47732.78	0.772
1989 Jul 29	47736.84	0.081
1989 Aug 31	47769.72	0.632
1989 Sep 3	47772.62	0.844
1989 Sep 5	47774.62	0.999
1989 Sep 9	47778.62	0.308
1989 Oct 2	47801.65	0.105
1989 Oct 10	47809.61	0.704

[a] Phases were calculated using the ephemeris in Harmanec & Scholz (1993).

Table 2.3: FCO *B* Filter Data

Phase	**HJD - 2,400,000**	**%*Q***	**%*U***	**ISP sub % *Q***	**ISP sub % *U***	$\sigma^{\mathbf{a}}_{\mathbf{i,Q}}$ **(%)**	$\sigma^{\mathbf{a}}_{\mathbf{i,U}}$ **(%)**
0.081	47736.79	0.395	-0.432	0.164	-0.067	0.007	0.007
0.308	47778.57	0.579	-0.493	0.348	-0.128	0.016	0.014
0.318	47804.45	0.617	-0.527	0.386	-0.162	0.010	0.008
0.352	47636.85	0.405	-0.438	0.174	-0.073	0.008	0.008
0.366	47675.80	0.549	-0.520	0.318	-0.155	0.009	0.008
0.448	47689.80	0.257	-0.261	0.026	0.104	0.007	0.007
0.543	48777.76	0.148	-0.350	-0.083	0.015	0.009	0.009
0.550	47807.60	0.460	-0.698	0.229	-0.333	0.016	0.023
0.583	47639.85	0.421	-0.527	0.190	-0.162	0.008	0.010
0.632	47769.68	0.497	-0.517	0.266	-0.152	0.010	0.010
0.753	47628.88	0.538	-0.479	0.307	-0.114	0.014	0.012
0.772	47732.74	0.486	-0.494	0.255	-0.129	0.011	0.011
0.840	47707.76	0.416	-0.469	0.185	-0.104	0.007	0.008
0.844	47772.58	0.406	-0.476	0.175	-0.111	0.009	0.011
0.907	47682.78	0.531	-0.488	0.300	-0.123	0.012	0.011
0.922	47773.57	0.470	-0.456	0.239	-0.091	0.010	0.010
0.989	47696.78	0.602	-0.566	0.371	-0.201	0.010	0.010
0.994	47709.79	0.635	-0.558	0.404	-0.193	0.018	0.016
0.999	47774.57	0.553	-0.645	0.322	-0.280	0.009	0.010

[a]The $\sigma_{i,Q}$ and $\sigma_{i,U}$ columns represent internal errors.

Table 2.4: FCO *V* Filter Data

Phase	**HJD - 2,400,000**	***%Q***	***%U***	**ISP sub *% Q***	**ISP sub *% U***	$\sigma^{a}_{i,Q}$ **(%)**	$\sigma^{a}_{i,U}$ **(%)**
0.002	48822.60	0.353	-0.393	0.134	-0.028	0.053	0.053
0.017	48809.68	0.405	-0.471	0.186	-0.106	0.013	0.013
0.018	47412.55	0.508	-0.433	0.289	-0.068	0.010	0.009
0.037	47464.50	0.687	-0.704	0.468	-0.339	0.097	0.099
0.081	47736.82	0.390	-0.422	0.171	-0.057	0.010	0.011
0.084	48836.61	0.390	-0.423	0.171	-0.058	0.010	0.010
0.104	47025.54	0.287	-0.412	0.068	-0.047	0.014	0.019
0.104	47025.56	0.292	-0.437	0.073	-0.072	0.008	0.012
0.105	47801.68	0.548	-0.458	0.329	-0.093	0.010	0.009
0.115	47465.49	0.310	-0.418	0.091	-0.053	0.006	0.008
0.119	47064.55	0.335	-0.454	0.116	-0.089	0.008	0.011
0.152	48811.59	0.440	-0.416	0.221	-0.051	0.012	0.012
0.161	48837.60	0.442	-0.438	0.223	-0.073	0.010	0.010
0.163	47336.80	0.370	-0.390	0.151	-0.025	0.092	0.096
0.182	47440.56	0.519	-0.431	0.300	-0.066	0.012	0.010
0.196	47065.54	0.397	-0.457	0.178	-0.092	0.009	0.010
0.197	47479.50	0.451	-0.474	0.232	-0.109	0.015	0.016
0.239	48786.72	0.322	-0.454	0.103	-0.089	0.015	0.015
0.248	48864.56	0.500	-0.510	0.281	-0.145	0.006	0.006

Continued on Next Page...

Table 2.4 – Continued

Phase	**HJD - 2,400,000**	$\%Q$	$\%U$	**ISP sub** $\%$ Q	**ISP sub** $\%$ U	$\sigma^{a}_{i,Q}$ (%)	$\sigma^{a}_{i,U}$ (%)
0.250	47415.55	0.492	-0.466	0.273	-0.101	0.014	0.013
0.259	47027.59	0.412	-0.441	0.193	-0.076	0.009	0.010
0.268	47053.57	0.420	-0.433	0.201	-0.068	0.007	0.007
0.273	47066.55	0.493	-0.448	0.274	-0.083	0.008	0.008
0.274	47480.47	0.549	-0.570	0.330	-0.205	0.011	0.011
0.308	47778.60	0.560	-0.461	0.341	-0.096	0.013	0.011
0.313	47325.80	0.408	-0.419	0.189	-0.054	0.009	0.009
0.316	48839.60	0.526	-0.492	0.307	-0.127	0.008	0.008
0.330	48878.55	0.580	-0.475	0.361	-0.110	0.012	0.012
0.336	47028.58	0.461	-0.423	0.242	-0.058	0.008	0.008
0.352	47636.83	0.391	-0.421	0.172	-0.056	0.008	0.009
0.366	47675.78	0.556	-0.495	0.337	-0.130	0.012	0.011
0.398	48801.73	0.455	-0.428	0.236	-0.063	0.021	0.021
0.398	48853.54	0.332	-0.397	0.113	-0.032	0.012	0.012
0.403	48866.60	0.492	-0.401	0.273	-0.036	0.009	0.009
0.413	47029.56	0.312	-0.268	0.093	0.097	0.044	0.039
0.424	47469.50	0.405	-0.414	0.186	-0.049	0.008	0.008
0.448	47689.82	0.269	-0.273	0.050	0.092	0.007	0.007
0.453	47340.61	0.318	-0.282	0.099	0.083	0.009	0.008
0.476	48802.67	0.233	-0.198	0.014	0.167	0.017	0.017
0.477	47405.62	0.328	-0.268	0.109	0.097	0.006	0.005

Continued on Next Page...

Table 2.4 – Continued

Phase	**HJD - 2,400,000**	$\%Q$	$\%U$	**ISP sub** $\%$ Q	**ISP sub** $\%$ U	$\sigma^{a}_{i,Q}$ (%)	$\sigma^{a}_{i,U}$ (%)
0.487	47431.54	0.430	-0.413	0.211	-0.048	0.008	0.007
0.491	47392.69	0.281	-0.349	0.062	0.016	0.009	0.011
0.491	47444.52	0.434	-0.432	0.215	-0.067	0.013	0.010
0.506	47483.49	0.501	-0.401	0.282	-0.036	0.011	0.009
0.548	48842.56	0.316	-0.455	0.097	-0.090	0.019	0.019
0.554	47406.58	0.354	-0.345	0.135	0.020	0.010	0.009
0.559	47419.55	0.341	-0.468	0.122	-0.103	0.007	0.009
0.563	47018.61	0.355	-0.389	0.136	-0.024	0.007	0.008
0.564	47432.50	0.372	-0.445	0.153	-0.080	0.013	0.016
0.568	47031.58	0.322	-0.402	0.103	-0.037	0.006	0.008
0.583	47639.83	0.421	-0.501	0.202	-0.136	0.013	0.015
0.625	48791.65	0.517	-0.523	0.298	-0.158	0.004	0.004
0.631	47407.59	0.514	-0.438	0.295	-0.073	0.011	0.009
0.632	47769.70	0.475	-0.469	0.256	-0.104	0.012	0.011
0.636	47420.55	0.328	-0.247	0.109	0.118	0.009	0.007
0.641	47433.53	0.575	-0.390	0.356	-0.025	0.013	0.010
0.685	47343.62	0.507	-0.438	0.288	-0.073	0.010	0.009
0.709	47822.59	0.508	-0.488	0.289	-0.123	0.009	0.008
0.718	47020.57	0.521	-0.398	0.302	-0.033	0.012	0.010
0.723	47395.68	0.558	-0.473	0.339	-0.108	0.011	0.009
0.728	47460.47	0.478	-0.470	0.259	-0.105	0.009	0.009

Continued on Next Page...

Table 2.4 – Continued

Phase	**HJD - 2,400,000**	***%Q***	***%U***	**ISP sub *% Q***	**ISP sub *% U***	$\sigma^{a}_{i,Q}$ **(%)**	$\sigma^{a}_{i,U}$ **(%)**
0.733	47628.85	0.518	-0.459	0.299	-0.094	0.009	0.008
0.772	47732.76	0.480	-0.449	0.261	-0.084	0.011	0.010
0.775	48832.57	0.508	-0.491	0.289	-0.126	0.011	0.011
0.780	48845.56	0.458	-0.477	0.239	-0.112	0.010	0.010
0.781	47396.59	0.483	-0.419	0.264	-0.054	0.010	0.009
0.796	47435.57	0.462	-0.417	0.243	-0.052	0.010	0.009
0.801	47448.52	0.422	-0.446	0.203	-0.081	0.007	0.007
0.805	47461.57	0.421	-0.424	0.202	-0.059	0.010	0.010
0.814	47073.55	0.435	-0.403	0.216	-0.038	0.009	0.008
0.838	48794.62	0.503	-0.456	0.284	-0.091	0.006	0.006
0.840	47707.78	0.411	-0.410	0.192	-0.045	0.007	0.007
0.844	47772.60	0.376	-0.425	0.157	-0.060	0.008	0.009
0.852	48833.58	0.391	-0.432	0.172	-0.067	0.011	0.011
0.863	47358.66	0.435	-0.357	0.216	0.008	0.009	0.008
0.872	47022.59	0.451	-0.640	0.232	-0.275	0.011	0.010
0.873	47436.54	0.467	-0.437	0.248	-0.072	0.012	0.011
0.878	47449.57	0.374	-0.388	0.155	-0.023	0.009	0.009
0.883	47462.53	0.389	-0.397	0.170	-0.032	0.007	0.008
0.888	47475.53	0.308	-0.376	0.089	-0.011	0.006	0.007
0.892	47074.53	0.376	-0.396	0.157	-0.031	0.010	0.011
0.907	47682.80	0.468	-0.442	0.249	-0.077	0.011	0.011

Continued on Next Page...

Table 2.4 – Continued

Phase	**HJD - 2,400,000**	***%Q***	***%U***	**ISP sub % *Q***	**ISP sub % *U***	$\sigma^{a}_{i,Q}$ **(%)**	$\sigma^{a}_{i,U}$ **(%)**
0.922	47773.61	0.451	-0.407	0.232	-0.042	0.008	0.008
0.941	47411.56	0.547	-0.396	0.328	-0.031	0.013	0.010
0.949	47023.58	0.540	-0.490	0.321	-0.125	0.010	0.009
0.989	47696.80	0.558	-0.509	0.339	-0.144	0.016	0.015
0.994	47709.81	0.623	-0.496	0.404	-0.131	0.016	0.013
0.999	47774.60	0.514	-0.603	0.295	-0.238	0.012	0.014

[a]The $\sigma_{i,Q}$ and $\sigma_{i,U}$ columns represent internal errors.

Table 2.5: FCO *R* Filter Data

Phase	**HJD - 2,400,000**	***%Q***	***%U***	**ISP sub *% Q***	**ISP sub *% U***	$\sigma^{a}_{i,Q}$ **(%)**	$\sigma^{a}_{i,U}$ **(%)**
0.081	47736.84	0.318	-0.373	0.131	-0.077	0.007	0.008
0.105	47801.65	0.454	-0.432	0.267	-0.136	0.011	0.011
0.308	47778.62	0.503	-0.431	0.316	-0.135	0.008	0.007
0.352	47636.81	0.376	-0.374	0.189	-0.078	0.012	0.012
0.366	47675.76	0.504	-0.489	0.317	-0.193	0.018	0.017
0.448	47689.84	0.261	-0.267	0.074	0.029	0.006	0.007
0.583	47639.79	0.377	-0.450	0.190	-0.154	0.009	0.011
0.632	47769.72	0.412	-0.443	0.225	-0.147	0.013	0.014
0.704	47809.61	0.830	-0.779	0.643	-0.483	0.017	0.016
0.753	47628.90	0.452	-0.417	0.265	-0.121	0.014	0.013
0.772	47732.78	0.398	-0.398	0.211	-0.102	0.009	0.009
0.840	47707.80	0.359	-0.373	0.172	-0.077	0.009	0.004
0.844	47772.62	0.330	-0.372	0.143	-0.076	0.007	0.007
0.907	47682.83	0.391	-0.443	0.204	-0.147	0.012	0.021
0.989	47696.82	0.449	-0.417	0.262	-0.121	0.011	0.010
0.994	47709.83	0.524	-0.438	0.337	-0.142	0.017	0.015
0.999	47774.62	0.463	-0.522	0.276	-0.226	0.013	0.014

[a]The $\sigma_{i,Q}$ and $\sigma_{i,U}$ columns represent internal errors.

2.3.3 AH Data Set

We also used archival *BV* polarization data taken between 1964 and 1966, originally published in AH. This data set consists of 37 *B* band and 127 *V* band observations, the details of which can be found in AH (and references therein). The DC two-channel polarimeter was rotated 30° between 12 separate 20 second exposures of β Lyr and the sky (Appenzeller 1965). Therefore, the total integration time for both β Lyr and the sky was 4 minutes (approximately 0.003 days). We converted these data from polarization magnitudes to percent polarization and converted their Julian dates to heliocentric Julian dates for use in this study. For consistency between the HPOL and AH data sets, we did not use AH's published ISP corrected data because it included two stars (β Lyr E and F) that are not included in the HPOL ISP estimate. Instead, we subtracted only the AH *BV* β Lyr B observations from their non-ISP corrected β Lyr data in each respective band.

2.4 Results

2.4.1 Broadband Polarimetry

To examine the behavior of the continuum polarization with orbital phase, we applied synthetic *BVRI* Johnson-Cousins band filters (described by Bessell 1990) to the ISP-corrected HPOL data. The filter routine produces broadband values and associated internal errors for each observation; however, we must still take into account systematic variations in the instrumental polarization between nights. Systematic errors for HPOL at PBO were evaluated by periodically analyzing observations of unpolarized standard stars. Tables 2.6 through 2.9 list broadband po-

larization values and internal errors determined by the filter routine along with the systematic errors. In the case of the Reticon data, the systematic errors are less well determined; based on our previous experience with these data, we have estimated the uncertainties in the Stokes parameters for the Reticon data to be 0.02% in all bands. Figures 2.1 through 2.4 display these data graphically, using the larger of the internal and systematic errors for each observation, along with the FCO and AH data.

The position angles for the *BVRI* bands remain relatively constant with orbital phase except near secondary eclipse, where the position angle values appear to rotate away from the mean value. The bottom panels in Figures 2.1 through 2.4 show this behavior in each band. In the standard picture of the system, the polarization is produced by scattering from the accretion disk edge; the average position angle at these wavelengths should therefore provide us with an estimate of the orientation of the axis of the disk and thus of the system as a whole. To calculate the average position angle in each band, we excluded the secondary eclipse points (between phases 0.425 and 0.575) because they do not follow the near-constant trend displayed at other phases and performed a linear, error-weighted, least-squares fit to the remaining data in *Q*-*U* space. We then used the slopes of the fitted lines to determine the position angles listed in Table 2.10. We also calculated a position angle for Balmer jump index (the vector difference between the polarization above and below the Balmer jump). As discussed in HNF, the broadband polarization in β Lyr undergoes a 90° position angle rotation across the Balmer Jump. Thus, this vector difference defines the system axis in *Q*-*U* space. Because the Balmer jump index is independent of the ISP, it provides us with an independent estimate of the orientation of the system axis.

We find the weighted mean position angle of the HPOL Reticon and CCD bands and the Balmer jump index to be $164.6° \pm 0.22°$. For each band, the CCD and Reticon position angles do not agree within uncertainties, with the Reticon data yielding larger position angles in all bands. This result is due to poor sampling in *Q*-*U* space; the Reticon data only consist of 14 data points in each band while there are 55 observations in the CCD *V* and *R* bands and 53 observations in the CCD *B* and *I* bands. This skews the linear fit since the full range of possible observable *Q*-*U* values is not well covered by the Reticon data. However, the larger systematic uncertainties we adopt for the Reticon data result in these points carrying a lower weight in the fit; thus, we are confident that our weighted mean is a fair representation of the true system axis. HNF found the mean *V* band position angle to be $163.8° \pm 0.15°$; while our estimate is not formally consistent with HNF's, it shows the broad band polarization behavior of the system is the same in all optical bands. Our polarization position angle implies a system position angle, defined by the position angle of the disk axis, of $253.8° \pm 0.15°$ on the sky. As expected for polarization by electron scattering, the position angle of the polarized light is perpendicular to the position angles describing the system orientation given by Zhao et al. (2008) and Schmitt et al. (2009). Zhao et al. (2008) estimated the position angle of the system's ascending node as $253.22° \pm 1.97°$ and $251.87° \pm 1.83°$ using two different image reconstruction techniques on their interferometric data and $254.39° \pm 0.83°$ using a model of the system, while Schmitt et al. (2009) estimate $249.0° \pm 4.0°$.

We rotated all of the HPOL, AH and FCO data to the average position angle of $164°$. This orients our data with respect to the intrinsic polarization axis of the system. After this rotation, $\%U$ averages to zero in each band and the polarization varies significantly only in the $\%Q$ direction. In the rest of this paper we present the

Table 2.6: HPOL Synthetic *B* Filter Data

Phase	**HJD - 2,400,000**	**%Q**	**%U**	**ISP sub % Q**	**ISP sub % U**	$\sigma_{\mathrm{i}}^{\mathrm{a}}$ (%)	$\sigma_{\mathrm{s}}^{\mathrm{a}}$ (%)
B Band Reticon:							
0.000	49663.46	0.4323	-0.6592	0.2020	-0.2953	0.0019	0.0200
0.121	48901.67	0.3905	-0.4928	0.1603	-0.1289	0.0030	0.0200
0.206	49562.62	0.4691	-0.4456	0.2388	-0.0816	0.0062	0.0200
0.292	49615.49	0.4248	-0.5536	0.1945	-0.1897	0.0015	0.0200
0.358	49564.59	0.4874	-0.4409	0.2572	-0.0770	0.0023	0.0200
0.368	49603.53	0.4823	-0.4503	0.2521	-0.0864	0.0016	0.0200
0.525	48984.52	0.2897	-0.4828	0.0594	-0.1188	0.0034	0.0200
0.657	48908.60	0.5574	-0.5334	0.3272	-0.1695	0.0030	0.0200
0.661	48895.71	0.5392	-0.5076	0.3090	-0.1436	0.0023	0.0200
0.668	49555.66	0.5611	-0.5302	0.3308	-0.1663	0.0015	0.0200
0.737	48922.58	0.4881	-0.5021	0.2578	-0.1382	0.0019	0.0200
0.762	49194.60	0.4841	-0.5642	0.2538	-0.2003	0.0011	0.0200
0.890	49506.78	0.4337	-0.4554	0.2027	-0.0953	0.0033	0.0200
0.962	49533.59	0.5317	-0.6448	0.3015	-0.2810	0.0019	0.0200
B Band CCD:							
0.000	50685.64	0.3794	-0.8971	0.1492	-0.5332	0.0044	0.0220
0.004	50698.63	0.5419	-0.4592	0.3117	-0.0953	0.0031	0.0220
0.008	50685.74	0.3222	-0.8462	0.0920	-0.4823	0.0046	0.0220

Continued on Next Page. . .

Table 2.6 – Continued

Phase	**HJD - 2,400,000**	***%Q***	***%U***	**ISP sub % *Q***	**ISP sub % *U***	$\sigma_{\mathrm{i}}^{\mathrm{a}}$ **(%)**	$\sigma_{\mathrm{s}}^{\mathrm{a}}$ **(%)**
0.010	50698.71	0.4679	-0.4787	0.2377	-0.1149	0.0063	0.0220
0.011	50724.60	0.4846	-0.5516	0.2544	-0.1877	0.0035	0.0220
0.015	50685.83	0.2608	-0.8606	0.0326	-0.4982	0.0082	0.0220
0.019	50724.70	0.3952	-0.5281	0.1650	-0.1643	0.0053	0.0220
0.039	49935.68	0.3981	-0.6422	0.1679	-0.2783	0.0030	0.0100
0.043	49922.79	0.6360	-0.5666	0.4058	-0.2028	0.0034	0.0100
0.069	50647.71	0.4896	-0.5155	0.2594	-0.1516	0.0036	0.0140
0.073	50634.82	0.3301	-0.3861	0.0999	-0.0223	0.0024	0.0140
0.079	50686.66	0.3372	-0.5482	0.1070	-0.1843	0.0029	0.0220
0.086	50725.57	0.2982	-0.3927	0.0680	-0.0289	0.0033	0.0220
0.087	50712.64	0.3415	-0.5013	0.1113	-0.1374	0.0029	0.0220
0.117	49910.82	0.3875	-0.4219	0.1573	-0.0581	0.0023	0.0100
0.145	50661.64	0.3608	-0.4670	0.1307	-0.1030	0.0027	0.0140
0.184	49872.86	0.2940	-0.4482	0.0638	-0.0844	0.0027	0.0100
0.219	50636.72	0.4525	-0.5404	0.2223	-0.1765	0.0028	0.0140
0.226	50636.80	0.4000	-0.5080	0.1698	-0.1442	0.0024	0.0140
0.283	50585.78	0.4840	-0.6685	0.2538	-0.3047	0.0018	0.0140
0.287	51025.78	0.3671	-0.5343	0.1368	-0.1704	0.0028	0.0150
0.300	51064.76	0.3961	-0.6073	0.1659	-0.2435	0.0054	0.0150
0.333	50922.86	0.5179	-0.5637	0.2877	-0.1998	0.0025	0.0080
0.354	50987.82	0.4517	-0.5322	0.2215	-0.1683	0.0025	0.0150

Continued on Next Page. . .

Table 2.6 – Continued

Phase	**HJD - 2,400,000**	***%Q***	***%U***	**ISP sub % *Q***	**ISP sub % *U***	$\sigma_{\mathrm{i}}^{\mathrm{a}}$ (%)	$\sigma_{\mathrm{s}}^{\mathrm{a}}$ (%)
0.385	50690.62	0.4775	-0.5832	0.2473	-0.2193	0.0031	0.0220
0.401	50703.77	0.3079	-0.4730	0.0777	-0.1091	0.0029	0.0220
0.403	50716.73	0.3754	-0.4673	0.1453	-0.1027	0.0057	0.0220
0.410	49901.66	0.3475	-0.3311	0.1174	0.0327	0.0024	0.0100
0.447	50639.67	0.2957	-0.3379	0.0655	0.0261	0.0025	0.0140
0.455	50639.77	0.3165	-0.3542	0.0863	0.0097	0.0028	0.0140
0.463	50639.87	0.3221	-0.4072	0.0920	-0.0433	0.0047	0.0140
0.483	50316.65	0.4778	-0.4378	0.2475	-0.0739	0.0020	0.0300
0.485	49863.82	0.3250	-0.3518	0.0948	0.0121	0.0022	0.0100
0.486	50769.56	0.3433	-0.4030	0.1131	-0.0391	0.0041	0.0220
0.525	50640.68	0.3457	-0.5121	0.1155	-0.1482	0.0029	0.0140
0.534	50640.79	0.3062	-0.5369	0.0760	-0.1730	0.0099	0.0140
0.572	49916.70	0.4309	-0.4738	0.2006	-0.1099	0.0020	0.0100
0.645	50797.50	0.4821	-0.5407	0.2519	-0.1769	0.0050	0.0220
0.671	51056.62	0.5691	-0.5555	0.3388	-0.1916	0.0024	0.0150
0.723	50927.90	0.5293	-0.6009	0.2990	-0.2369	0.0051	0.0080
0.749	49970.74	0.5268	-0.4740	0.2965	-0.1101	0.0020	0.0100
0.796	49867.84	0.4758	-0.5419	0.2455	-0.1780	0.0017	0.0100
0.833	50644.66	0.3884	-0.5293	0.1581	-0.1654	0.0024	0.0140
0.842	50644.77	0.3740	-0.5620	0.1438	-0.1981	0.0026	0.0140
0.848	49790.89	0.4561	-0.5198	0.2259	-0.1559	0.0033	0.0100

Continued on Next Page. . .

Table 2.6 – Continued

Phase	**HJD - 2,400,000**	***%Q***	***%U***	**ISP sub % *Q***	**ISP sub % *U***	$\sigma_{\mathrm{i}}^{\mathrm{a}}$ **(%)**	$\sigma_{\mathrm{s}}^{\mathrm{a}}$ **(%)**
0.848	50644.86	0.3216	-0.5164	0.0914	-0.1526	0.0025	0.0140
0.862	49842.82	0.4337	-0.4914	0.2035	-0.1276	0.0023	0.0100
0.912	50645.68	0.3993	-0.4460	0.1691	-0.0821	0.0024	0.0140
0.920	50645.78	0.4319	-0.4887	0.2017	-0.1249	0.0041	0.0140
0.939	50749.54	0.5136	-0.7251	0.2834	-0.3612	0.0035	0.0220
0.955	49908.72	0.7422	-0.5796	0.5120	-0.2158	0.0051	0.0100
0.969	49947.72	0.6624	-0.5345	0.4322	-0.1707	0.0041	0.0100
0.980	50594.80	0.4666	-0.7196	0.2365	-0.3557	0.0082	0.0140

[a]The σ_i and σ_s columns represent internal and systematic errors respectively.

Table 2.7: HPOL Synthetic *V* Filter Data

Phase	**HJD - 2,400,000**	**%*Q***	**%*U***	**ISP sub % *Q***	**ISP sub % *U***	σ_i^a (%)	σ_s^a (%)
V Band Reticon:							
0.000	49663.46	0.4485	-0.6204	0.2292	-0.2737	0.0021	0.0200
0.121	48901.67	0.3620	-0.4839	0.1427	-0.1373	0.0025	0.0200
0.206	49562.62	0.4578	-0.3863	0.2386	-0.0398	0.0056	0.0200
0.292	49615.49	0.4058	-0.5298	0.1865	-0.1830	0.0018	0.0200
0.358	49564.59	0.4499	-0.4464	0.2306	-0.0998	0.0024	0.0200
0.368	49603.53	0.4474	-0.4376	0.2280	-0.0909	0.0020	0.0200
0.525	48984.52	0.2534	-0.4453	0.0339	-0.0985	0.0026	0.0200
0.657	48908.60	0.5430	-0.4910	0.3236	-0.1444	0.0032	0.0200
0.661	48895.71	0.4934	-0.4758	0.2741	-0.1291	0.0021	0.0200
0.668	49555.66	0.5306	-0.4902	0.3113	-0.1435	0.0017	0.0200
0.737	48922.58	0.4451	-0.4905	0.2258	-0.1438	0.0018	0.0200
0.762	49194.60	0.4531	-0.5427	0.2337	-0.1960	0.0013	0.0200
0.890	49506.78	0.3825	-0.4272	0.1590	-0.0808	0.0053	0.0200
0.962	49533.59	0.5339	-0.6376	0.3147	-0.2910	0.0023	0.0200
V Band CCD:							
0.000	50685.64	0.3923	-0.7974	0.1732	-0.4508	0.0029	0.0100
0.004	50698.63	0.5482	-0.4414	0.3288	-0.0948	0.0020	0.0100
0.008	50685.74	0.3562	-0.7982	0.1370	-0.4516	0.0030	0.0100

Continued on Next Page. . .

Table 2.7 – Continued

Phase	**HJD - 2,400,000**	$\%Q$	$\%U$	**ISP sub % Q**	**ISP sub % U**	$\sigma_{\rm i}^{\rm a}$ (%)	$\sigma_{\rm s}^{\rm a}$ (%)
0.010	50698.71	0.5082	-0.4602	0.2892	-0.1139	0.0037	0.0100
0.011	50724.60	0.5266	-0.5742	0.3075	-0.2280	0.0022	0.0100
0.015	50685.83	0.3205	-0.8314	0.1022	-0.4861	0.0044	0.0100
0.019	50724.70	0.4657	-0.5516	0.2464	-0.2053	0.0029	0.0100
0.039	49935.68	0.4228	-0.6091	0.2038	-0.2631	0.0021	0.0050
0.043	49922.79	0.6145	-0.5334	0.3948	-0.1860	0.0024	0.0050
0.069	50647.71	0.4805	-0.5109	0.2612	-0.1644	0.0024	0.0070
0.073	50634.82	0.3706	-0.3841	0.1516	-0.0382	0.0016	0.0070
0.079	50686.66	0.3369	-0.5427	0.1179	-0.1966	0.0018	0.0100
0.086	50725.57	0.3240	-0.4117	0.1047	-0.0652	0.0021	0.0100
0.087	50712.64	0.3497	-0.4760	0.1304	-0.1295	0.0018	0.0100
0.117	49910.82	0.3706	-0.3946	0.1517	-0.0479	0.0015	0.0050
0.145	50661.64	0.3556	-0.4517	0.1361	-0.1047	0.0019	0.0070
0.184	49872.86	0.3099	-0.4214	0.0903	-0.0756	0.0017	0.0050
0.219	50636.72	0.4250	-0.5151	0.2058	-0.1685	0.0019	0.0070
0.226	50636.80	0.3969	-0.5070	0.1777	-0.1604	0.0016	0.0070
0.283	50585.78	0.4976	-0.6274	0.2777	-0.2799	0.0012	0.0070
0.287	51025.78	0.3863	-0.5250	0.1671	-0.1785	0.0017	0.0100
0.300	51064.76	0.3968	-0.5232	0.1779	-0.1771	0.0030	0.0100
0.333	50922.86	0.5109	-0.5433	0.2916	-0.1967	0.0016	0.0050
0.354	50987.82	0.4459	-0.4969	0.2268	-0.1506	0.0016	0.0100

Continued on Next Page. . .

Table 2.7 – Continued

Phase	**HJD - 2,400,000**	$\%Q$	$\%U$	**ISP sub % Q**	**ISP sub % U**	$\sigma_{\rm i}^{\rm a}$ (%)	$\sigma_{\rm s}^{\rm a}$ (%)
0.385	50690.62	0.4809	-0.5536	0.2617	-0.2070	0.0019	0.0100
0.401	50703.77	0.3649	-0.4747	0.1452	-0.1273	0.0019	0.0100
0.403	50716.73	0.3778	-0.4680	0.1584	-0.1217	0.0032	0.0100
0.410	49901.66	0.3568	-0.3198	0.1376	0.0266	0.0018	0.0050
0.447	50639.67	0.3001	-0.3333	0.0811	0.0132	0.0017	0.0070
0.455	50639.77	0.3256	-0.3258	0.1063	0.0209	0.0018	0.0070
0.463	50639.87	0.3353	-0.3521	0.1161	-0.0056	0.0031	0.0070
0.483	50316.65	0.4529	-0.4384	0.2338	-0.0928	0.0014	0.0200
0.485	49863.82	0.3189	-0.3351	0.1000	0.0106	0.0015	0.0050
0.486	50769.56	0.3571	-0.4099	0.1378	-0.0634	0.0025	0.0100
0.525	50640.68	0.3109	-0.5088	0.0915	-0.1620	0.0019	0.0070
0.534	50640.79	0.2687	-0.5048	0.0508	-0.1606	0.0059	0.0070
0.559	49864.78	0.5740	-0.4877	0.3675	-0.1488	0.0045	0.0050
0.572	49916.70	0.4404	-0.4434	0.2215	-0.0974	0.0014	0.0050
0.645	50797.50	0.4919	-0.5245	0.2736	-0.1783	0.0027	0.0100
0.653	49943.63	0.6036	-0.4925	0.3022	-0.1452	0.0022	0.0050
0.671	51056.62	0.5323	-0.5334	0.3130	-0.1869	0.0015	0.0100
0.723	50927.90	0.4912	-0.5611	0.2714	-0.2138	0.0034	0.0050
0.749	49970.74	0.5054	-0.4378	0.2861	-0.0908	0.0013	0.0050
0.796	49867.84	0.4662	-0.5150	0.2471	-0.1688	0.0012	0.0050
0.833	50644.66	0.3579	-0.5014	0.1386	-0.1549	0.0017	0.0070

Continued on Next Page. . .

Table 2.7 – Continued

Phase	**HJD - 2,400,000**	***%Q***	***%U***	**ISP sub % *Q***	**ISP sub % *U***	$\sigma_{\mathrm{i}}^{\mathrm{a}}$ **(%)**	$\sigma_{\mathrm{s}}^{\mathrm{a}}$ **(%)**
0.842	50644.77	0.3457	-0.5039	0.1264	-0.1573	0.0018	0.0070
0.848	49790.89	0.4292	-0.4756	0.2104	-0.1292	0.0020	0.0050
0.848	50644.86	0.3131	-0.4951	0.0939	-0.1483	0.0016	0.0070
0.862	49842.82	0.4222	-0.4591	0.2037	-0.1134	0.0015	0.0050
0.912	50645.68	0.3943	-0.4385	0.1748	-0.0918	0.0016	0.0070
0.920	50645.78	0.3880	-0.4313	0.1690	-0.0849	0.0025	0.0070
0.939	50749.54	0.4909	-0.6709	0.2715	-0.3242	0.0022	0.0100
0.955	49908.72	0.6986	-0.5220	0.4790	-0.1747	0.0035	0.0050
0.969	49947.72	0.6168	-0.4929	0.3989	-0.1476	0.0028	0.0050
0.980	50594.80	0.4644	-0.5950	0.2447	-0.2476	0.0053	0.0070

[a]The σ_i and σ_s columns represent internal and systematic errors respectively.

Table 2.8: HPOL Synthetic *R* Filter Data

Phase	**HJD - 2,400,000**	**%*Q***	**%*U***	**ISP sub % *Q***	**ISP sub % *U***	$\sigma_{\mathrm{i}}^{\mathrm{a}}$ (%)	$\sigma_{\mathrm{s}}^{\mathrm{a}}$ (%)
R Band Reticon:							
0.000	49663.46	0.4242	-0.5664	0.2205	-0.2422	0.0027	0.0200
0.121	48901.67	0.3360	-0.4694	0.1341	-0.1494	0.0038	0.0200
0.206	49562.62	0.3777	-0.3521	0.1861	-0.0332	0.0067	0.0200
0.292	49615.49	0.3735	-0.4713	0.1709	-0.1498	0.0025	0.0200
0.358	49564.59	0.3955	-0.4077	0.1947	-0.0863	0.0032	0.0200
0.368	49603.53	0.3917	-0.4168	0.1852	-0.0923	0.0027	0.0200
0.525	48984.52	0.2297	-0.4119	0.0295	-0.0905	0.0032	0.0200
0.657	48908.60	0.4936	-0.4751	0.2912	-0.1619	0.0045	0.0200
0.661	48895.71	0.4402	-0.4586	0.2373	-0.1349	0.0033	0.0200
0.668	49555.66	0.4711	-0.4491	0.2711	-0.1300	0.0022	0.0200
0.737	48922.58	0.3817	-0.4389	0.1567	-0.1187	0.0042	0.0200
0.762	49194.60	0.4064	-0.4960	0.2035	-0.1761	0.0018	0.0200
0.890	49506.78	0.2308	-0.5012	0.0096	-0.1950	0.0098	0.0200
0.962	49533.59	0.4678	-0.5736	0.2714	-0.2479	0.0035	0.0200
R Band CCD:							
0.000	50685.64	0.4015	-0.6876	0.1993	-0.3676	0.0020	0.0080
0.004	50698.63	0.5123	-0.4037	0.3090	-0.0828	0.0014	0.0080
0.008	50685.74	0.3668	-0.7072	0.1640	-0.3878	0.0019	0.0080

Continued on Next Page. . .

Table 2.8 – Continued

Phase	**HJD - 2,400,000**	***%Q***	***%U***	**ISP sub % *Q***	**ISP sub % *U***	$\sigma_{\mathrm{i}}^{\mathrm{a}}$ **(%)**	$\sigma_{\mathrm{s}}^{\mathrm{a}}$ **(%)**
0.010	50698.71	0.4717	-0.3918	0.2708	-0.0742	0.0019	0.0080
0.011	50724.60	0.5048	-0.5398	0.3034	-0.2217	0.0014	0.0080
0.015	50685.83	0.3437	-0.7394	0.1418	-0.4221	0.0036	0.0080
0.019	50724.70	0.4562	-0.5390	0.2541	-0.2205	0.0017	0.0080
0.039	49935.68	0.4169	-0.5498	0.2151	-0.2291	0.0014	0.0040
0.043	49922.79	0.5921	-0.5174	0.3832	-0.1864	0.0025	0.0040
0.069	50647.71	0.4405	-0.4660	0.2384	-0.1469	0.0015	0.0070
0.073	50634.82	0.3695	-0.3606	0.1678	-0.0419	0.0010	0.0070
0.079	50686.66	0.3101	-0.5081	0.1085	-0.1898	0.0011	0.0080
0.086	50725.57	0.3175	-0.4057	0.1147	-0.0859	0.0013	0.0080
0.087	50712.64	0.3317	-0.4421	0.1289	-0.1217	0.0012	0.0080
0.117	49910.82	0.3510	-0.3731	0.1492	-0.0526	0.0010	0.0040
0.145	50661.64	0.3317	-0.4227	0.1267	-0.0989	0.0015	0.0070
0.184	49872.86	0.2922	-0.3812	0.0882	-0.0616	0.0011	0.0040
0.219	50636.72	0.3710	-0.4600	0.1691	-0.1402	0.0012	0.0070
0.226	50636.80	0.3663	-0.4598	0.1638	-0.1391	0.0011	0.0070
0.283	50585.78	0.4810	-0.5997	0.2692	-0.2653	0.0015	0.0070
0.287	51025.78	0.3534	-0.4673	0.1512	-0.1477	0.0011	0.0140
0.300	51064.76	0.3697	-0.4742	0.1683	-0.1560	0.0018	0.0140
0.333	50922.86	0.4735	-0.4876	0.2710	-0.1675	0.0010	0.0080
0.354	50987.82	0.4001	-0.4492	0.1984	-0.1304	0.0010	0.0140

Continued on Next Page. . .

Table 2.8 – Continued

Phase	**HJD - 2,400,000**	$\%Q$	$\%U$	**ISP sub % Q**	**ISP sub % U**	$\sigma_{\rm i}^{\rm a}$ (%)	$\sigma_{\rm s}^{\rm a}$ (%)
0.385	50690.62	0.4323	-0.4968	0.2300	-0.1768	0.0012	0.0080
0.401	50703.77	0.3302	-0.4507	0.1257	-0.1271	0.0015	0.0080
0.403	50716.73	0.3535	-0.4378	0.1509	-0.1187	0.0020	0.0080
0.410	49901.66	0.3238	-0.2942	0.1197	0.0269	0.0012	0.0040
0.447	50639.67	0.2888	-0.3107	0.0874	0.0085	0.0011	0.0070
0.455	50639.77	0.3009	-0.3000	0.0987	0.0201	0.0011	0.0070
0.463	50639.87	0.3125	-0.3099	0.1106	0.0090	0.0017	0.0070
0.483	50316.65	0.4170	-0.3947	0.2131	-0.0749	0.0009	0.0200
0.485	49863.82	0.2997	-0.2970	0.0976	0.0219	0.0010	0.0040
0.486	50769.56	0.3217	-0.3832	0.1196	-0.0638	0.0014	0.0080
0.525	50640.68	0.3155	-0.4577	0.1120	-0.1365	0.0014	0.0070
0.534	50640.79	0.2685	-0.4502	0.0701	-0.1377	0.0016	0.0070
0.559	49864.78	0.5560	-0.4658	0.3583	-0.1510	0.0022	0.0040
0.572	49916.70	0.4179	-0.3970	0.2160	-0.0770	0.0009	0.0040
0.645	50797.50	0.4237	-0.4673	0.2253	-0.1500	0.0015	0.0080
0.653	49943.63	0.4946	-0.4361	0.2744	-0.1159	0.0011	0.0040
0.671	51056.62	0.4657	-0.4839	0.2640	-0.1650	0.0009	0.0140
0.723	50927.90	0.4251	-0.5203	0.2193	-0.1945	0.0028	0.0080
0.749	49970.74	0.4687	-0.4084	0.2651	-0.0870	0.0009	0.0040
0.796	49867.84	0.4310	-0.4647	0.2274	-0.1439	0.0008	0.0040
0.833	50644.66	0.3140	-0.4453	0.1120	-0.1262	0.0010	0.0070

Continued on Next Page. . .

Table 2.8 – Continued

Phase	**HJD - 2,400,000**	***%Q***	***%U***	**ISP sub % *Q***	**ISP sub % *U***	$\sigma_{\mathrm{i}}^{\mathrm{a}}$ **(%)**	$\sigma_{\mathrm{s}}^{\mathrm{a}}$ **(%)**
0.842	50644.77	0.2980	-0.4499	0.0959	-0.1305	0.0011	0.0070
0.848	49790.89	0.3819	-0.4402	0.1778	-0.1185	0.0014	0.0040
0.848	50644.86	0.2874	-0.4334	0.0851	-0.1131	0.0012	0.0070
0.862	49842.82	0.3860	-0.4130	0.1842	-0.0936	0.0010	0.0040
0.912	50645.68	0.3574	-0.3987	0.1543	-0.0783	0.0011	0.0070
0.920	50645.78	0.3495	-0.3898	0.1483	-0.0707	0.0014	0.0070
0.939	50749.54	0.4245	-0.5886	0.2219	-0.2686	0.0015	0.0080
0.955	49908.72	0.6552	-0.4704	0.4477	-0.1407	0.0039	0.0040
0.969	49947.72	0.5424	-0.4346	0.3401	-0.1159	0.0016	0.0040
0.980	50594.80	0.4749	-0.5607	0.2626	-0.2252	0.0059	0.0070

[a]The σ_i and σ_s columns represent internal and systematic errors respectively.

Table 2.9: HPOL Synthetic *I* Filter Data

Phase	**HJD - 2,400,000**	**%*Q***	**%*U***	**ISP sub % *Q***	**ISP sub % *U***	$\sigma_{\mathrm{i}}^{\mathrm{a}}$ (%)	$\sigma_{\mathrm{s}}^{\mathrm{a}}$ (%)
I Band Reticon:							
0.000	49663.46	0.3626	-0.5178	0.1859	-0.1806	0.0107	0.0200
0.121	48901.67	0.3121	-0.5255	0.1643	-0.2718	0.0210	0.0200
0.206	49562.62	0.2211	-0.3197	0.2852	-0.0712	0.0212	0.0200
0.292	49615.49	0.2800	-0.4636	0.1333	-0.1712	0.0147	0.0200
0.358	49564.59	0.2809	-0.3208	0.1720	-0.0486	0.0135	0.0200
0.368	49603.53	0.3388	-0.4346	0.1126	-0.0753	0.0167	0.0200
0.525	48984.52	0.2337	-0.3604	0.1426	-0.1002	0.0127	0.0200
0.657	48908.60	0.4512	-0.4725	0.2977	-0.3356	0.0278	0.0200
0.661	48895.71	0.3869	-0.4243	0.2265	-0.0991	0.0178	0.0200
0.668	49555.66	0.4397	-0.3904	0.3286	-0.1580	0.0090	0.0200
0.737	48922.58	0.2630	-0.2777	-0.2879	-0.0631	0.0139	0.0200
0.762	49194.60	0.3384	-0.4473	0.1821	-0.1987	0.0061	0.0200
0.890	49506.78	-0.3013	-0.9340	-0.4458	-0.6993	0.0649	0.0200
0.962	49533.59	0.4211	-0.5398	0.3808	-0.1714	0.0138	0.0200
I Band CCD:							
0.000	50685.64	0.3804	-0.5442	0.2091	-0.2734	0.0019	0.0080
0.004	50698.63	0.4507	-0.3146	0.2795	-0.0439	0.0014	0.0080
0.008	50685.74	0.3583	-0.5498	0.1870	-0.2790	0.0018	0.0080

Continued on Next Page...

Table 2.9 – Continued

Phase	**HJD - 2,400,000**	***%Q***	***%U***	**ISP sub % *Q***	**ISP sub % *U***	$\sigma_{\mathrm{i}}^{\mathrm{a}}$ **(%)**	$\sigma_{\mathrm{s}}^{\mathrm{a}}$ **(%)**
0.010	50698.71	0.4507	-0.3272	0.2794	-0.0564	0.0018	0.0080
0.011	50724.60	0.4749	-0.4690	0.3036	-0.1983	0.0014	0.0080
0.015	50685.83	0.3397	-0.5846	0.1683	-0.3138	0.0038	0.0080
0.019	50724.70	0.4457	-0.4810	0.2744	-0.2102	0.0017	0.0080
0.039	49935.68	0.3865	-0.4621	0.2152	-0.1913	0.0015	0.0070
0.043	49922.79	0.5194	-0.4285	0.3481	-0.1578	0.0016	0.0070
0.069	50647.71	0.3885	-0.3872	0.2171	-0.1163	0.0012	0.0080
0.073	50634.82	0.3375	-0.3073	0.1662	-0.0366	0.0011	0.0080
0.079	50686.66	0.2636	-0.4484	0.0923	-0.1777	0.0012	0.0080
0.086	50725.57	0.2855	-0.3658	0.1142	-0.0951	0.0013	0.0080
0.087	50712.64	0.2864	-0.3721	0.1150	-0.1013	0.0012	0.0080
0.117	49910.82	0.2913	-0.3028	0.1198	-0.0321	0.0010	0.0070
0.145	50661.64	0.2625	-0.3677	0.0912	-0.0968	0.0019	0.0080
0.184	49872.86	0.2252	-0.2967	0.0538	-0.0259	0.0012	0.0070
0.219	50636.72	0.2874	-0.3558	0.1159	-0.0849	0.0012	0.0080
0.226	50636.80	0.2898	-0.3749	0.1183	-0.1040	0.0011	0.0080
0.287	51025.78	0.2746	-0.3784	0.1034	-0.1078	0.0011	0.0220
0.300	51064.76	0.2952	-0.4062	0.1240	-0.1356	0.0017	0.0220
0.333	50922.86	0.3977	-0.4008	0.2263	-0.1298	0.0011	0.0060
0.354	50987.82	0.3203	-0.3821	0.1489	-0.1112	0.0010	0.0220
0.385	50690.62	0.3443	-0.3991	0.1731	-0.1284	0.0011	0.0080

Continued on Next Page. . .

Table 2.9 – Continued

Phase	**HJD - 2,400,000**	$\%Q$	$\%U$	**ISP sub** $\%$ Q	**ISP sub** $\%$ U	$\sigma_{\mathrm{i}}^{\mathrm{a}}$ (%)	$\sigma_{\mathrm{s}}^{\mathrm{a}}$ (%)
0.401	50703.77	0.2546	-0.3997	0.0833	-0.1289	0.0013	0.0080
0.403	50716.73	0.2897	-0.3675	0.1184	-0.0967	0.0020	0.0080
0.410	49901.66	0.2705	-0.2435	0.0991	0.0274	0.0013	0.0070
0.447	50639.67	0.2618	-0.2654	0.0902	0.0056	0.0012	0.0080
0.455	50639.77	0.2673	-0.2538	0.0959	0.0171	0.0012	0.0080
0.463	50639.87	0.2749	-0.2538	0.1035	0.0171	0.0013	0.0080
0.483	50316.65	0.3544	-0.3245	0.1829	-0.0535	0.0010	0.0200
0.485	49863.82	0.2575	-0.2304	0.0861	0.0405	0.0012	0.0070
0.486	50769.56	0.2740	-0.3214	0.1030	-0.0509	0.0014	0.0080
0.525	50640.68	0.3033	-0.3901	0.1319	-0.1192	0.0018	0.0080
0.534	50640.79	0.2402	-0.3920	0.0689	-0.1213	0.0013	0.0080
0.559	49864.78	0.5150	-0.4246	0.3438	-0.1540	0.0022	0.0070
0.572	49916.70	0.3529	-0.3019	0.1815	-0.0309	0.0011	0.0070
0.645	50797.50	0.3609	-0.3924	0.1897	-0.1218	0.0016	0.0080
0.653	49943.63	0.3998	-0.3541	0.2285	-0.0833	0.0011	0.0070
0.671	51056.62	0.3735	-0.4160	0.2021	-0.1452	0.0010	0.0220
0.723	50927.90	0.2960	-0.4475	0.1246	-0.1766	0.0025	0.0060
0.749	49970.74	0.3880	-0.3424	0.2166	-0.0715	0.0009	0.0070
0.796	49867.84	0.3552	-0.3721	0.1839	-0.1013	0.0009	0.0070
0.833	50644.66	0.2470	-0.3595	0.0756	-0.0886	0.0011	0.0080
0.842	50644.77	0.2378	-0.3646	0.0665	-0.0937	0.0012	0.0080

Continued on Next Page...

Table 2.9 – Continued

Phase	**HJD - 2,400,000**	***%Q***	***%U***	**ISP sub % *Q***	**ISP sub % *U***	$\sigma_{\mathbf{i}}^{\mathbf{a}}$ **(%)**	$\sigma_{\mathbf{s}}^{\mathbf{a}}$ **(%)**
0.848	49790.89	0.2912	-0.3398	0.1198	-0.0689	0.0018	0.0070
0.848	50644.86	0.2267	-0.3582	0.0553	-0.0873	0.0014	0.0080
0.862	49842.82	0.3112	-0.3377	0.1400	-0.0670	0.0011	0.0070
0.912	50645.68	0.3068	-0.3286	0.1354	-0.0577	0.0014	0.0080
0.920	50645.78	0.2922	-0.3419	0.1210	-0.0712	0.0012	0.0080
0.939	50749.54	0.3517	-0.4706	0.1803	-0.1997	0.0014	0.0080
0.955	49908.72	0.5040	-0.3810	0.3327	-0.1102	0.0059	0.0070
0.969	49947.72	0.4425	-0.3480	0.2715	-0.0772	0.0015	0.0070

[a]The σ_i and σ_s columns represent internal and systematic errors respectively.

Table 2.10: Position Angle Information for β Lyrae

Band	**HPOL Reticon (deg)**	**HPOL CCD (deg)**	**AH (deg)**	**FCO (deg)**
B	139.8 ± 3.5	165.0 ± 0.7	169.8 ± 1.7	165.1 ± 0.9
V	147.3 ± 3.0	164.0 ± 0.5	171.8 ± 1.0	163.1 ± 0.4
R	158.4 ± 0.4	158.3 ± 0.4	···	162.2 ± 0.7
I	57.3 ± 3.0	162.7 ± 0.6	···	···
Index	158.8 ± 0.6	142.1 ± 1.7	···	···
Hα	···	47.9 ± 9.7	···	···
Hβ	···	71.1 ± 2.5	···	···
He Iλ5876	···	63.8 ± 6.4	···	···
He Iλ7065	···	51.0 ± 3.2	···	···
He Iλ6678	···	138.2 ± 6.6	···	···

Note. – These values were calculated by fitting a line in *Q*-*U* space to the data, excluding points between phases 0.475 and 0.525. For the HPOL data, we used systematic errors in both *Q* and *U* in the least-squares fit calculation for all bands except the Balmer jump index (the vector difference between the polarization above and below the Balmer jump) and the lines, for which we used the intrinsic errors. See Sections 2.3.1 and 2.3.2.

projected Stokes parameter $\%Q_p$ resulting from this rotation. The use of this quantity is beneficial because it can be positive or negative, whereas $\%P$ is always positive. Data points that have a position angle near 164° will have a positive $\%Q_p$ value while points with a position angle perpendicular to this (near 74°) will have a negative $\%Q_p$. Hereafter we display only $\%Q_p$ because $\%U_p$ values scatter around zero. Because the rotation is a simple trigonometric calculation, we present in Tables 2.3 through 2.9 the unrotated $\%Q$ and ISP subtracted FCO and HPOL data only.

The middle panels in Figures 2.1 through 2.4 show the $\%Q_p$ curves for the *BVRI* bands after rotation. We used the program PERIOD04 to perform a Fourier fit to the data for each band (Lenz & Breger 2005). The PERIOD04 fitting formula is $y = Z + \sum_{i=1}^{n} A_i \sin(2\pi(\Omega_i t + \phi_i))$ where *n* is the number of sine terms in the fit, *Z* is the zero point, *A* is the amplitude, Ω is the frequency, and ϕ is the phase. The results of the fits are displayed as solid curves in each figure and their parameters are given in Table 2.11. The *V* band, and to a lesser extent the *B* band, Fourier fits deviate from the data at phase 0.9 (see Figure 2.2). This discrepancy disappears in the *V* band if we include three frequency terms in the Fourier fit. However, we are not as confident in the third frequency as we are in the first two because the PERIOD04 fitting program produces a reasonable third term for the *V* band only. Therefore, in Table 2.11 we report parameters for only the first two terms, but we display both the two-term and three-term fits in Figure 2.2. These fits provide the first quantitative representations of the polarization variations in the β Lyr system.

The data in the *BVRI* bands are almost always positive, indicating their position angles stay near 164° throughout the orbital period. Each of the bands displays an increase in $\%Q_p$ at primary eclipse and two other increases near the quadrature phases (0.25 and 0.75). The height difference between the polarization bumps at

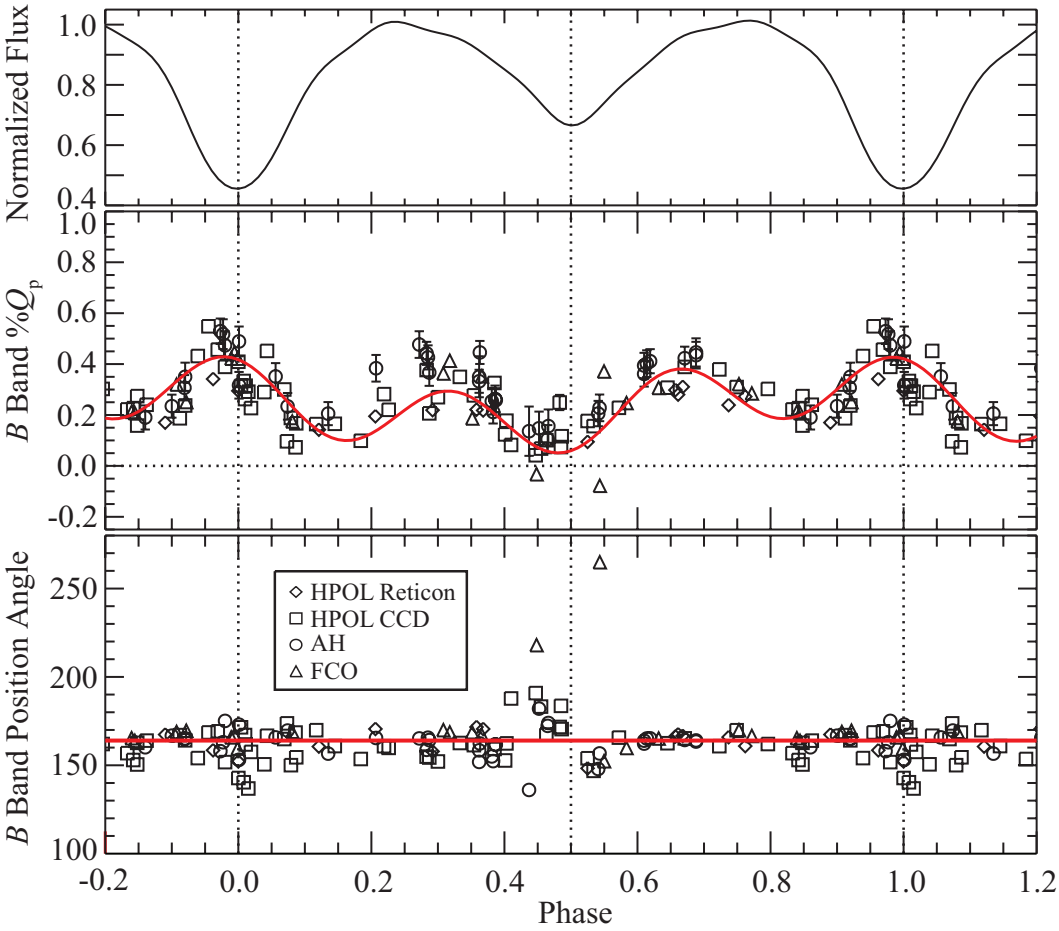

Figure 2.1 Data points represent the *B* band polarimetric observations from HPOL Reticon (diamonds), HPOL CCD (squares), AH (circles) and FCO (triangles). *From top:* Normalized *V* band Fourier fit light curve (Harmanec et al. 1996), projected polarization (see Section 2.3.1), and position angle (degrees) versus phase. Error bars are shown for uncertainties larger than 0.025 in $\%Q_p$ and 5.0° in position angle. The HPOL error bars shown represent the larger of the intrinsic and systematic uncertainties. All data have been wrapped so that more than one complete period is shown. The solid line in the middle panel represents our Fourier fit to the $\%Q_p$ data (see Section 2.3.1). The dotted line represents zero projected polarization. The solid line in the bottom panel represents the average position angle of 164°.

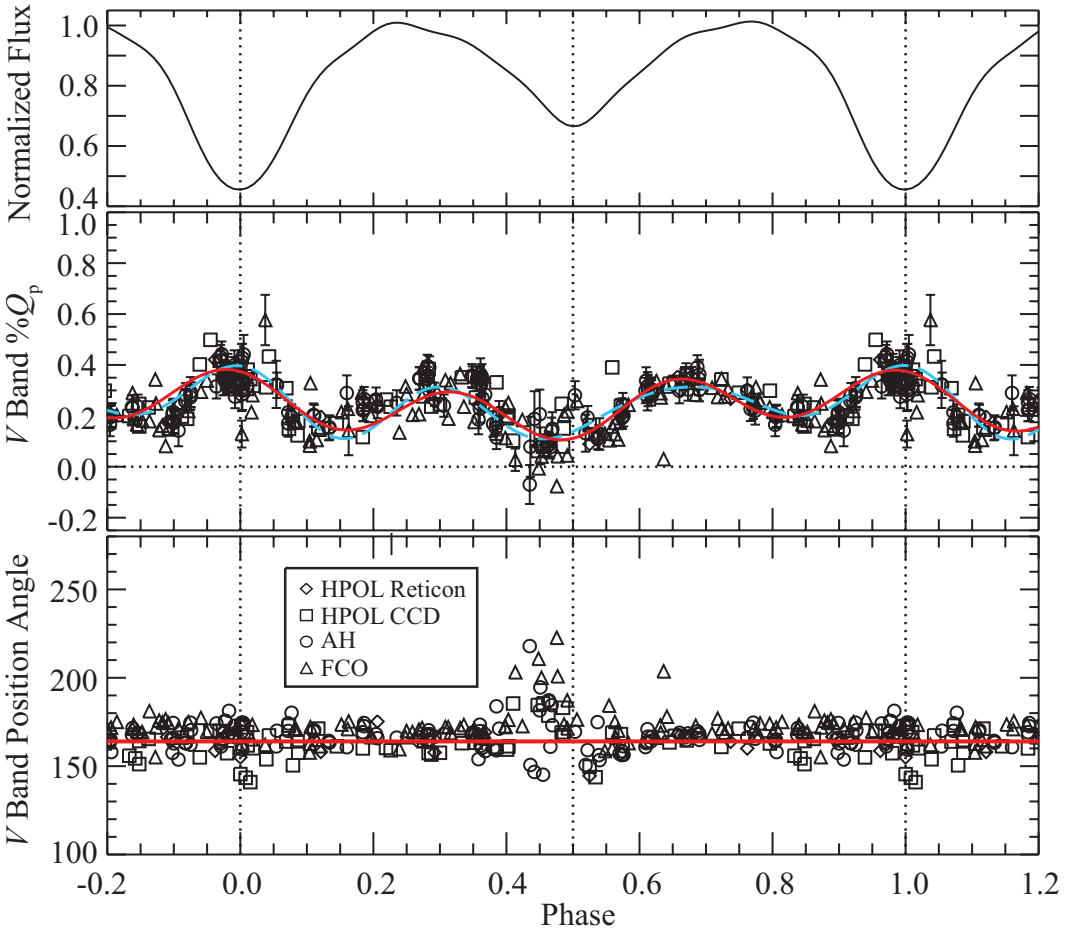

Figure 2.2 Same as Figure 2.1, but for *V* band polarimetry. The dashed blue curve (in the online version, otherwise dashed light grey) represents the three-term Fourier fit and the red curve (in the online version, otherwise solid) represents the two-term Fourier fit. Note the two fits differ at primary and secondary eclipse, the quadrature phases, and near phases 0.15 and 0.9.

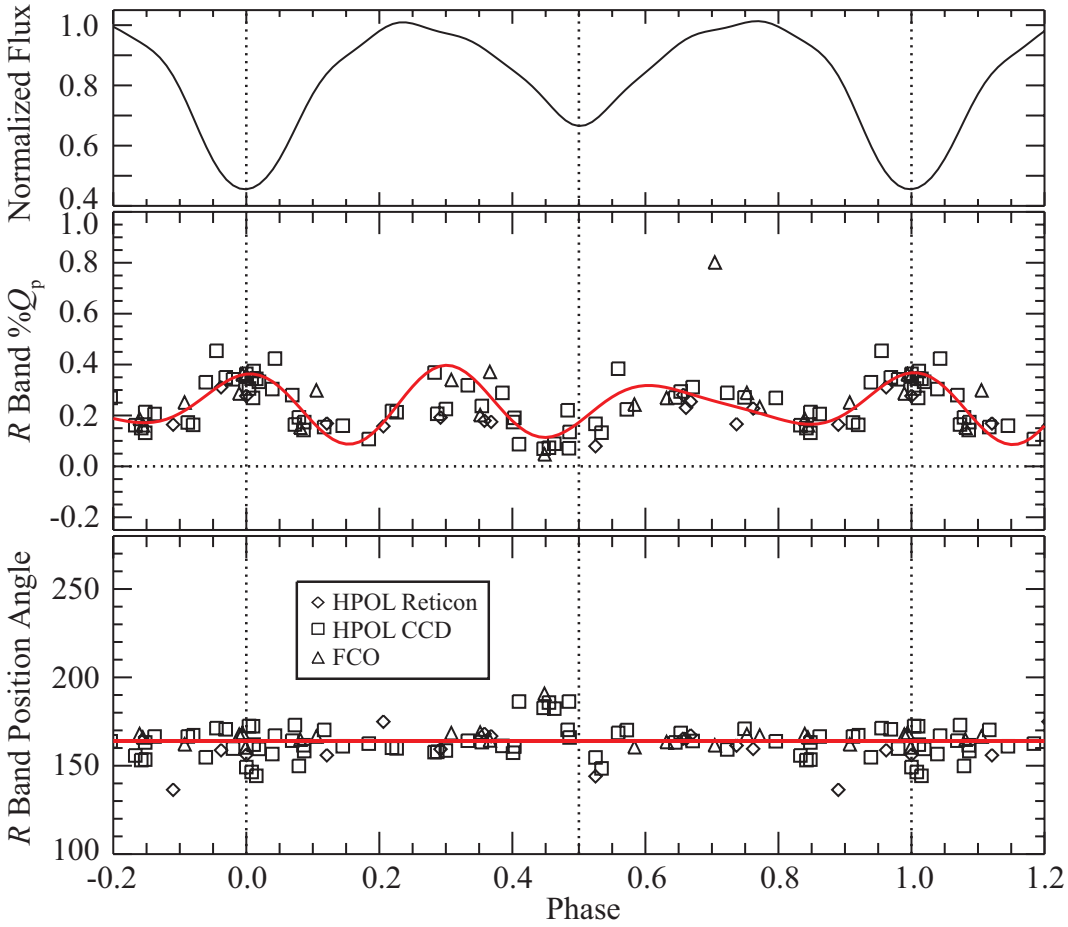

Figure 2.3 Same as Figure 2.1, but for *R* band polarimetry.

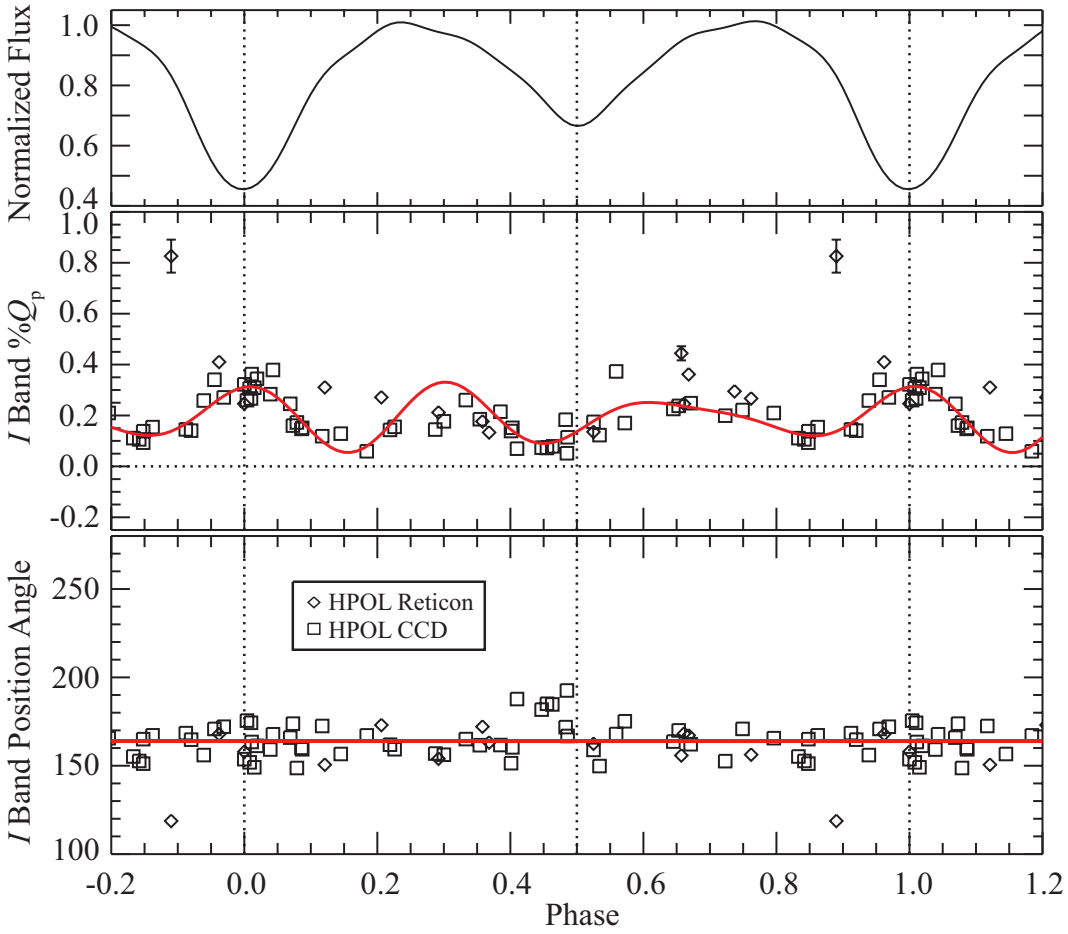

Figure 2.4 Same as Figure 2.1, but for *I* band polarimetry.

the quadrature phases noted by HNF disappears now that more data are added, but we note that the *B* and *V* phase 0.25 bump have a higher dispersion around the average $\%Q_p$ value than does the 0.75 phase bump. The *R* and *I* band show the opposite behavior; future observations will be able to tell us whether this is due to their poor phase coverage or whether it indicates that the *R* and *I* bands are probing a different region of the disk than the *B* and *V* bands. We calculated the variance of the two quadrature bumps between phases 0.25 and 0.35, and 0.65 and 0.75 to formally show this. The first quadrature bump has *BVRI* variances of 0.081 $\pm$ 0.006, 0.110 $\pm$ 0.005, 0.040 $\pm$ 0.002, and 0.016 $\pm$ 0.002 respectively, while the second quadrature bump has variances of 0.048 $\pm$ 0.005, 0.027 $\pm$ 0.002, 0.281 $\pm$ 0.005, and 0.069 $\pm$ 0.004.

Table 2.11: *BVRI* Fourier Fit Parameters

Band	**Zero Point**	**Term**	**Ω**	***A***	ϕ
B	0.239470	1	2.98 ± 0.01	0.127 ± 0.009	0.30 ± 0.01
	···	2	1.00 ± 0.02	0.078 ± 0.008	0.37 ± 0.02
V	0.243419	1	2.98 ± 0.01	0.096 ± 0.007	0.30 ± 0.01
	···	2	1.01 ± 0.03	0.050 ± 0.006	0.36 ± 0.02
R	0.241148	1	3.00 ± 0.01	0.107 ± 0.008	0.32 ± 0.01
	···	2	4.02 ± 0.03	0.052 ± 0.009	0.08 ± 0.03
I	0.195021	1	3.00 ± 0.01	0.093 ± 0.006	0.30 ± 0.01
	···	2	4.01 ± 0.02	0.050 ± 0.006	0.10 ± 0.02

Note. – These parameters describe our Fourier fits to the broadband polarimetric data in the combined HPOL, FCO and AH data sets. See Section 2.3.1.

The *R* and *I* bands also produce a lower polarization signal than the *B* and *V* bands. This change in polarization behavior with wavelength could indicate that scattering mechanisms other than electron scattering are present in the system. However, more observations in the *R* and *I* bands are needed to rule out the possibility that the low signal is due to a lack of phase coverage in these bands.

Figures 2.1 through 2.4 also show that in each band, the polarization curve has a fitted minimum in polarization that occurs just prior to the secondary eclipse in total light. This minimum is accompanied by a rotation in the position angle of the polarized light away from its average value. Table 2.12 gives the phases of the $\%Q_P$ Fourier fit minimum in all bands. The offset between secondary eclipse in polarized light and total light is a new result, seen here for the first time due to the improved phase coverage in these data. We discuss the implications of this phenomenon in Section 2.4.

At primary eclipse, there are hints of similar behavior: the polarization maxima in the *B* and *V* bands occur slightly before phase 0.0, and all bands show a deviation from the mean position angle at and just after phase 0.0. However, we consider the primary eclipse features to be less significant than the ones at secondary eclipse for the following reasons. The three data points showing noticeable deviations from the mean position angle all occurred on the same night, 1997 August 25, which suggests that this effect may be due to a non-periodic process intrinsic to the β Lyr system, or to a change in observing conditions that affected that night's data. If the same structure is responsible for the phenomena at both eclipses, we expect that a similar position angle scatter should exist in observations from the same orbit of the system whose phases are between primary and secondary eclipse, when such a structure should be most visible to the observer. However, neither the data from

1997 August 26, nor 1997 August 30 show such behavior. Additionally, the polarization maximum in the *R* band occurs at phase 0.0 within the uncertainties, and in the *I* band the maximum occurs just after phase 0.0. If we include the third term in the *V* band Fourier fit, the primary polarization maximum occurs at phase 0.0 within uncertainties. Because the eclipse behavior is not consistent between bands and the associated position angle scatter appears to have occurred during only one orbit of the system, we consider it unlikely that these are due to a stable physical structure within the system (see Section 2.4 for further discussion of the effects seen at primary eclipse).

Figure 2.5 displays the projected polarized *BVRI* flux light curves for the β Lyr system. To create these polarized light curves, we multiplied the fitted polarization curves shown in Figures 2.1 through 2.4 by their respective Fourier fit light curves (Harmanec et al. 1996) normalized to maximum light. In all bands, the polarized flux remains nearly constant across primary eclipse due to a decrease in total light and an increase in $\%Q_P$. The secondary eclipse offset seen in Figures 2.1 through 2.4 persists in Figure 2.5, while quadrature phases display local maxima. The *B* and *V* band appear to be the most similar; they overlap for most phases, while outside of secondary eclipse and the first quadrature phase the *R* and *I* bands produce the lowest net projected polarized flux. We do not consider the apparent height differences between bands at the quadrature phases to be significant due to the scatter in the observational points and the lack of coverage in the *R* and *I* bands.

2.4.2 Line Polarimetry

We also took advantage of the spectropolarimetric nature of the data by studying the polarization behavior of the strongest optical emission lines in β Lyr's spectrum:

Hα, Hβ, He I λ5876, He I λ6678, and He I λ7065. HNF hypothesized that the Hα, Hβ, He I λ5876 and He I λ7065 lines, which show a negative projected polarization, scatter in the bipolar outflow, while the He I λ6678 scatters on the edge of the disk. However, HNF did not have enough data to construct a full polarization phase curve for the lines. Our expanded data set allows us to do this. However, we present only our He I λ5876 results in graphical form because our uncertainties are relatively large due to signal-to-noise limitations. Rather than present the Hα, Hβ, He I λ6678, and He I λ7065 data, we describe their general behavior below. Future observations will allow us to use these data to draw quantitative conclusions about the scattering regions that give rise to the polarization in these lines.

In order to calculate the polarization for each emission line, we used the flux equivalent width method described by HNF, using the same line and continuum regions as far as possible. We corrected the Hα and Hβ lines for underlying unpolarized absorption components (arising from the loser) in the same manner as HNF, using their preferred absorption equivalent widths of 8 ± 2 Å for Hα and 6 ± 1 Å for Hβ. This has the following effect on the data. The continuum is positively polarized while the lines are negatively polarized. If we do not correct for unpolarized absorption, we remove too much continuum, and thus our resulting line polarization is too negative. With the absorption correction, the continuum contribution is smaller and the magnitude of the polarization is also smaller, resulting in a less negative $\%Q_p$.

We do not present the HPOL Reticon line polarization values due to their large uncertainties. Figure 2.6 shows $\%Q_p$ and position angle curves for the He I λ5876 line. It has a negative $\%Q_p$; thus its position angle is perpendicular to the intrinsic axis of the system. In addition, the polarization for the line approaches zero at both

primary and secondary eclipses. For this to happen, the scattering region for this line must lie near enough to the orbital plane of the system to be occulted both by the loser and by the disk. HNF previously suggested that this line scatters in the bipolar outflows because its average position angles lie near $74°$, corresponding to negative values of $\%Q_P$. The results from our extended data set support this interpretation and further suggest that the He I λ5876 scattering region within the outflows must lie between the loser and the disk and have a vertical extent comparable to the height of the disk.

The Hα, Hβ, and He I λ7065 lines also all display a negative $\%Q_p$ and are likely scattered in the same region as the He I λ5876 line. Their average position angles are listed in Table 2.10.

The He I λ6678 data show a polarization behavior different from that of the other lines. The data are generally positively polarized and their average position angle, $138.2°$, agrees more closely with the intrinsic axis of the system than do those of the other emission lines (see Table 2.10).

2.4.3 Period Analysis

Besides the primary orbital period of β Lyr (12.9 days), analysis of light curves has revealed several longer periodicities. A 340-day period was detected by Peel (1997), while both Van Hamme et al. (1995) and Harmanec et al (1996) detected a 282-day period. Wilson and Van Hamme (1999) searched polarimetry from AH, HNF, Serkowski (1965), and Shulov (1967) for periodicities but did not detect anything significant.

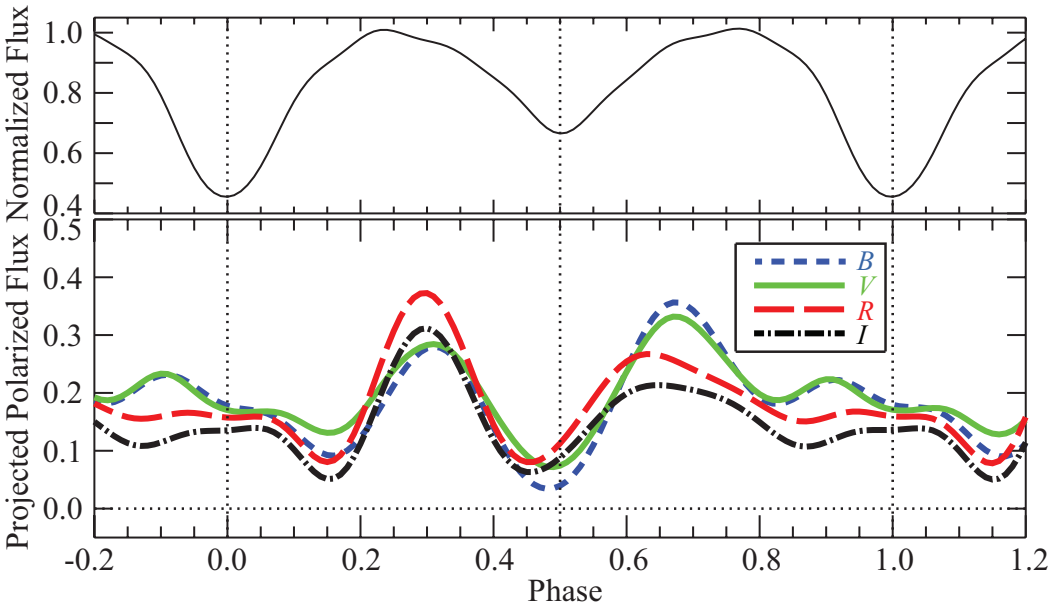

Figure 2.5 *From top:* Normalized *V* band Fourier fit light curve and projected polarized flux curves for the *BVRI* bands (see Section 2.3.1). The projected polarized flux curves are formed by multiplying each band's Fourier fit polarization curve by its normalized to maximum light Fourier fit light curve.

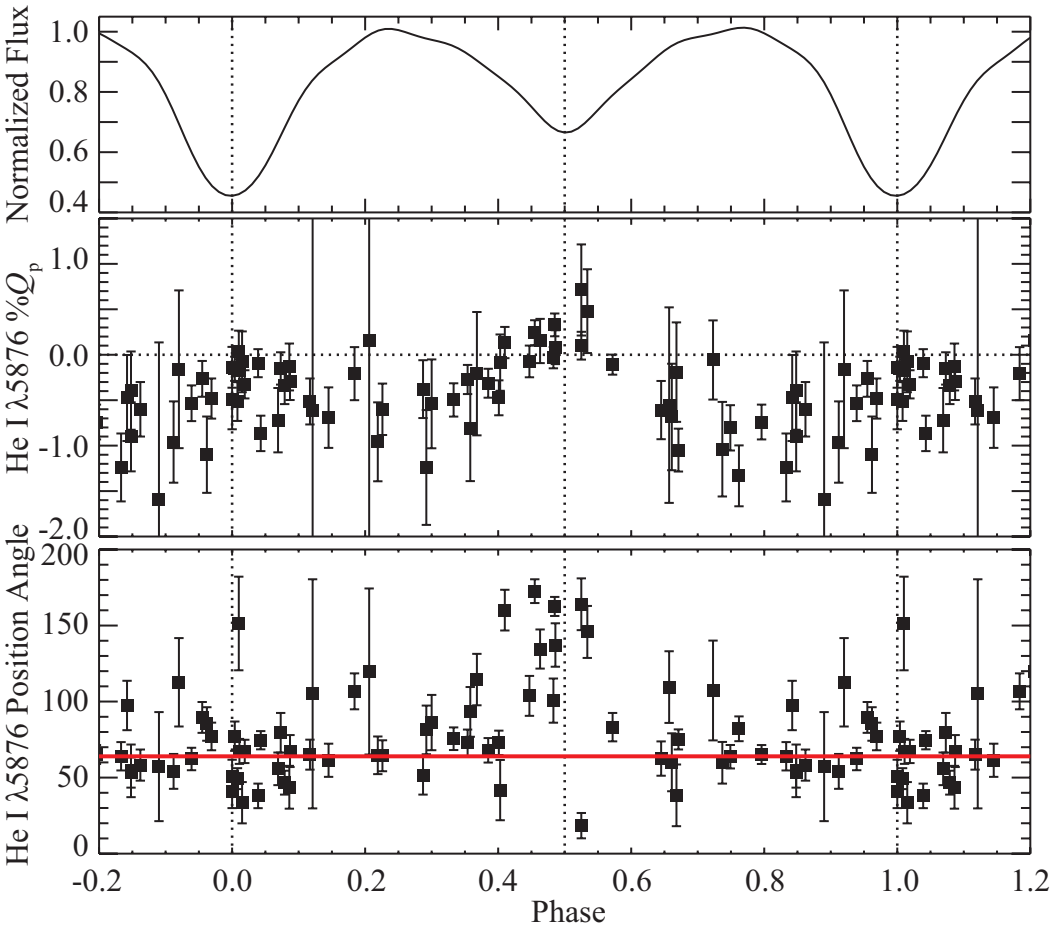

Figure 2.6 He I λ5876 emission line polarization from HPOL CCD observations (see Section 2.3.2). *From top:* Normalized *V* band Fourier fit light curve (Harmanec et al. 1996), projected polarization, and position angle (degrees) versus phase. Error bars represent intrinsic uncertainties. All data have been wrapped in phase to display more than one complete period.

Table 2.12: Broadband Secondary Eclipse Phases and Maximum Hot Spot Size

Band	**Phase**	**Min PA Phase Rot**	**Max PA Phase Rot**	**Hot Spot Size in Phase**	$\mathbf{qf_{DC}}$
B	0.481 ± 0.004	0.448	0.543	0.095	0.186
V	0.481 ± 0.004	0.385	0.554	0.169	0.184
R	0.449 ± 0.005	0.448	0.524	0.076	0.171
I	0.449 ± 0.004	0.448	0.524	0.076	0.140
Band	$\mathbf{qf_{min}}$	$\mathbf{HS_Q}$	$\mathbf{HS_{PA}}$	$\mathbf{HS_{SM}}$ **(i** $= 90°$**)**	$\mathbf{HS_{SM}}$ **(i** $= 86°$**)**
B	0.045	22 $R_\odot$	33 $R_\odot$	31 $R_\odot$	26 $R_\odot$
V	0.080	22 $R_\odot$	58 $R_\odot$	18 $R_\odot$	9 $R_\odot$
R	0.080	33 $R_\odot$	26 $R_\odot$	19 $R_\odot$	10 $R_\odot$
I	0.077	33 $R_\odot$	26 $R_\odot$	12 $R_\odot$	2 $R_\odot$

Note. – Columns two through six are parameters used in the three hot spot size estimates (see Sections 2.4.1, 2.4.2, and 2.4.3). Flux normalized to maximum light was used for qf_{DC} and qf_{min}. The last four columns represent the width of the hot spot calculated using our different estimates (see Section 2.4). All three polarimetric data sets were used in this analysis and the resulting estimates.

We performed a Lomb-Scargle power spectrum analysis to search for any periodic behavior in our polarimetric broadband (HPOL, AH, and FCO) and line data (Hα and He I λ 5876) not associated with the 12.9 day orbital period of the system. While none of the previously detected longer periods were found, our analysis indicates the presence of periods of approximately 4.3 days in both the *V* and *B* bands with a False Alarm Probability (FAP; Horne & Baliunas 1986) of 10^{-6} when using all three data sets. None of the other bands or the line polarization data appear to contain periods other than the orbital period. We also searched for periods within the HPOL, AH and FCO data sets individually to look for any transient periodic variations. We find that the 4.3 day period also appears in the *V* and *B* AH data set with a FAP of 10^{-6}, but it does not appear in the other two data sets. This period is exactly one third of the 12.9-day orbital period of the β Lyr system and results from the combination of two separate effects: the increase in polarization at the quadrature phases due to light scattering off the disk edge and the increase in polarization at primary eclipse due to the occultation of unpolarized light by the loser (Hoffman et al. 2003; hereafter HWN). These two effects cause the $\%Q_p$ curves to form a complete cosine curve between phases 0.0 and 0.3, a second cosine curve between phases 0.3 and 0.6 and a third cosine between 0.6 and 1.0 (see Figures 1 through 4). Therefore, this period does not provide new information about the β Lyr system.

We also performed a much simpler analysis to search for signatures of the 282-day period, which has been ascribed to variability of the conditions of the circumstellar and circumbinary gas (Wilson 1974, Ak et al. 2007). Time plots of $\%Q_p$, $\%U_p$, position angle, and percent polarization for each of the *BVRI* bands and the He I λ5876 line did not reveal the 282-day period and are therefore not shown. However, the time coverage of our observations is very uneven and could have pre-

vented us from detecting variations on this time scale. The observations in our data set were taken between 1964 and 1998, but we have no polarimetric observations taken during 1990, 1991, or between 1966 and 1987. The number of observations performed per year only adds further complications; several years have very few observations. We also note that the only the HPOL data set has observations of every band and the He I λ5876 line. For these reasons, we also performed an analysis similar to Harmanec et al. (1996) on the $\%Q_p$ data for each band and the He I λ5876 line. Plotting the data on the 282.37 day period mitigates the lack of time coverage by "folding" observations onto one cycle.

We plotted the data from selected orbital period phase bins versus their phase on the 282.37 day period (see Harmanec et al. 1996 for a similar analysis of a large amount of *V* band total-light photometry). We chose the following five orbital phase bins for several reasons: the 0.0-1.0 bin allows us to use all of the data, the 0.6-0.15 bin is where Harmanec et al. (1996) detected the 282.37 day period the most strongly, the 0.25-0.35 and 0.65-0.75 bins allow us to determine whether the polarization of the quadrature phases changes on a 282.37 day time scale, and the 0.425-0.575 bin allows us to determine whether the secondary eclipse has a 282.37 day periodic behavior. The 0.25-0.35, 0.425-0.575, and 0.65-0.75 orbital period bins are too tight to leave a useful number of observations in the *R* and *I* bands and the He I λ5876 line. While the *B* and *V* bands are slightly less affected by the size of the 0.25-0.35, 0.425-0.575, and 0.65-0.75 orbital phase bins, their behavior does not indicate, by eye or by using PERIOD04, the presence of a variation on a 282.37 day period. The size of the 0.6-0.15 and 0.0-1.0 bins present the best chance of detecting this period because the amount of data is not severely reduced. However, neither bin reveals the presence of the 282.37 day period. We also subtracted the

Fourier fits from the data in the *BVRI* bands (see Section 2.3.1) and searched the residuals for the 282.37 day period with the same bins used for the original $\%Q_p$ data. The analysis on the residuals produced similar results; we do not find evidence of a 282.37 day period in either the $\%Q_p$ data or the Fourier fit subtracted residuals. However, we note that the Fourier fits deviate from the data at some phases (see Section 2.3.1). Plots from this analysis resemble scatter plots and are therefore not shown.

2.5 Discussion

In interpreting their polarized flux curves, HNF proposed two different possibilities for the origin and scattering location of the visible light. In their "disk-disk" case, this light arises from within the disk and scatters from the disk edge; in the "loser-lobe" case, the *V*-band continuum light arises from the loser and scatters from material between the loser and the disk. In this analysis, HNF implicitly assumed that all features of the visible polarized flux curve are due to the same origin and scatterer. However, modeling work by HWN and subsequent modeling results (Hoffman et al., in prep.) have shown that the scattered light can originate both from the loser and from the disk in differing proportions over the binary cycle. These newer results suggest the following interpretations of our *BVRI* polarization curves. The net increase in $\%Q_p$ at primary eclipse (Figures 2.1-2.4) is the result of the unpolarized light from the primary star being blocked by the disk material at phase 0.0. HNF interpreted the increase in $\%Q_p$ at the quadrature phases as arising in one of two ways: light originating from within the disk and scattering from the disk edge, or light originating from the loser and scattering from material be-

tween the stars. We propose, based on recent modeling work by Hoffman, that these "quadrature bumps" form simply by loser light scattering from the disk edge. The minimum at secondary eclipse occurs because the unpolarized primary star blocks light scattered in the secondary component.

Near secondary eclipse in all four broadband $\%Q_p$ curves, the minimum in polarization precedes the minimum in total light; the phases for the polarization minimum in the *BVRI* bands are listed in Table 2.12. In each band, this minimum corresponds to a rotation in position angle away from the average value; the phase ranges for this rotation are also listed in Table 2.12. In the basic star-star-disk model for the system, there is no mechanism to produce this disparity. If the loser is an unpolarized source, as indicated by the absence of a primary eclipse in the polarized flux curves (Figure 5; HNF), then the polarization minimum produced by its transit across the disk should be centered at flux minimum (phase 0.5; HWN). Thus, to explain this offset, we need to invoke another system component. Since β Lyr is a mass transfer system, it most likely contains a mass stream connecting the loser and the disk as well as a 'hot spot' where the mass stream from the loser interacts with the disk edge (Lubow & Shu 1975; see also the geometries proposed by HNF). Some studies (for example, Bisikalo et al. 2000 and references therein) suggest that the manner in which the mass stream approaches the disk prevents a hot spot from forming. Instead, a portion of the stream makes a full revolution around the disk and then interacts with the original stream. The process of this interaction allows the material that has made a full revolution around the secondary star to become part of mass stream again; Bisikalo et al. (2000) do not consider it to be part of the disk. Since this material's position angle is the same as the disk in the system, polarimetry cannot distinguish between the two possibilities. Therefore, we use the

term ‘hot spot’ to refer to the region where the mass stream interacts with material already encircling the secondary star and assume that any material which has completed a revolution around the secondary star is part of the disk.

Even if a true “hot spot” is not created by the mass stream-disk interaction, the region where the stream and disk meet could potentially decrease observed polarization from the disk edge by disrupting the otherwise smooth structure of the disk edge and adding unpolarized light at phases when it is visible. On the other hand, the mass stream, which is elongated in the same direction as the disk, should produce a polarization position angle very similar to that of the disk. Therefore, the presence of the mass stream should not lead to a decrease in the observed polarization. The effects of a hot spot would be detectable in the polarization light curves in the *BVRI* bands because the disk is the primary scattering region for visible light in the β Lyr system. But, if it is not significantly brighter than the surrounding disk, the hot spot would not be visible in the total light curves. Therefore, we interpret the $\%Q_p$ minimum associated with the randomization of the polarized position angle prior to secondary eclipse as the first direct evidence for the proposed hot spot on the β Lyr disk edge (Lubow & Shu 1975, Harmanec 2002).

We expect the hot spot to create an unstructured region on the disk edge where the polarization vectors of the scattered light are randomized in position angle. When this part of the disk is visible, the hot spot should cause a decreased polarization signal and a rotation in position angle, both of which occur in our polarization curves (Figures 2.1-2.4). As long as the hot spot does not lie on the line connecting the centers of mass of the two stars, and its brightness in the visible continuum is similar to that of the undisturbed disk, its effect should result in a minimum in polarization that does not correspond to a minimum in flux. Hydrodynamical mod-

eling of the β Lyr system indicates that the mass stream, and therefore its associated hot spot, should lead the loser in the sense of rotation of the system (Lubow & Shu 1975, Nazarenko & Glazunova 2006). In the β Lyr polarization curves, the polarization minimum and concurrent position angle variation occur just before secondary eclipse, suggesting that the hot spot begins its transit of the disk before the loser does. In fact, the larger dispersion of points in the *B* and *V* bands at the first quadrature phase when compared to the second quadrature phase suggests that the hot spot is already in view by phase 0.25. In this picture, the minimum polarization occurs at the phases where the disk area disrupted by the hot spot and eclipsed by the loser is maximized. We sketch this proposed interpretation in Figure 2.7.

We note that in all bands, there are fewer data points after secondary eclipse than before, which may skew the $\%Q_P$ Fourier fit near secondary minimum. However, we have several reasons to believe the eclipse offset is not an artifact of the fit. The effect is apparent in all filters, some of which have a much lower point density in phase then the *V* band. (However, the *V* band displays the smallest difference between the $\%Q_P$ near secondary minimum and phase 0.5.) The position angle rotation does not heavily depend on the number of points, is apparent in all bands, and has a larger effect at pre-secondary eclipse phases than post-secondary eclipse phases. Finally, the uncertainties on the phases at which the minima occur are small (see Table 2.12) compared to the difference between phase 0.5 and the polarization secondary minimum. Future work will include filling in the post-secondary data gap with new HPOL observations to improve the Fourier fits and quantify the $\%Q_P$ near secondary minimum offsets more reliably.

In the subsections below, we outline three different estimates of the size of the hot spot, assuming it has the same height as the edge of the disk. We use the

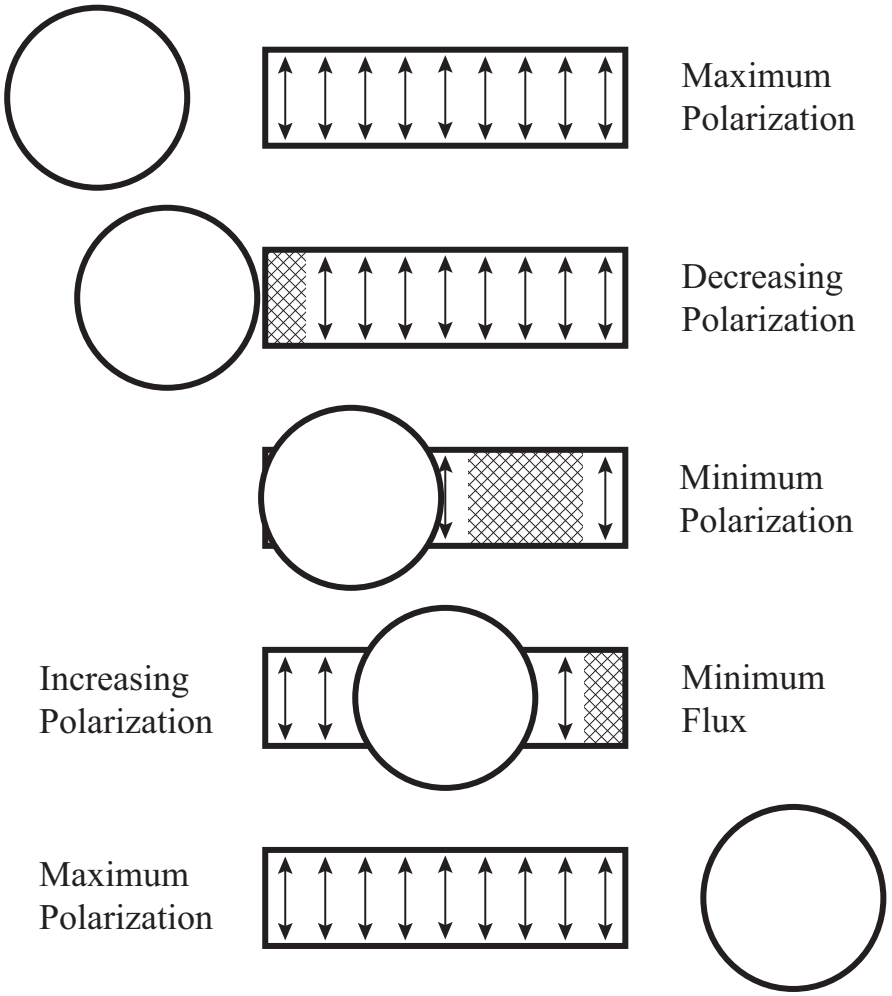

Figure 2.7 Proposed geometry of the β Lyr system at various phases in our proposed hot spot model. Arrows represent the polarization arising from the disk edge. *From Top:* The first maximum in polarization occurs at the first quadrature phase. The polarization then begins to decrease as the hot spot (hatched region) rotates into view. The minimum in polarization occurs when the area eclipsed by the loser and disrupted by the hot spot is maximized. The minimum in flux occurs as the hot spot is rotating off the edge of the visible disk. The second maximum in polarization occurs at the second quadrature phase.

following values for system parameters: a loser radius of $R_L = 15R_\odot$, a disk diameter of $D_D = 60R_\odot$, a binary separation of $R_S = 58R_\odot$, and a disk height of $H_D = 16R_\odot$ (Linnell 2000, Harmanec 2002).

2.5.1 Hot Spot Size Estimate: $\%Q_P$ Method

We can use the offset in secondary eclipse to estimate a maximum size for the hot spot. Assuming circular orbits, we have the scenario depicted in Figure 2.8. Knowing that phase 0.5 occurs at an angle of 180° on the circle depicting the loser's orbit, we can use a simple ratio to find the angle θ,

$$\frac{0.5}{180^\circ} = \frac{P}{180^\circ - \theta} \tag{2.5.1}$$

where P is the phase for which secondary eclipse occurs in polarized light (Table 2.12) and $180^\circ - \theta$ is the angle from zero at which phase P occurs. If we know θ, we can also find the length of line x,

$$x = R_S \sin(\theta) \tag{2.5.2}$$

where R_S is the radius between the center of the disk and the center of the loser. With the length of line x we can estimate the projected size of the hot spot, HS_Q (hatched region in the Observer's View in Figure 2.8), with the following equation,

$$HS_Q = \begin{cases} 60R_\odot & \text{for } x \geq \frac{1}{2}D_D, \\ (x - R_L) + \frac{1}{2}D_D & \text{for } \frac{1}{2}D_D > x > R_L, \\ \frac{1}{2}D_D - (R_L - x) & \text{for } R_L > x > 0 \end{cases} \tag{2.5.3}$$

where D_D is the diameter of the accretion disk and R_L is the radius of the loser.

Using the above formulae we can calculate the maximum projected hot spot size for the *BVRI* bands. Table 2.12 lists the results. The maximum hot spot size ranges from 22 $R_\odot$ to 33 $R_\odot$. Since we assume the hot spot has the same height as the disk, these values represent 'widths' along the projected face of the disk. We do not calculate formal error bars on these estimates because the estimates vary so widely.

2.5.2 Hot Spot Size Estimate: Position Angle Method

We also used the variations in position angle to estimate a maximum size for the hot spot. First, we calculated the size of the disk in phase. To do this we solved Equation 2 for θ when $x = \frac{1}{2}D_D$. The phase for the left side of the disk as depicted in Figure 2.8 is then given by Equation 1. We calculate this phase to be 0.413. Similarly for the right side of the disk we calculate a phase of 0.587. The resulting size of the disk in phase is the difference of these phases, or 0.174.

We then estimated the size of the hot spot in phase by finding how long the randomization of position angle lasts. We assumed any points near secondary eclipse that deviated significantly from the average position angle were due to the hot spot. We did not use a formal calculation to find these points; we chose the smallest and largest phases for the randomized position angles by eye. We then took the difference in phase between the deviant observations with the smallest and largest phases

to calculate the size of the hot spot in phase, θ_{HS} (Table 2.12). In this case the maximum hot spot size, HS_{PA}, is given by the ratio

$$\frac{60R_{\odot}}{0.174} = \frac{HS_{PA}}{\theta_{HS}}. \tag{2.5.4}$$

Table 2.12 lists the maximum projected size of the hot spot across the edge of the disk for each band. Our hot spot size estimates found with this method range from 26 $R_{\odot}$ to 58 $R_{\odot}$.

2.5.3 Hot Spot Size Estimate: Simple Model

We used a simple model for a third estimate of the size of the hot spot. For this model we assume the polarization of the disk is uniform across the disk edge. We first calculated a baseline qf_{DC}, the polarized flux due to the disk's self-illumination, by taking the error-weighted mean $\%Q_P$ multiplied by the normalized Fourier fit flux of the observations between phases 0.7 and 1.2 for each band (HWN). This assumes all the polarized flux at these phases is due to light originating within the disk rather than from the loser, a reasonable assumption given the results of HWN. We also define qf_{min}, the minimum polarized flux near secondary eclipse due to the primary star's eclipse and hot spot's transit of the disk, to be the error-weighted mean $\%Q_P$ multiplied by the normalized Fourier fit flux for observations between phases 0.4 and 0.55. If we subtract from qf_{DC} the amount of polarized flux blocked by the primary star and disrupted by the transit of the hot spot, the result should be qf_{min}, the polarized flux observed at secondary eclipse.

The amount of polarized flux lost due to the primary eclipsing the disk and the hot spot transiting the disk is given by

$$qf_{DC} - \frac{qf_{DC}}{A_D} A_{ecl} - \frac{qf_{DC}}{A_D} A_{HS} = qf_{min} \tag{2.5.5}$$

where A_{ecl} is the area of the disk eclipsed by the primary star (shaded region in Figure 2.8), A_D is the observed area of the edge of the disk, and $A_{HS} = H_D HS_{SM}$ is the area of the disk edge disrupted by the hot spot. The fraction $qf_{DC}/A_D = qf_{DC}/D_D H_D$ gives the polarized flux per unit area from the disk. The second term is the polarized flux eclipsed by the primary star and the third term is the polarized flux subtracted by the hot spot. We note that Equation 5 assumes an inclination angle of $i = 90^\circ$ and that each unit area of the disk contributes to the polarized flux equally. In reality, the relative contributions of each portion of a disk with an inclination angle of $i = 90^\circ$ are not equal due to limb darkening. Taking limb darkening into account would complicate our estimates; a hot spot near a limb darkened edge of the disk would need to be larger to account for the same amount polarized flux loss that would be lost by a hot spot closer to the center of the disk. Table 2.12 gives qf_{DC}, qf_{min}, and the resulting hot spot size estimate for the *BVRI* bands using Equation 5.

Assuming an inclination angle of $i = 86^\circ$ (Linnell et al. 1998, Linnell 2000) instead of 90° changes the equation we use to calculate HS_{SM}. In this case, the area of the disk that we see is larger than in the edge-on case; projection effects allow us to see a small portion of the back side of the disk. The visible portion of the interior of the disk is polarized differently than the disk edge; the polarized flux from the interior should cancel with some of the polarized flux from the disk edge.

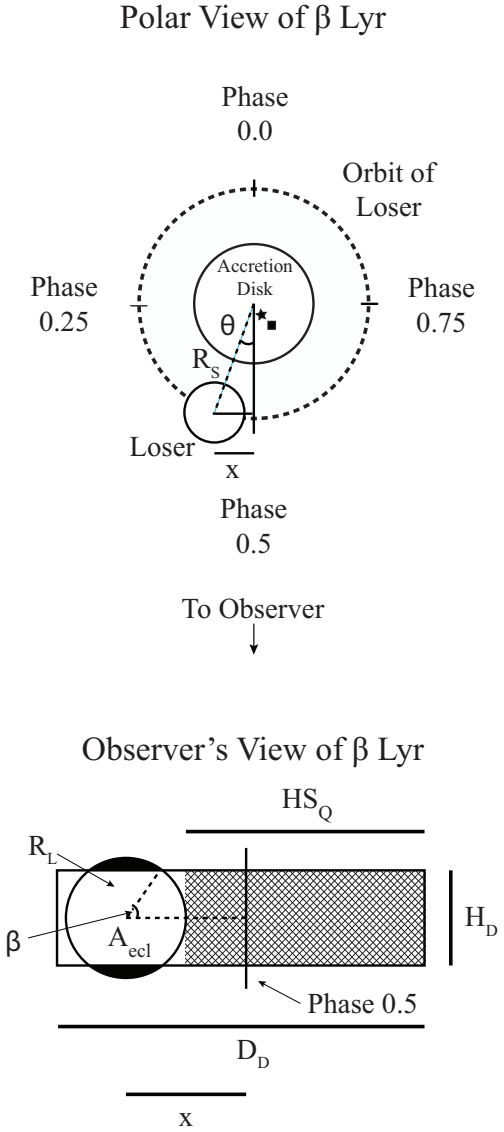

Figure 2.8 Sketch of the geometry we used for our hot spot size estimates (not to scale, see Section 2.4). We used parameters obtained by Linnell (2000) for the disk height, disk diameter, loser radius and separation between the two components. The hatched region in the Observer's View represents the hot spot size based on the $\%Q_p$ method (see Section 2.4.1). The blackened area of the circle in the Observer's View is the uneclipsed area of the loser at primary eclipse. The filled square inside the accretion disk in the Polar View indicates the location of the roots of the bipolar outflows as given by the Hα absorption core while the filled star represents the same thing for the Hα emission wings (Harmanec et al. 1996).

Also, the area eclipsed by the primary star is larger and the center of the star is no longer aligned with the plane that cuts the disk into equal bottom and top halves.

In order to calculate an estimate for $i = 86°$, we make the assumption that the area of the disk we see is rectangular. This makes our calculations easier since the projected height of the disk does not change across the disk edge, but has the effect of making our estimate smaller; if the edges of the projected disk have a height of H_D and the center of the projected disk has a larger height due to the projection, the total area of the disk is smaller than a rectangle whose height is the projected height (see Figure 2.9). This assumption allows us to use Equation 5 with a slight adjustment:

$$qf_{DC} - \frac{qf_{DC}}{D_D H_{PD}} A_{ecl} - \frac{qf_{DC}}{D_D H_{PD}} A_{HS} = qf_{min} \tag{2.5.6}$$

where H_{PD} is the projected disk height. A simple calculation reveals that $H_{PD} = 20R_{\odot}$. The area of the hot spot, $A_{HS} = H_D HS_{SM}$, remains unchanged because the hot spot is only on the front portion of the disk. Therefore, it does not take up the full projected disk height. We note that we do not have to account for the cancellation of polarized light due to the contribution from the interior of the disk. We are using our observations to estimate qf_{DC} and qf_{min}, and these numbers should therefore already incorporate this effect, if it is present. However, we still make the assumption that each portion of the disk contributes to the polarized flux equally. Besides the complication due to limb darkening mentioned previously, this enlarges our size estimate because more area is needed to cancel out the same amount of polarized flux. Table 2.12 gives the resulting hot spot size estimate for the *BVRI* bands when $i = 86°$ using Equation 6.

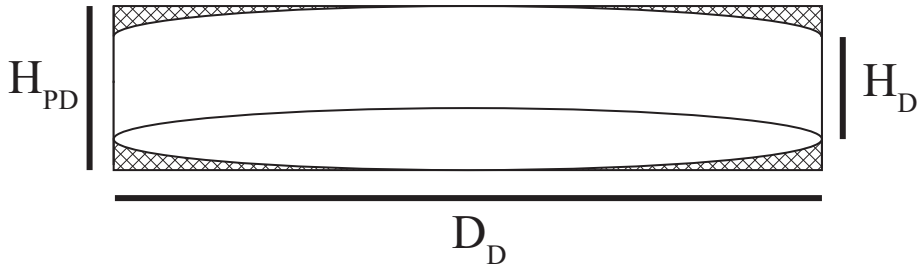

Figure 2.9 Sketch of the geometry we used for our simple model hot spot size estimate at an inclination angle of 86° (not to scale; see Section 2.4.3). The hatched regions represent the additional area of the disk in our estimate due to the assumption of a rectangularly shaped disk.

In our estimates, the size of the hot spot is smaller when the inclination angle is 86° compared to 90° for the following reason. The area of the disk is larger in the $i = 86^\circ$ method compared to the $i = 90^\circ$ method by a factor of approximately 1.3. This causes the amount of polarized flux per unit area to decrease by a factor of 0.8. However, the area eclipsed by the primary star increases by more than a factor of two. Therefore, the amount of polarized light lost due to the hot spot is smaller when $i = 86^\circ$ than when $i = 90^\circ$.

2.5.4 Comparison and Review of Hot Spot Size Estimates

Comparing all three methods, we find a wide range of sizes for the hot spot. The smallest size estimate is 2 $R_\odot$ (*I* band) while the largest is 58 $R_\odot$ (*V* band). The *R* and *I* band estimates are the most likely to change with additional data because their current phase coverage is not as good as the *B* and *V* bands. The *B* band estimates

have the closest agreement between the three methods; they range from 22 $R_\odot$ to 33 $R_\odot$, while the *V* band estimates have the largest range, 9 $R_\odot$ to 58 $R_\odot$. The overlap region for size ranges in all the bands is 22 $R_\odot$ to 33 $R_\odot$.

The large size of our estimates lends support to the possibility that we are actually detecting the portion of the mass stream which has not interacted with the disk and not a hot spot, similar to the findings of Bisikalo et al. (2000). The largest hot spot size estimate, 58 $R_\odot$, is similar in size to the diameter of the disk, 60 $R_\odot$, and the same as the binary separation, 58 $R_\odot$. However, this scenario would not likely produce the phenomena seen in Figures 2.1 through 2.4 because light scattering from the mass stream would tend to have a position angle similar to that of the disk; therefore, we prefer a large hot spot interpretation.

The 22 $R_\odot$ to 33 $R_\odot$ range is likely an upper limit for the size of the hot spot for several reasons. The position angle method (see Section 2.4.2) relies on using the randomization of position angles around secondary eclipse. We determined the length of time that the randomization in position angle lasts by using data from multiple orbits of the system. If the spot varies, either in size or location, on time scale similar to the orbital period, this variation would cause our estimate to be larger than the actual size of the hot spot. Also, we made the assumption that the hot spot contributes only unpolarized light to the observations. It is possible that the hot spot contributes light polarized at a different position angle than light polarized in the disk. This would cause a cancellation effect to occur; light polarized in the hot spot would cancel some of the light polarized in the disk. In this case, our estimate would again be larger than the area of the hot spot.

If the hot spot is indeed larger than 30 $R_\odot$, a portion of it may already be visible to the observer during primary eclipse. If this were the case, we would expect the

polarization maxima in the affected bands to shift from phase 0.0 to an earlier phase. This line of reasoning suggests that the primary eclipse effects seen in Figures 2.1 through 2.4, if real, may also be due to the hot spot (see Section 2.3.1). However, such a scenario does not explain why the *I* band polarization maximum occurs just after primary eclipse. The *R* band and three-term *V* band Fourier fits do not show an offset at primary eclipse, suggesting that the hot spot is not visible at this phase (see Section 2.3.1). We propose that the primary eclipse offsets are likely a result of the Fourier fits in some bands being less well determined around primary eclipse due to incomplete phase coverage.

The position angle scatter around primary eclipse in Figures 2.1 through 2.4 could also be interpreted as evidence that the hot spot is visible at this phase. As the system moves from primary eclipse to secondary eclipse, the amount of the hot spot visible to the observer should only increase if the time scale for changes in the hot spot is large compared to the orbital period. This suggests that if the scatter in the position angle of the 1997 August 25 observations (squares between phases 0.000 and 0.015 in Figures 2.1 through 2.4) is due to the hot spot, then a similar scatter should also exist in observations where the hot spot was fully visible during the same orbit. In particular, the 1997 August 26 (phase 0.079) and 1997 August 30 (phase 0.385) observations should show this effect. However, these two observations appear to have a position angle more similar to the system average than the 1997 August 25 observations. If that the mass transfer rate varies on time scales shorter than an orbital period, then the hot spot size may have changed over this five-day period to change the amount of position angle scatter. This scenario would explain the position angle scatter at primary eclipse for a single cycle, but it would not address the fact that no other orbits of the system were observed to have a posi-

tion angle scatter near primary eclipse. The combination of the arguments for and against the visibility of the hot spot at primary eclipse does not clearly determine whether its effects are discernible near phase 0.0. Multiple spectropolarimetric observations from the same orbit near primary eclipse will provide more insight into the cause of this phenomena and access its repeatability. In particular, the evolution of the color index of the polarized flux through primary eclipse compared to the evolution of the color index of the total light flux may shed new light on this situation.

Harmanec et al (1996) derived the location of the 'roots' of the bipolar outflows, where the bipolar outflows originate within the disk, using the Hα absorption core and the Hα emission wings seen in many epochs of spectra (see Figure 1 in Harmanec (2002) for an artist's view of the location of the outflows). The location of the roots (marked by a filled square in Figure 2.8 for the Hα absorption and by a filled star for Hα emission) is in the same quadrant of the disk in which we interpret the hot spot being located. However, the location of the roots is in the interior of the disk while we suggest the hot spot is a disruption in the structure of the disk edge. Certainly the bipolar outflows and the hot spot are related; both components are the result of the system's high mass transfer rate. How far into the interior of the disk the hot spot reaches is unknown. Additionally, the disk is made up of two components: a dense inner disk and an outer less dense disk (Skulskii 1992). What constitutes the 'disk edge' where the hot spot disruption occurs is unclear, although we have assumed it is the outermost edge of the disk (whose diameter is 60 $R_{\odot}$) in our size estimates. Because the scattering region for the Hα line is thought to be the bipolar outflows (HNF), future high precision Hα line polarization measurements may be able to link the two structures. If the hot spot location is consistent with

the roots of the outflows, we expect the Hα line polarization to show a secondary minimum offset, similar to those characterizing the broadband curves (Figures 2.1 through 2.4), while maintaining a position angle consistent with the outflows. Radial velocity curves of the Hα line's polarized flux may also provide valuable insight into the relationship between the hot spot and bipolar outflows.

2.6 Summary

We have presented a large new data set of polarimetric observations of β Lyr in the *BVRI* bands and the first Fourier fits to the polarimetric variations in these bands and the He I λ5876 emission line. We have interpreted the minimum in the *BVRI* projected polarization prior to secondary eclipse and the associated position angle rotations as the first direct evidence for a hot spot on the edge of the accretion disk in the β Lyr system. Using the phases of polarization minimum, the scatter of the position angle and a simple model, we have estimated the maximum size of the hot spot to be between 22 and 33 $R_\odot$ across the face of the disk. More extensive polarimetric modeling of β Lyr is needed in order to fully understand these results. Insights into the importance of the effects at primary eclipse and more accurate estimates of the hot spot size could be derived from such models.

We expect the hot spot may also be detectable in X-rays. Both ROSAT HRI (Berghofer & Schmitt 1994) and *Suzaku* (Ignace et al. 2008) have detected strong and variable hard X-ray emission from β Lyr. However, neither set of observations has provided information on the origin of the X-ray emission or observed the system at phases at which we see the hot spot effects. An X-ray light curve with more complete phase coverage will help locate the source of the X-ray emission.

The large uncertainties and scatter in Figure 2.6 make it difficult to pinpoint a location for the origin of the jets with confidence. Future, higher-precision line polarization measurements will provide much needed insights and determine their source.

Advancements in technology will soon allow for the combination of long-baseline optical interferometry with polarimetry (Elias et al. 2008). We expect such a technological development will provide new and exciting geometrical insights into the β Lyr system and others like it.

Chapter 3

A New View of the Colliding Winds in V444 Cygni

Jamie R. Lomax, Yael Nazé, Jennifer L. Hoffman, Michael De Becker, Hilding R. Neilson, Julian M. Pittard, Andy M. T. Pollock, and Christopher M. P. Russell 2013 (in prep.)

3.1 Abstract

Aims. To determine the extent of Coriolis distortion on the wind-wind collision region and the importance of radiative braking and inhibition in the V444 Cygni system.

Methods. We created the most complete the X-ray light curve of the V444 Cyg system with four new and six archived *XMM-Newton* observations and supporting *Swift* observations to date. In addition, we created polarized light curves of some

of the strongest emission lines with the University of Wisconsin's Half-Wave Spectropolarimeter.

Results. In our data we have detected evidence of the Coriolis distortion of the wind-wind collision in the X-ray regime, which manifests itself through asymmetric behavior in the X-ray light curves in the V444 Cyg system. Additionally, the polarimetric results show evidence of the hole the wind-wind collision region carves out of the Wolf-Rayet star's wind. While, the combination of these two data sets suggest that radiative forces play an important role in the system.

3.2 Introduction

V444 Cyg (also known as WR 139 and HD 193576) is one of the few known eclipsing Wolf-Rayet (hereafter WR) binary systems with colliding winds and a circular orbit (Eriş & Ekmekçi 2011; i = 78.3°$\pm$ 0.4°). Its distance has been disputed, although it is likely between 1.15 and 1.72 kpc (Kron & Gordon 1950, Forbes 1981, Nugis 1996). At this distance, it is the closest known example of an eclipsing WR binary. The primary star is a WN5 while the secondary is a main-sequence O6 star. The WN star has a mass of 12.4 $M_\odot$ and a mass loss rate of 4.6×10^{-6} $M_\odot$ yr^{-1}, while the O star is 28.4 $M_\odot$ and is losing mass at a rate of 5.8×10^{-7} $M_\odot$ yr^{-1} (Hirv et al. 2006). The terminal wind velocities are 2.5×10^3 km s^{-1} (WN star) and 1.7×10^3 km s^{-1} (O star; Stevens et al. 1992).

Evidence for colliding winds within the system is considerable and comes from several wavelength regimes. Studies using *IUE* spectra found evidence for colliding winds within V444 Cyg from variations in the terminal velocity and material density inferred from emission lines, and the absorption features within those emis-

sion lines (Koenigsberger & Auer 1985, Shore & Brown 1988). Additional evidence from *Einstein*, *ROSAT*, *ASCA*, and *XMM-Newton* suggests at least part of the observed X-ray emission is due to the wind collision region; the measured X-ray temperature is higher than expected for single WR and O stars, and the variability is consistent with a colliding wind scenario (Moffat et al. 1982, Pollock 1987, Corcoran et al. 1996, Maeda et al. 1999, Bhatt et al. 2010, Fauchez et al. 2011).

Today V444 Cyg is considered the canonical, close, short period, colliding wind binary system and has been extensively considered within the theoretical regime. It is considered to be the example system for both radiative inhibition, where the acceleration of a wind is reduced by the radiation from a companion star, and radiative braking, where a wind is slowed after reaching terminal velocity due to the companion's radiation (Stevens & Pollock 1994, Owocki & Gayley 1995). However, despite the system's brightness and ease to observe, V444 Cyg's X-ray phase coverage has been inadequate to make important and reliable constraints on these types of processes until now.

Bhatt et al. (2010) and Fauchez et al. (2011) have both analyzed the archived *XMM-Newton* observations previously. However, these observations only cover half of the system's orbit. Analysis by Fauchez et al. (2011) suggests some unexpected results concerning the wind collision region. These authors found that the hard X-ray emitting region may be positioned close to the WN star, suggesting strong radiative braking may be occurring within the system (Owocki & Gayley 1995). The observations we present here are the closest to complete version of the X-ray light curve of the system, allowing us to determine how the Coriolis force due to the short orbital period of V444 Cyg (4.2 days) distorts the geometric shape

and location of the shock cone, and further determine the importance of radiative braking and inhibition on the system.

Optical spectropolarimetric observations can place additional constraints on the geometry of circumstellar material within the system. Light scattering from free electrons in the ionized circumstellar material is responsible for the phase-dependent polarization observed in V444 Cyg (Robert et al. 1989, St.-Louis et al. 1993). Since electron scattering preserves geometric information about the scattering region, analyzing V444 Cyg's polarization behavior as a function of wavelength and orbital phase allows us to describe the scattering regions that produce the polarization in different spectral features. In the *UBVRI* bands, the observed phase-locked linear polarization variations are dominated by the O star occultation of photons originating from the WR star and scattering in a region of varying electron density (St.-Louis et al. 1993). V444 Cyg's polarization behavior near secondary eclipse deviates from the theoretical predictions of Brown et al. (1978), possibly due to the WR wind's distortion from spherical symmetry as a results of the binary's orbital motion (Robert et al. 1989, St.-Louis et al. 1993). St.-Louis et al. (1993) suggested that this deviation is due to the WR wind's distortion from spherical symmetry possibly as a result of the orbital motion of the V444 Cyg system (St.-Louis et al. 1993). Kurosawa et al. (2002) modeled the continuum polarization and found that they need the WR wind to reproduce the observations. In their work, the presence of the O wind and the wind-wind collision region do not affect the continuum polarization.

In this paper, we present the results of four new *XMM-Newton* observations, which we combine with six archival *XMM-Newton* observations to construct the most complete X-ray light curve of the system to date with supplemental observa-

tions from *Swift*. The locations of the optical and infrared primary and secondary eclipses (phases 0.0 and 0.5) are well covered. X-ray eclipses appear offset from these locations which provides important new information about the size and location of the hot gas within the system. We also conduct a spectral analysis of all ten *XMM-Newton* observations. We also present new polarization curves of the V444 Cyg system in several strong optical emission lines, using data obtained with the HPOL spectropolarimeter at Pine Bluff and Ritter Observatories. In Section 2 we describe the details of our observations. Section 3 presents and describes our observational results. We analyze our findings in Section 4 and summarize our conclusions in Section 5.

3.3 Observations

This study uses data from several distinct data sets. Our first set of data consists of ten X-ray observations taken during two different years with the *XMM-Newton* European Photon Imaging Cameras (EPIC); the second set is a 40 ksec observation of V444 Cyg taken over two weeks by *Swift*. The third consists of 14 observations taken with the University of Wisconsin's Half-Wave Spectropolarimeter (HPOL) at the 0.9m telescope at Pine Bluff Observatory (PBO); and the last includes 6 observations taken with HPOL on the 1.0m telescope at Ritter Observatory. We phased all observations using the ephemeris given by Eriş & Ekmekçi (2011):

$$T_{pri} = \text{HJD } 2441164.311 + 4.212454E$$

where E is the number of orbits of the system since the primary eclipse that occurred on HJD $2,441,164.311$.

3.3.1 XMM-Newton

Our ten *XMM-Newton* observations were taken using the EPIC instrument in full frame mode with the medium filter. The first six of those observations are from 2004 while the last four were taken in 2012. The lengths of the observations vary; see Table 3.1 for their observation ID numbers, revolution numbers, start times, durations, and phase ranges. In total they cover approximately 55% of the orbit.

All of these observations were reduced using the latest version of the *XMM-Newton* SAS software (version 12.0.1). Due to the faintness of the source, pile up is not a problem for any observation; however, background flares were excised from several observations (see Table 3.1). Additionally, data from both MOS CCDs for observation 0206240401 (revolution number 0819) were not usable due to a strong flare affecting both MOS1 and MOS2 exposures. For each *XMM-Newton* observation, we extracted spectra for all EPIC cameras in a circular region with a 30" radius around the source such that oversampling is limited to a factor of five and the minimum signal to noise per bin is three. The background was extracted from a nearby area devoid of sources that was 35" in radius. Additionally, we extracted count rates for these regions and computed their equivalent on-axis count rate while correcting for parts of the point spread function not in the extraction region (using SAS task `epiclccorr`) to create light curves for each observation for the soft (0.4-2.0 keV), hard (2.0-10.0 keV), and total (0.4-10.0 keV) bands.

Table 3.1: *XMM-Newton* Observation Information for V444 Cyg

Observation ID	**Revolution**	**Start Time (HJD)**	**Duration (S)**	**Phase Range**	**Flare?**
0206240201	0814	2453144.997	11672	0.112-0.171	No
0206240301	0818	2453152.986	11672	0.011-0.070	No
0206240401[a]	0819	2453154.986	10034	0.485-0.545	Yes
0206240501	0823	2453162.969	11672	0.385-0.444	No
0206240701	0827	2453170.943	11672	0.284-0.343	Yes
0206240801	0895	2453306.476	19667	0.450-0.510	Yes
0692810401	2272	2456053.363	45272	0.505-0.683	No
0692810601	2275	2456059.025	18672	0.870-0.929	Yes
0692810501	2283	2456075.221	13672	0.727-0.787	Yes
0692810301	2292	2456093.118	50067	0.941-0.119	No

[a] Data from MOS 1 and MOS 2 were lost for this observation due to a strong flare.

3.3.2 Swift

Swift observed V444 Cyg for 40 ksec over the course of two weeks in 2011 (see Table 3.2). Observations were not continuous so we only list the start time and the total exposure for each observation ID. The *Swift* data were processed with the online tool at the UK *Swift* Science Data Center[1], which produce a concatenated light curve with 100s bins, built for the soft (0.4-10 keV) and hard (2-10 keV) bands containing all *Swift* datasets. The small bins were then aggregated into 8 phase bins (0.00-0.5, 0.05-0.10, 0.45-0.50, 0.50-0.55, 0.55-0.60, 0.90-0.95, and 0.95-1.00). Our observations have no pile up and count rates are low (between 0.01 and 0.04 cts s^{-1}).

Table 3.2: *Swift* Observation Information for V444 Cyg

Observation ID	**Start Time (HJD)**	**Exposure (S)**
31983002	2455728.619	8970
31983003	2455730.627	8969
31983004	2455732.684	8048
31983005	2455734.778	6749
31983006	2455735.501	3277
31983007	2455736.978	4677
31983008	2455739.305	2646
31983009	2455743.586	2270

[1] http://www.swift.ac.uk/user_objects/

3.3.3 HPOL

Our HPOL data can be divided into two subgroups. Taken between 1989 October and 1994 December, the first 14 HPOL observations used a dual Reticon array detector with a wavelength range of 3200-7600 Å and a resolution of 15 Å (see Wolff et al. 1996 for further instrument information). During this period HPOL was at the Pine Bluff Observatory (hereafter HPOL@PBO). The last six observations were conducted between 2012 July and 2012 December with the refurbished HPOL at Ritter Observatory (hereafter HPOL@Ritter). These four observations used a CCD-based system with a wavelength range of 3200 Å-10500 Å, and a spectral resolution of 7.5 Å below 6000 Å and 10 Å above (Nordsieck & Harris 1996).

Table 3.3 lists the orbital phase along with the civil and heliocentric Julian date for the midpoint of each HPOL observation. All of the HPOL@PBO observations covered the full spectral range of the Reticon detector system. Only one of the HPOL@Ritter observations covered the full spectral range of the CCD detector system. The remaining HPOL@Ritter observations used the blue grating only (3200 Å-6000 Å). Each HPOL observation typically lasted between one and three hours (0.010 to 0.030 in phase). We reduced all of the HPOL observations using the REDUCE software package described by Wolff et al. (1996).

Table 3.3: HPOL Date and Phase Information for V444 Cyg

Date	Observatory	Detector	Midpoint HJD	Phase[a]
1989 Oct 03	PBO	Reticon	2447802.15	0.790
1990 Jul 24	PBO	Reticon	2448096.26	0.583
1990 Oct 23	PBO	Reticon	2448187.15	0.185
1990 Oct 24	PBO	Reticon	2448188.10	0.363
1991 Aug 21	PBO	Reticon	2448489.20	0.878
1991 Aug 31	PBO	Reticon	2448499.31	0.252
1991 Oct 10	PBO	Reticon	2448539.21	0.747
1991 Nov 17	PBO	Reticon	2448577.11	0.708
1994 Jun 15	PBO	Reticon	2449518.36	0.153
1994 Jul 03	PBO	Reticon	2449536.35	0.426
1994 Aug 16	PBO	Reticon	2449580.19	0.872
1994 Oct 06	PBO	Reticon	2449631.23	0.978
1994 Nov 12	PBO	Reticon	2449668.12	0.702
1994 Dec 01	PBO	Reticon	2449687.12	0.212
2012 Jul 13[b]	Ritter	CCD	2456121.83	0.767
2012 Jul 14[b]	Ritter	CCD	2456122.87	0.004
2012 Oct 19[b]	Ritter	CCD	2456219.62	0.971
2012 Oct 22	Ritter	CCD	2456222.58	0.684
2012 Oct 26[b]	Ritter	CCD	2456226.69	0.692
2012 Dec 14[b]	Ritter	CCD	2456275.55	0.265

[a] Phases were calculated using the ephemeris in Eriş & Ekmekçi (2011).

[b] Theses observations used only the blue grating. All other HPOL observations are full spectrum for their respective detectors.

3.4 Results

3.4.1 XMM-Newton Spectra

For each *XMM-Newton* observation, we extracted spectra for both MOS CCDs and the PN CCD. The data were fit with the XSPEC (v12.7.1) software package using the following two-component model (Arnaud 1996) with the same binning as the extracted spectra:

$$wabs \times (vphabs \times vapec + vphabs \times vapec)$$

where $wabs$ represents the interstellar medium absorption component with a hydrogen column density fixed to $n_H = 0.32 \times 10^{22}$ cm^{-2} (Oskinova 2005). We refer to the abundance table of Anders & Grevesse (1989) for the other components.

For each observation we fit the three EPIC spectra simultaneously, except for observation 0206240401 (revolution 0819) where we only have PN data due to a strong flaring event. We performed a careful step-by-step fitting procedure. First we allowed the temperatures, absorptions, and strengths (i.e. normalization factors within XSPEC) of the two components to vary freely, but we fixed the abundances to solar (Anders & Grevesse 1989). The temperatures of the two components were found to be constant with phase within their uncertainties; 0.6 keV for the first component and 2.0 keV for the second component. This is consistent with previous X-ray data of the system (Maeda et al. 1999). Therefore, we froze the temperatures of each observation at those values. Adopting constant temperatures with phase as we do here is consistent with a circular orbit and constant pre-shock wind speeds.

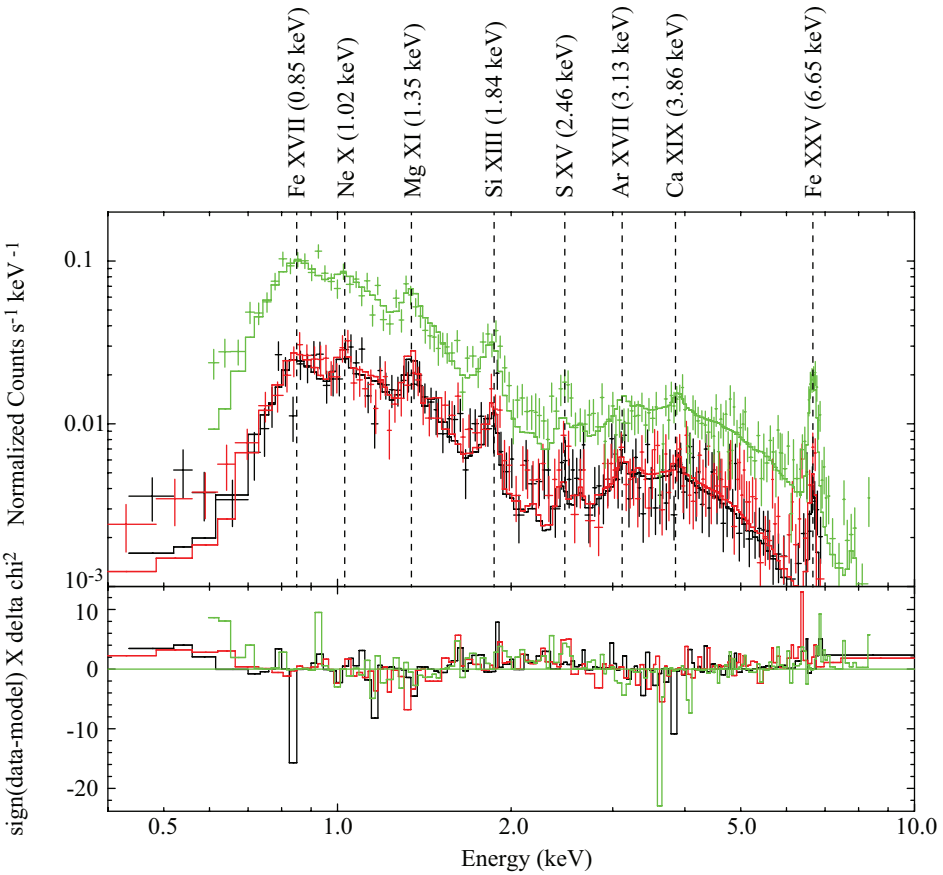

Figure 3.1 Sample *XMM-Newton* EPIC spectrum from observation revolution number 2292. Green (PN), red (MOS2), and black (MOS1) coloring represents the different detectors within the EPIC instrument. The solid lines represent the model fit to our data (see Section 3.3.1). We have also identified many of the strong emission lines indicated by the vertical dashed lines.

With fixed temperatures we then allowed abundances to vary, linking the abundances of each individual element across the model components. This produces only one abundance per element during the fitting. We allowed one abundance to vary at a time while holding all others constant in the following order: nitrogen (N), silicon (Si), sulfur (S), neon (Ne), magnesium (Mg), carbon (C), oxygen (O), and iron (Fe). We found the abundance of N to be about three times solar and constant with phase within uncertainties (abundances are in the XSPEC format: relative to hydrogen relative to solar). Therefore, we froze it at that value before moving on to the next element. Similarly, we found the Si, S, and Ne abundances for all of the spectra were solar within errors, so we froze them at 1.0. Magnesium was found to be slightly higher than solar and was frozen at 1.5. Both C and O were found to be comparable with a null value, so we set them to 0.0, while we found Fe to be just slightly lower than solar (0.8). These values are consistent with the Fauchez et al. (2011) results but are significantly different from the abundances found by Bhatt et al. (2010) because their complex model had many free parameters. Figure 3.1 shows a sample spectrum and model fit for one of our EPIC observations (revolution 2292) where we have also identified many of the strong emission lines and their approximate energies.

After we completed the abundance fitting, the only free parameters left were the normalization and additional absorption columns (see Table 3.4). As we are dealing with a circular orbit, the stellar separation does not change as a function of orbital phase. Therefore, the intrinsic emission from V444 Cyg should be constant with phase. However, we allow the normalization parameters, which reflect the emission measure and therefore the intrinsic X-ray flux from the system, to vary to probe the occurrence of orientation effects such as photoelectric absorption by wind

material and occultation. Therefore, we display these parameters (normalization and absorption columns) in Figure 3.2 graphically. The absorption of the 0.6 keV component stays relatively constant at a low value (see column 5 of Table 3.4). This suggests that the soft emission arises in the far regions of the stellar winds of the two stars, especially the WN wind. The slight increase in absorption between phases 0.22 and 0.6 is due to the O star wind's intrinsic emission becoming visible when the WN wind is no longer absorbing that emission in our line of sight (see Section 3.3.2). As expected, the absorption of the hotter component is strongest when the WN star and its wind are in front of the wind collision region (phase 0.0). In contrast, the absorption of the 2.0 keV component is weakest when the X-ray source is seen through the more tenuous O star wind. This occurs during a long interval between phases 0.25 and 0.75, suggesting a large opening angle for the bow shock (see Section 3.4). In general, the fluxes in Table 3.4 also roughly follow the light curves of the system (see Section 3.3.2).

In addition to the above spectral fitting, we divided observation 0692810401 (2272) into two separate spectra due the large change in count rate over the course of the observation (see Figures 3.3 and 3.4). The observation was divided at phase 0.624 (2272_1 before, 2272_2 after) and we performed spectral fitting to the two resulting spectra. We started our fitting process with the best fit from the total observation, keeping the same temperatures and abundances that were found to be constant on a global level (see previous paragraph). Therefore, the only free parameters were the normalization and absorption columns (see Table 3.4 and Figure 3.2) which agree with the total 2272 observation and the overall normalization and column density trends.

Table 3.4: Spectral Fit Information for V444 Cyg *XMM-Newton* Observations

Revolution	0.4-2.0 keV Flux	2.0-10.0 keV Flux	Norm 1st (10^{-3})	n_H 1st
0814	$1.12E{-13}$ $2.30E{-12}$	$1.00E{-12}$ $2.13E{-12}$	$0.37^{0.06}_{0.05}$	$0.32^{0.05}_{0.04}$
0818	$1.28E{-13}$ $1.81E{-12}$	$5.21E{-13}$ $1.58E{-12}$	$0.38^{0.05}_{0.05}$	$0.26^{0.03}_{0.03}$
0819	$3.36E{-13}$ $2.33E{-12}$	$6.27E{-13}$ $8.93E{-13}$	$1.68^{0.40}_{0.44}$	$0.51^{0.06}_{0.07}$
0823	$2.77E{-13}$ $2.79E{-12}$	$1.08E{-12}$ $1.64E{-12}$	$1.42^{0.25}_{0.23}$	$0.58^{0.05}_{0.05}$
0827	$2.08E{-13}$ $2.15E{-12}$	$9.10E{-13}$ $1.36E{-12}$	$1.00^{0.25}_{0.22}$	$0.58^{0.07}_{0.07}$
0895	$3.25E{-13}$ $2.40E{-12}$	$9.08E{-13}$ $1.27E{-12}$	$1.37^{0.19}_{0.18}$	$0.50^{0.03}_{0.03}$
2272	$1.51E{-13}$ $2.92E{-12}$	$1.18E{-12}$ $2.70E{-12}$	$1.62^{0.14}_{0.14}$	$0.45^{0.02}_{0.02}$
2272_1	$3.82E{-13}$ $1.94E{-12}$	$5.15E{-13}$ $6.24E{-13}$	$1.52^{0.18}_{0.17}$	$0.47^{0.02}_{0.02}$
2272_2	$4.83E{-13}$ $2.43E{-12}$	$7.20E{-13}$ $8.89E{-13}$	$1.79^{0.22}_{0.23}$	$0.44^{0.02}_{0.01}$
2275	$1.16E{-13}$ $1.64E{-12}$	$4.77E{-13}$ $1.41E{-12}$	$0.47^{0.04}_{0.04}$	$0.29^{0.02}_{0.02}$
2283	$2.98E{-13}$ $1.78E{-12}$	$5.83E{-13}$ $8.97E{-13}$	$1.07^{0.10}_{0.10}$	$0.36^{0.02}_{0.02}$
2292	$4.35E{-13}$ $2.15E{-12}$	$6.28E{-13}$ $7.65E{-13}$	$0.37^{0.02}_{0.02}$	$0.29^{0.01}_{0.01}$

Revolution	Norm 2nd (10^{-3})	n_H 2nd	Reduced χ^2	Degrees of Freedom
0814	$3.96^{0.28}_{0.27}$	$4.97^{0.39}_{0.36}$	1.1498	263
0818	$2.92^{0.47}_{0.42}$	$9.22^{1.47}_{1.30}$	1.0866	143
0819	$1.49^{0.37}_{0.30}$	$2.04^{0.95}_{0.77}$	0.9666	66

Continued on Next Page...

Table 3.4 – Continued

Revolution	**Norm 2nd (10^{-3})**	**n_H 2nd**	**Reduced (χ^2)**	**Degrees of Freedom**
0823	$2.92^{0.19}_{0.18}$	$2.34^{0.29}_{0.26}$	1.1529	299
0827	$2.43^{0.16}_{0.16}$	$2.23^{0.30}_{0.27}$	1.1224	277
0895	$2.22^{0.11}_{0.11}$	$1.82^{0.20}_{0.18}$	1.1455	363
2272	$1.25^{0.04}_{0.04}$	$1.01^{0.12}_{0.11}$	1.2884	444
2272_1	$9.99^{0.05}_{0.05}$	$0.96^{0.16}_{0.13}$	1.0173	333
2272_2	$1.46^{0.07}_{0.07}$	$1.09^{0.21}_{0.18}$	1.1711	388
2275	$5.00^{0.27}_{0.26}$	$5.70^{0.33}_{0.31}$	1.1992	379
2283	$1.56^{0.14}_{0.13}$	$2.54^{0.38}_{0.34}$	1.1940	278
2292	$2.60^{0.16}_{0.16}$	$8.86^{0.56}_{0.53}$	1.5771	418

These values were calculated by spectral fitting with the XSPEC software package (see Section 3.3.1). Fluxes, normalizations (columns 4 and 6), and column densities (columns 5 and 7) are in units of erg cm^{-2} s^{-1}, cm^{-5}, and 10^{22} cm^{-2} respectively. Absorbed (upper) and unabsorbed (lower) fluxes are given for each observation in the same soft and hard bands for which light curves were created (see Section 3.3.2). Normalizations and column densities have high and low error bars as indicated. In the case of observation 2272, we split the observation at phase 0.624 and performed spectral fitting of the resulting spectra as well as the whole observation (see Section 3.3.1). Observation 2272_1 represents the spectra derived from the data between

the start of observation 2272 and phase 0.624, while 2272_2 is from phase 0.624 to the end of the observation. See Section 3.3.1 for abundances used for all fits.

3.4.2 *XMM-Newton* and *Swift* Light Curves

To examine the behavior of the X-ray count rate with phase, we extracted light curves for each of the *XMM-Newton* observations for the soft (0.4-2.0 keV), hard (2.0-10.0 keV), and total (0.4-10.0 keV) bands. We display these light curves in Figures 3.3 and 3.4, with *Swift* observations in the same bands overplotted. We converted the *Swift* count rates into *XMM-Newton* equivalent count rates in all the energy bands using the WebPIMMS software package. These represent the most complete X-ray light curves of the V444 Cyg system to date. Additionally, they are the first light curves to resolve the system's eclipses (phase 0.0 and 0.55) which allows us to place important constraints on the size and location of the X-ray emitting region (see Section 3.4). *XMM-Newton* light curves for each observation were binned at 2 ks. Bins with a fractional exposure less than 0.5 were removed due to low signal. We also cleaned our light curves by filtering out points with backgrounds higher than 0.02 cts s^{-1} (PN) and 0.01 cts s^{-1} (MOS) for the soft band, 0.012 cts s^{-1} (PN) and 0.007 cts s^{-1} (MOS) for the hard band, and 0.025 cts s^{-1} (PN) and 0.015 cts s^{-1} (MOS) for the total band. This causes us to filter out all the PN data from observations 0692810601 (revolution 2275) and 0206240401 (revolution 0819) in the hard band. In addition, the MOS data from observation 0206240401 (revolution 0819) are not shown in any band because they were lost due to a strong flaring event. The total band light curve (Figures 3.3 and 3.4) is a combination of the hard and soft bands. We describe the behaviors of each individual band below.

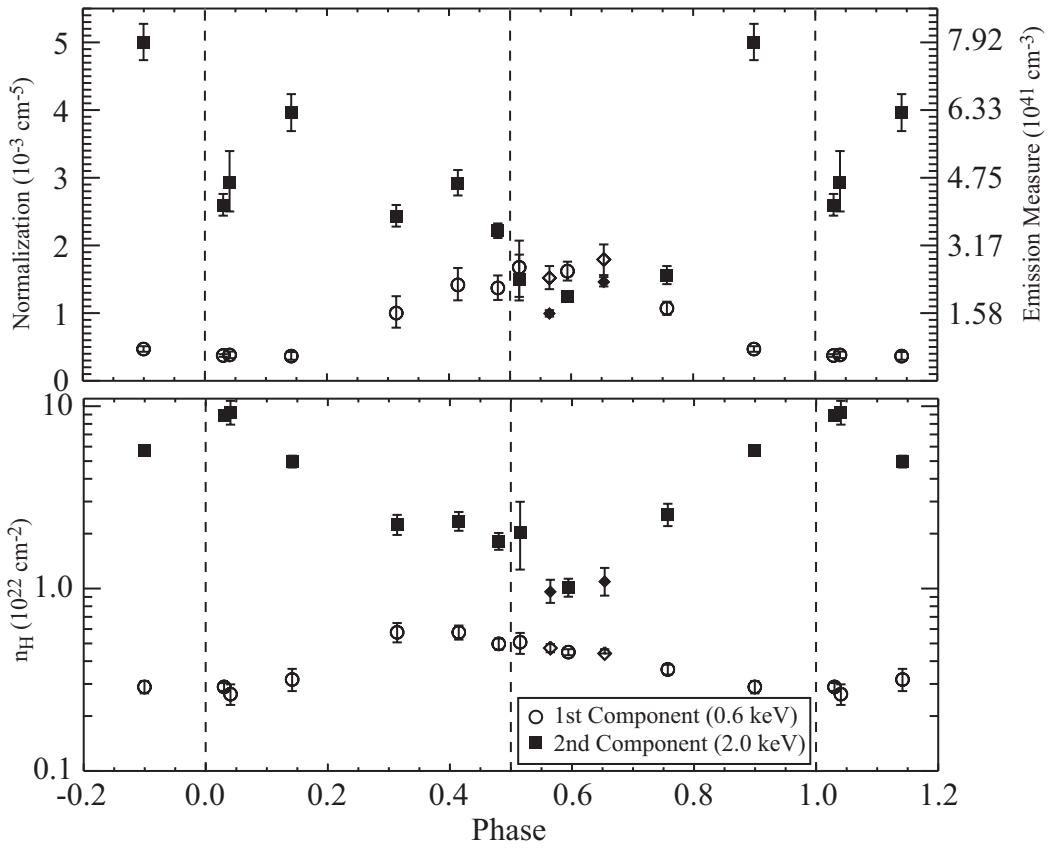

Figure 3.2 Normalization (top) and absorption column density (n_H; bottom; y axis is log scale) parameters found during our spectral fitting of the *XMM-Newton* observations as a function of phase. Circles (0.6 keV component) and squares (2.0 keV component) represent the two different model components. In the case of observation 2272, we split the observation at phase 0.624 as well as fitting the whole observation (see Section 3.3.1). Diamonds (open=0.6 keV, closed=2.0 keV) represent the two data sets derived from this split. Points are plotted in phase at the midpoint of each observation. Dotted vertical lines represent phases 0.0, 0.5, and 1.0. All data have been wrapped in phase so that more than one complete cycle is shown.

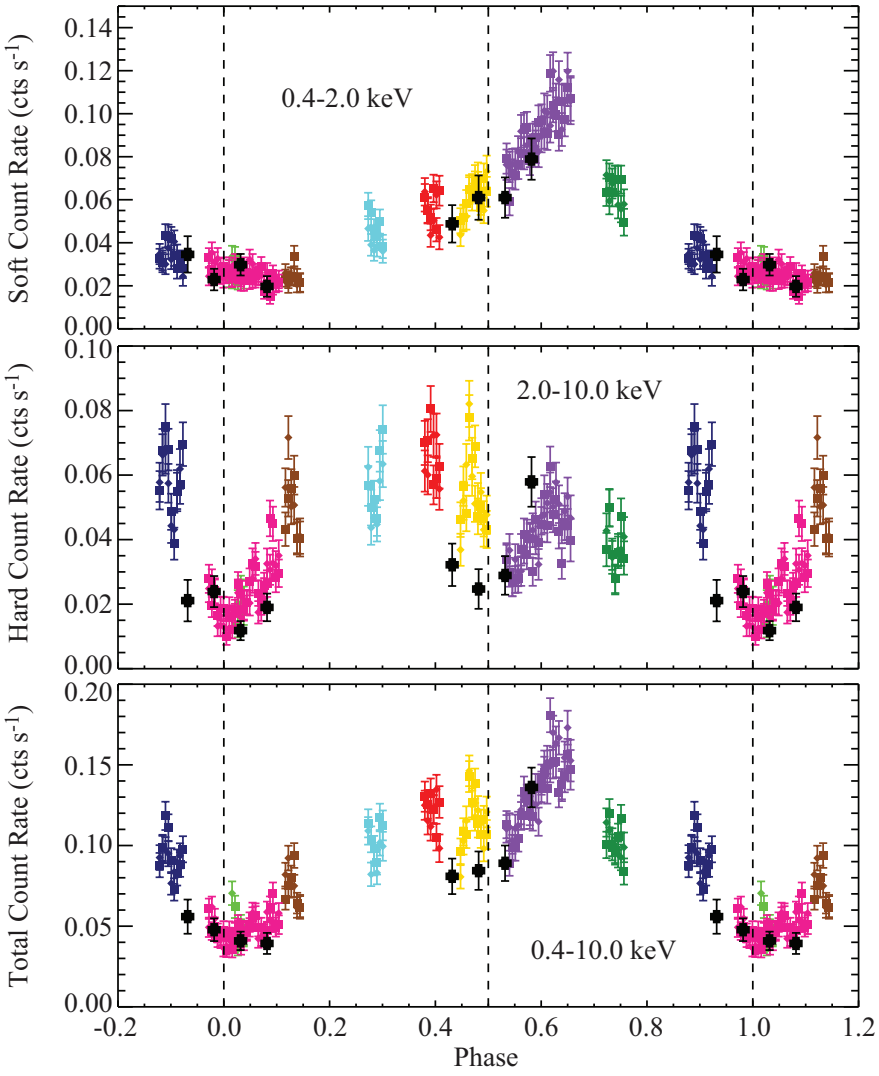

Figure 3.3 X-ray count rates from the *Swift* (black crosses), *XMM-Newton* MOS1 (diamonds), and MOS2 (squares) observations discussed in Section 3.3.2. Colors indicated data from different *XMM-Newton* observations: revolution number 0814=brown; 0818=green; 0819=blue; 0823=red; 0827=light blue; 0895=yellow; 2272=purple; 2275=dark blue; 2283=dark green; and 2292=pink. *Swift* data have been converted into an *XMM-Newton* count rate using the WebPIMMS software package. *From top:* Count rate in the soft (0.4-2.0 keV), hard (2.0-10.0 keV), and total (0.4-10.0 keV) bands versus phase. All data have been wrapped in phase so that more than one complete cycle is shown. The dotted vertical lines represent phases 0.0, 0.5, and 1.0.

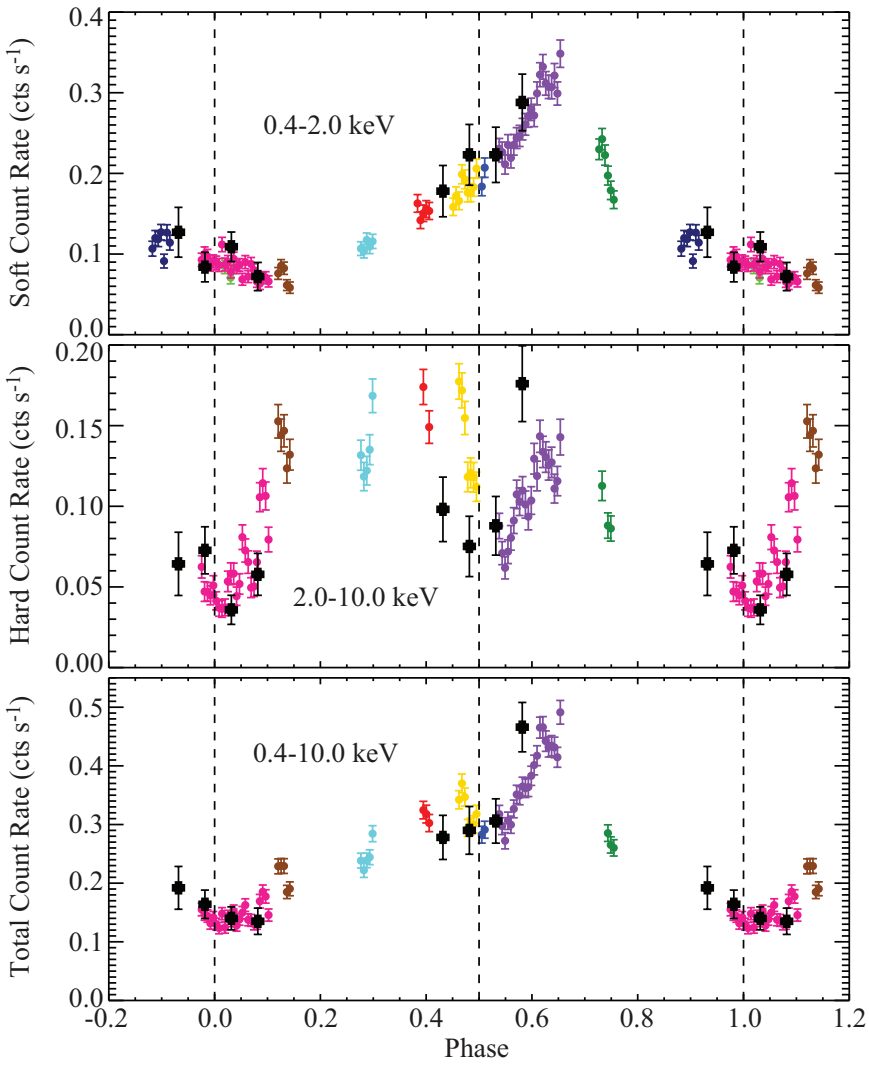

Figure 3.4 Same as Figure 3.3 but for the *XMM-Newton* PN camera.

The *Swift* observations are consistent with the *XMM-Newton* data in all bands. Additionally, where the *XMM-Newton* data overlap they show good agreement with each other despite the fact that data sets were taken during different orbits of the system, sometimes separated by several years (for example revolutions 2292 and 0818 overlap, and 0814 appears to follow the same trend 2292 does in the soft band). This is particularly evident near phases 0.0 and 0.5 where observations from different orbits and years would be indistinguishable from each other if it weren't for our color coding in Figures 3.3 and 3.4. At some level the behavior in the system is phase-locked despite there being obvious short term stochastic variations that presumably will not repeat.

In the soft band light curve, the minimum count rate occurs between phases 0.1 and 0.2 while the data show a maximum near phase 0.63 (see top panels of Figures 3.3 and 3.4). The PN data have a higher count rate than the MOS data due to the higher sensitivity of the PN camera to soft X-rays. The increase from minimum to maximum and the decrease from maximum to minimum appears to be smooth; however the count rate increases at a much slower rate as it approaches phase 0.63 than it decreases after the peak which may indicate that the leading shock edge is brighter than the trailing edge. However, the decline is only partially observed. It is obvious that important regions of the light curve have not yet been observed. The features seen in the soft light curve are related to the absorption behavior of the soft component in the spectral fits (see Figure 3.2 and Section 3.3.1). The phases which suffer the strongest absorption are indeed those when the WN star and its wind are in front; they are also the phases at which the soft count rate is the lowest. More of the soft X-rays can escape the winds of the system when the O star and its wind are in front in our line of sight due to that wind's lower absorption.

Indeed, the spectral fits show that the absorption of the hard component remains relatively constant between 0.25 and 0.75, despite the large variation in the soft count rate. This can be understood by considering the emission intrinsically linked to the O star wind. When the WN star is in front, the intrinsic X-ray emission from the O star wind is absorbed by the WN wind, but when the O star is in front its intrinsic emission becomes visible. This explains the increase in the normalization of the first component in the 0.25 to 0.75 phase interval (see Figure 3.2) from our spectral fits and the increase in the soft band count rate (see Figures 3.3 and 3.4). Moreover, the asymmetry of the soft light curve can only be due to distortion from Coriolis deflection of the shock cone. Different amounts of the O star wind are visible at different phases, but maximum visibility is not at phase 0.5 because of this distortion. We discuss the interplay between the emission and absorption behavior of the system more in Section 3.4.2.

The hard band light curves (middle panels of Figures 3.3 and 3.4) feature two eclipses, one centered on phase 0.0 (hereafter primary eclipse) and a second centered on phase 0.55 (hereafter secondary eclipse). Although, there also appears to be a fair amount of stochastic variability around theses phases as well which may be due to instabilities. The primary eclipse appears to be symmetric. However, the secondary eclipse is asymmetric; it starts at approximately phase 0.47 but ends at phase 0.63, and the system enters secondary eclipse more quickly than it recovers from it. Additionally, the system appears to enter the secondary eclipse at a higher count rate than that to which it recovers. Since the hard X-rays likely come from the higher temperature gas and the eclipses of the gas occur near the same phases as the optical eclipses, this behavior can be explained by the stars physically occulting the hot plasma in and around the stagnation point. However, this range is

bigger than the size of the O star in phase (approximately 0.1) so either the hard X-ray emitting region is large and never fully eclipsed (which is consistent with the count rate never dropping to zero) or the O-star wind is also responsible for a portion of the eclipse (in which case the count rate may never drop to zero because photons at these energies re not as readily absorbed within winds; see Marchenko et al. 1997 and Kurosawa et al. 2001). The asymmetry in the eclipse near phase 0.55 can then be explained by the position of the emitting region, which is not on the line of centers connecting the two stars due to Coriolis distortion (see Section 3.4.1 for the implications of the location of the hard X-ray emitting region). Combining this information with the shape of the eclipses (a deep and long primary eclipse) suggests that the primary WN star appears larger than what is suggested by visual and ultraviolet light curve analysis due its dense wind creating a 'wind eclipse' in addition to a stellar eclipse (Cherepashchuk et al. 1984, St.-Louis et al. 1993).

Observations 0692810601 (revolution number 2275; dark blue in Figures 3.3 and 3.4) and 0206240701 (0827; light blue) appear to have a variable count rate that is not part of the global light curve shape. We caution that the validity of some of these features remains unknown because the uncertainties of these measurements are similar in size to the change in count rate over the course of the observations. Additionally, observation 0206240801 (revolution 0895) has what looks like an emission spike that could cause us to underestimate the length of the secondary eclipse. We did remove a flare from this observation and therefore, it is possible that the flare may not have been completely excised causing the observed spike.

3.4.3 Optical Polarimetry

Continuum polarization light curves show phase-dependent variations that cannot be completely described by the standard, sinusoidal, 'BME'-type behavior expected from binary stars (Brown et al. 1978, St.-Louis et al. 1993). Differences from that behavior near secondary eclipse indicate a deviation of the WN star's wind from spherical symmetry due to the orbital motion of the system. However, the polarization of the emission lines has yet to be studied. Therefore, we took advantage of the spectropolarimetric nature of the HPOL data to investigate the polarization behavior of the strongest emission lines in the optical regime. Figure 3.5 shows a sample polarization spectrum produced by taking the error-weighted mean of the four HPOL@PBO observations between phases 0.6 and 0.75 (see Table 3.3), binning the resulting stacked spectrum to 25Å , and identifying many of the major emission lines. Even though we only show one averaged spectrum here, there is phase-dependent variability in both the continuum polarization and emission lines (Robert et al. 1989, St.-Louis et al. 1993).

In order to calculate the polarization in the HeII λ4686, Hα, and NIV λ7125 emission lines, we used the flux equivalent width (EW) method described by Hoffman et al. (1998). Line polarization values calculated with this method are intrinsic to the system and include no interstellar polarization (ISP) or instrumental effects. This is because when we subtract the continuum polarization from the polarization in the line region, ISP and instrumental effects, which contribute to both the line and continuum, are automatically removed. The choice of regions from which to estimate the continuum is important because the ISP does have some wavelength dependence, and because the inclusion of a polarized line in a continuum region will skew the polarization calculated for the line of interest. Therefore, we chose

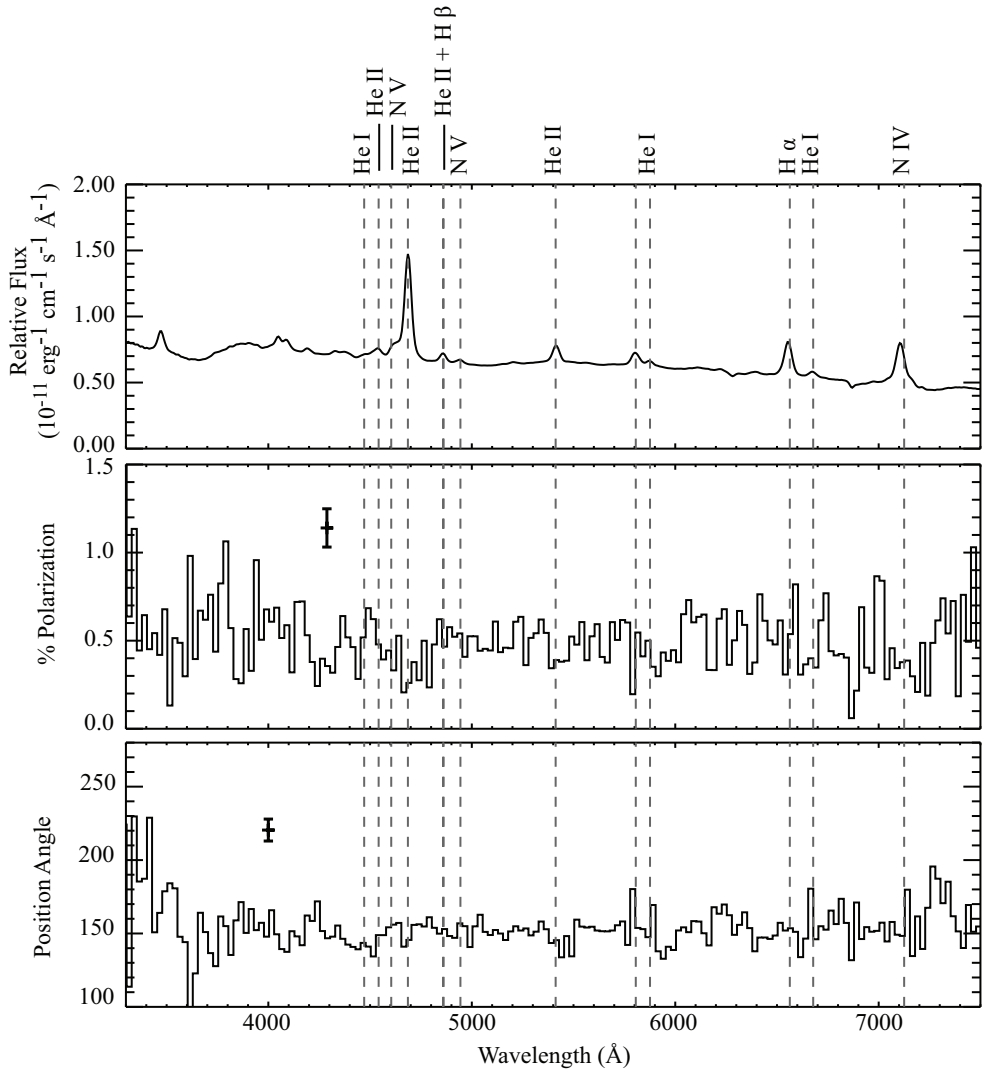

Figure 3.5 Error-weighted mean polarization spectrum for HPOL@PBO observations between phases 0.6 and 0.75. *From top:* relative flux, percent polarization, and position angle (degrees) versus wavelength. Grey dashed lines indicate identified emission lines. The polarization and position angle data have been binned to 25Å . Error bars shown are the average polarization and position angle errors for the spectrum.

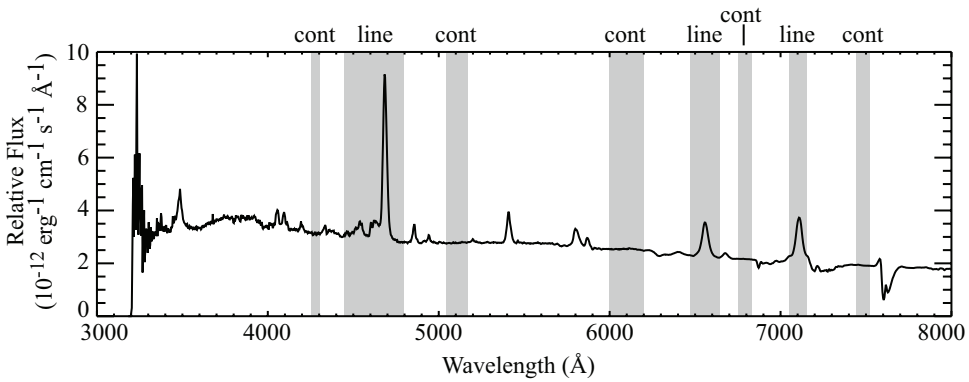

Figure 3.6 Relative total flux spectrum from the observation conducted with HPOL@Ritter on 2012 Oct 22. Grey boxes mark the line and continuum regions used to calculate the line polarization using the flux EW method (see Section 3.3.3) for every observation. Each calculation uses the first continuum region on the red and blue side of the line region.

continuum regions that appear to have no emission or absorption features in our total or polarized spectra. Figure 3.6 shows the continuum and line regions we used in our calculations.

In the case of the HeII λ4686 line we chose a line region that includes not only the HeII λ4686 line but also the NV λ4604 4620 doublet, and the HeII λ4542 and HeI λ4471 lines since they are blended with each other in our spectra. This makes it more difficult to determine which line is responsible for any phase-dependent polarization behavior; however, it allows us to ensure we include all spectral regions which may be contributing to any variations. Similarly, the NIV λ7125 line (Figure 3.8) has many absorption and emission lines around it, but we were able to define a line region that includes the line core without other stray lines and appropriate continuum regions. In the case of the Hα line (Figure 3.9) we were able to define line and continuum regions more easily than the other lines.

Photospheric absorption in the O star is an important source of line profile variations observed in total light (Marchenko et al. 1997, Flores et al. 2001). If we do not correct for this unpolarized absorption we remove too much continuum polarization from our observations. Marchenko et al. (1997) removed an absorption component from their HeII λ4686 profile data by approximating the O-star absorption as a Gaussian line profile with a full width at half maximum (FWHM) of 6.0 Å and an EW of 1.0 Å. The same authors estimate an absorption profile for the HeI λ4471 line as a Gaussian with a FWHM of 6.0Å and an EW of 0.25 Å. While we do not know the EW of the NV doublet that is also blended with the HeII λ4686 line, we corrected for an underlying unpolarized absorption component using a total EW of 2 Å . This corrects for the absorption due to the He lines (1.25 Å total) while estimating a total absorption equivalent width of 0.75 Å for the N doublet. We found that the corrected line polarization values were not significantly different from the uncorrected values. Similarly, we find that for the Hα line, corrections on the order of half the total EW need to be made before the corrected values differ from the uncorrected by more than their uncertainties. This is significantly larger than the absorption EWs estimated for O stars (Kurucz et al. 1974; 2Å). Therefore, in the rest of this paper we present only the uncorrected data for all lines.

Figures 3.7-3.9 show the phase-dependent polarization behavior for the HeII λ4686, NIV λ7125, and Hα lines (see Table 3.5). While it is possible for emission lines to be unpolarized in Wolf-Rayet systems (Harries et al. 1998), we do not believe this is the case for V444 Cyg. If the lines are intrinsically unpolarized, then they should show the same variation with phase as the continuum polarization (see for example St-Louis et al. 1993). However, the phase-dependent behavior of these three lines is not consistent with the broadband polarimetric behavior found by St.-

Louis et al. (1993) and Robert et al. (1989). This indicates that the extra emission in these lines is polarized differently than the light in the surrounding continuum. This inconsistency also rules out the possibility that the lines are polarized the same amount as the continuum. Because the stars are hot, we expect that electron scattering is the dominant polarizing mechanism in the system for both line and continuum light. Thus, the differing phase variations imply that light in the emission line form, scatter, and/or become eclipsed differently than does light in the continuum. Analyzing these variations can help us further constrain the geometry of the emission and scattering regions in V444 Cyg.

Table 3.5: HPOL Line Polarization Stokes Parameters

Phase	**% Q**	**% U**	**% Error**
		Hα	
0.790	-1.5110	-2.4579	0.9408
0.583	-0.0306	0.1236	0.9911
0.185	-1.4468	2.1103	0.8538
0.363	-0.5154	-0.2944	0.7267
0.878	-1.0984	0.7828	1.0322
0.252	-0.0926	0.2813	0.9119
0.747	-1.6390	-0.2771	0.6717
0.708	0.2388	-1.6601	1.0027
0.153	4.9108	0.9717	2.5127
0.426	-0.6828	-0.6338	1.5643
0.872	1.0321	0.4674	1.2103
0.978	-0.8630	1.2595	1.3337
0.702	1.3809	-1.5241	1.5728
0.212	-0.7050	0.2555	1.1458
0.766	...	...	...
0.004	...	...	...

Continued on Next Page...

Table 3.5 – Continued

Phase	**% Q**	**% U**	**% Error**
0.971	...	...	...
0.683	-0.1010	-0.4941	0.1913
0.692	...	...	...
0.265	...	...	...
		HeII λ4686	
0.790	0.0654	-0.1774	0.2992
0.583	-1.0061	-1.4650	0.3212
0.185	0.0068	0.4654	0.3375
0.363	0.3231	-0.7084	0.2973
0.878	-0.6105	-0.4702	0.3845
0.252	1.4296	-0.3627	0.4441
0.747	0.0549	-0.4787	0.3698
0.708	-0.1982	-0.2855	0.4866
0.153	0.9262	0.0591	0.7414
0.426	1.1650	-1.5495	0.4584
0.872	-0.2664	0.9080	0.5495
0.978	0.5983	-0.0933	0.5676
0.702	0.3399	0.1109	0.7363
0.212	0.7282	-1.0072	0.5716
0.766	2.9451	-1.6647	0.5953
0.004	1.4648	0.2450	0.8573
0.971	-1.0586	-1.3001	0.7125
0.683	0.1301	0.1954	0.3585
0.692	0.7285	-0.8648	0.6236
0.265	0.1316	-0.1312	0.3755
		NIV λ7125	
0.790	-0.6922	-0.6771	0.7119
0.583	-0.9406	0.0248	0.5935
0.185	0.2097	1.1375	0.5768
0.363	-0.7041	-0.8975	0.7494
0.878	0.9202	-0.0931	0.6354
0.252	-0.4877	0.3206	0.7898

Continued on Next Page...

Table 3.5 – Continued

Phase	**% Q**	**% U**	**% Error**
0.747	-0.0859	0.4593	0.5554
0.708	-0.6661	-0.0959	0.7179
0.153	3.1580	2.5385	1.5831
0.426	-1.2326	-1.3260	1.2366
0.872	1.9333	0.5301	0.9724
0.978	-0.3639	1.1728	0.9390
0.702	0.2433	-1.6902	1.4111
0.212	-1.7630	1.8021	0.9190
0.766	...	...	...
0.004	...	...	...
0.971	...	...	...
0.683	0.2929	-0.1404	0.0887
0.692	...	...	...
0.265	...	...	...

Since the HeII λ4686 emission line shows little phase dependence in the Stokes Q parameter, we calculated the error-weighted position angle of this line ($168^\circ \pm 0.2^\circ$) and rotated the data to this angle. We do not interpret this angle as an intrinsic axis for the system; there is a high amount of scatter in the polarization position angle of the HeII λ4686 line. Rather, a rotation by this angle allows us to place all of the polarization variation in the resulting projected Stokes U parameter (% U_p), since the projected Stokes Q averages to zero. In the rest of this section, we discuss the polarization behavior of the HeII λ4686 line in terms of $\%U_p$ only. We rotated the NIV λ7125 line to $145.4^\circ \pm 0.2^\circ$ for the same reasons, with the same caveat that this angle is not necessarily intrinsic to the system. In the case of the Hα line, both

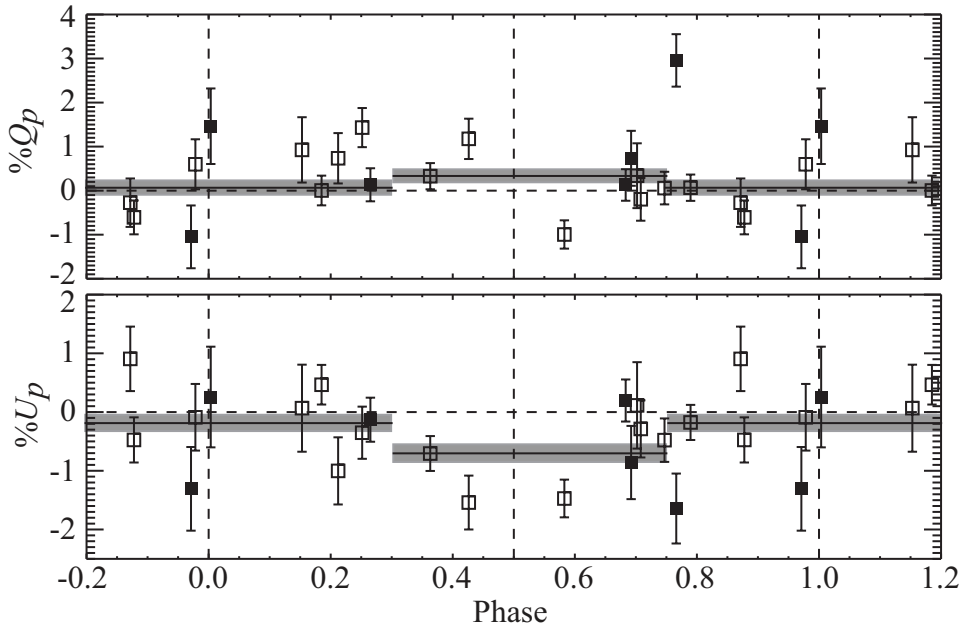

Figure 3.7 Data points represent the HeII λ4686 emission line polarization from HPOL@PBO (open squares) and HPOL@Ritter (filled squares). From top: projected % Q_p Stokes parameter and projected % U_p Stokes parameter versus phase. The solid horizontal lines surrounded by grey rectangles mark the error-weighted mean % U_p and % Q_p with uncertainties for the phase regions for which they are over plotted. Dotted vertical lines represent phases 0.0, 0.5, and 1.0. Dotted horizontal lines mark zero in % Q_p and % U_p.

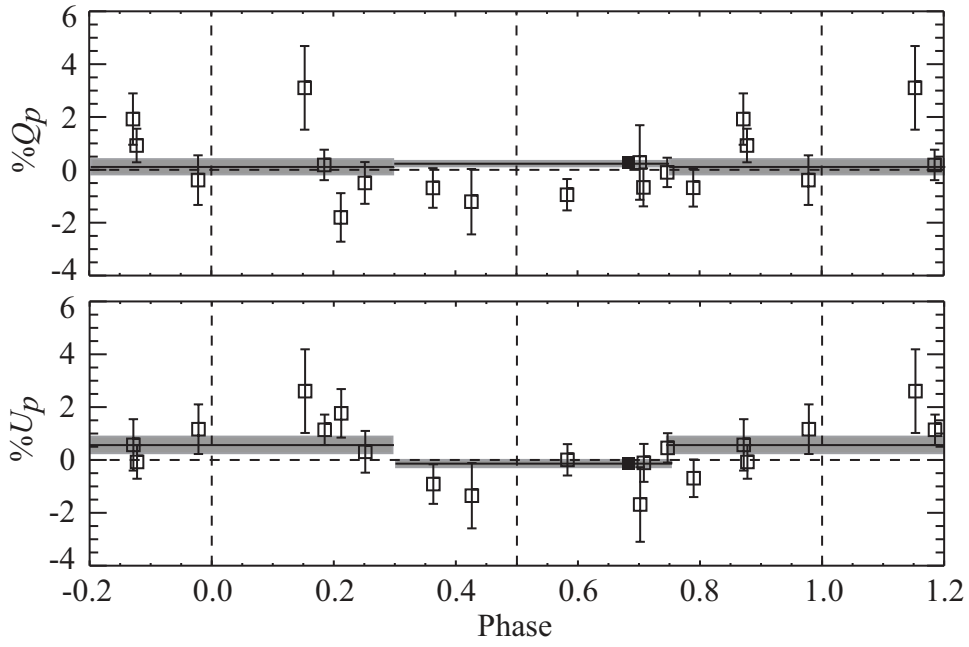

Figure 3.8 Same as Figure 3.7, but for the NIV λ7125 line. Stokes parameters are rotated to $145.4°$.

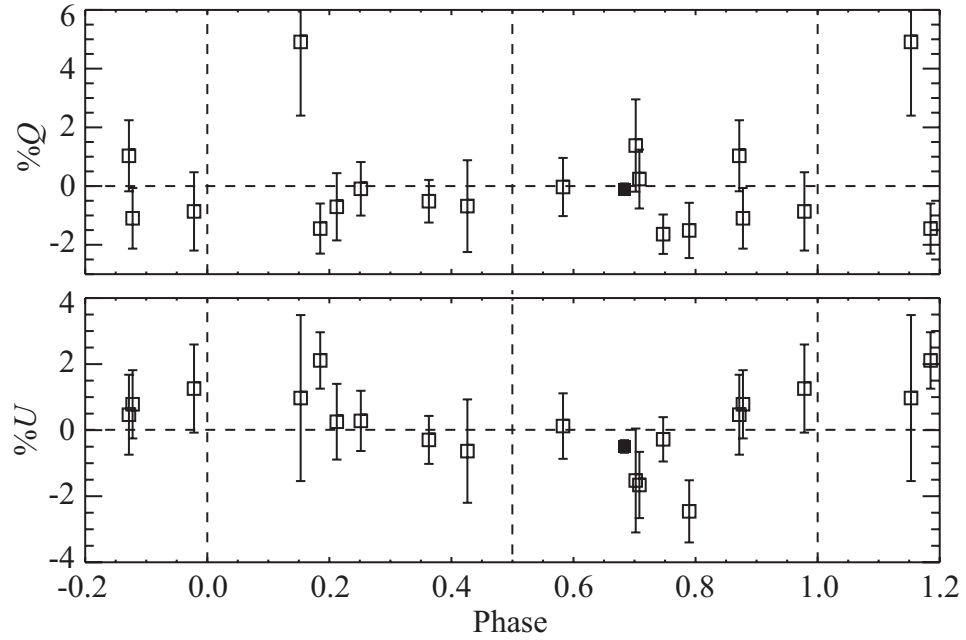

Figure 3.9 Same as Figure 3.7, but for the Hα line. Stokes parameters are unrotated.

Stokes parameters remain zero within uncertainties, but deviate from that behavior for a limited number of observations. We therefore do not rotate these data.

After rotation, the HeII λ4686 % Q_p (Figure 3.7) remains positive for the first half of the light curve, but scatters around zero more evenly during the second half. The % U_p shows variations on the same level (on the order of $\pm 2\%$) however, it has a phase dependence. Points between phases 0.6 and 1.0 have a larger scatter than the rest of the light curve, while observations near secondary eclipse have a lower % U_p than the rest of the light curve. The HeII λ4686 % U_p has a phase-locked polarization behavior associated with the phases that have a low 2.0 keV component absorption behavior from the X-ray spectral fitting (see Figure 3.2). To quantify this, we calculated the error-weighted mean % U_p for the phase regions 0.30 to 0.75, and 0.75 to 1.30. The same region in phase that has a low 2 keV absorption has a lower average % U_p (-0.703 ± 0.142) than the rest of the light curve (-0.193 ± 0.133), a discrepancy of nearly 2-sigma. The % Q_p averages for those same phase intervals overlap within uncertainties (0.056 ± 0.142 for phases 0.30-0.75; 0.320 ± 0.133 for phases 0.75 to 1.30).

The NIV λ7125 shows a similar behavior to the HeII λ4686 line (see Figure 3.8); the % U_p values for this line are predominately negative for a similar range in phases as the low 2 keV component absorption feature (Figure 3.2) and is positive or zero for other phases. However, the % Q_p values are negative in the 0.3 to 0.6 phase range, but scatter equally about zero at other phases. A similar analysis shows the error-weighted mean % U_p for observations between 0.3 and 0.75 in phase is significantly lower (-0.139 ± 0.085), than the rest of the cycle (0.579 ± 0.279), while the average % Q_p for these two regions overlap (0.228 ± 0.085 for phases

0.30-0.75; 0.110 ± 0.279 for phases 0.75 to 1.30). Again, this is similar to the HeII λ4686 result.

To directly compare the behavior of the two lines, we smoothed our polarization data by calculating the error-weighted mean unrotated $\%Q$ and $\%U$ for bins of width 0.1 in phase (Figure 3.10) and found that these two lines show similar trends. The $\%U$ values are more positive near phase 0.0 and first quadrature (phase 0.25) than around phase 0.5 while after secondary eclipse they gradually trend toward more positive values. In contrast, $\%Q$ remains relatively flat during the first half of the orbit, while the variations in the second half are of a more stochastic nature.

Within the V444 Cyg system, the NIV should be located within the wind of the WN star, and the HeII is largely in a shell of material around the WN star (see Figure 8 in Marchenko et al. 1997). If the shells of HeII λ4686 and NIV λ7125 around the WN star are the scattering region for these lines and are spherically symmetric no net polarization would be measured. However, in both cases we measure a phase dependent polarization so these shells must be aspherical in some way. The WN wind is much more dense than the O-star wind (Stevens et al. 1992, Hirv et al. 2006) and a cavity in the WN wind could effectively create an asymmetry.

The polarization behavior of a hole in the ejecta of Type Ia supernovae have previously been considered by Kasen et al. (2004). While the density profiles within the model ejecta and hole are different than the winds and shock within V444 Cyg, there are several important similarities between them. First the ejecta hole produces a geometry resembling the shock structure within V444 Cyg. Additionally, the density of material within the hole is less than the other ejecta, which is analogous to the O star wind within the boundaries of the shock being less dense than the WN wind. Kasen et al. (2004) oriented their models such that all the polarization vari-

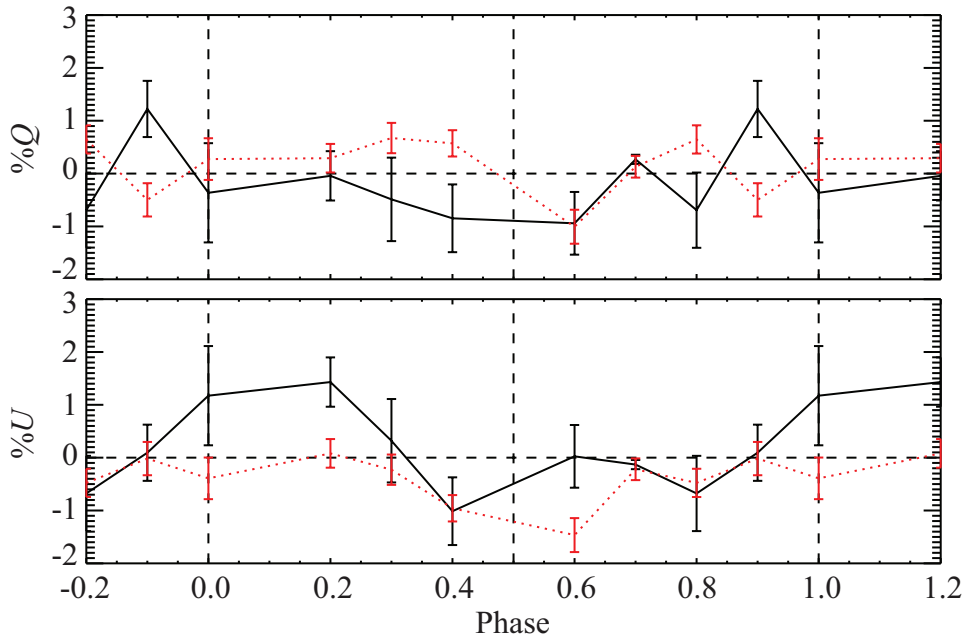

Figure 3.10 Unrotated Stokes parameters for the HeII λ4686 line (red dotted) and NIV λ7125 (black solid) data, binned to 0.1 in phase.

ations occurred in one Stokes parameter. They found that for viewing angles near the axis of the hole, the polarization is negative, but it becomes more positive as the viewing angle moves away from the hole. Because we rotated our line data (Figures 3.7 and 3.8) such that most of the polarization variation occurred in % U, we can draw an analogy between these variations and those predicted by the ejecta-hole model. In this analogy, the change in polarization behavior of our HeII λ4686 and NIV λ7125 lines is due to the shock cone creating a 'hole' in their shells of material around the WN star. As our viewing angle changes with phase, the changing geometry of the incomplete shells causes the variations in polarization we observe. In this picture, the 'hole' should correspond to phases near secondary eclipse and is consistent with the shock cone seen in the X-ray data creating a cavity in the WN-star's wind similar to a hole structure. The angle by which we rotated each

line's data thus corresponds to the geometrical offset between the orientation of the shells in V444 Cyg and the orientation of Kasen et al. (2004)'s model. It is similar, but not the same for the two lines. In addition, the trends in polarization with phase differ between lines (Figure 3.10). If this simple picture is a good approximation of the winds in V444 Cyg, these discrepancies may simply indicate that the shock is a more complex structure than a simple cone. This is not the first time a cavity in the WN wind has been considered with respect to the phase dependent polarization behavior of the system. However, when Kurosawa et al. (2002) modeled the continuum polarization with out needing effects from the O-star wind or the wind-wind collision region. From their models, the WN wind is the only significant contributor to the continuum polarization.

Unsurprisingly, our data do not exactly reproduce the trends in polarization with viewing angle predicted by Kasen et al. (2004). One important difference is the size of the opening angle of the shock/ejecta hole. Our shock likely has a very large opening angle (see Sections 3.3.1 and 3.4.2), which means our viewing angle remains closer to the edge of the hole than in Kasen's models. In addition, although we rotated our data in an attempt to confine the phase-locked polarization to one Stokes parameter, both still display relatively large changes in % Q_p (Figures 3.7 and 3.8). In the context of this model, this might indicate that at phases when we do not see the shock and the hole, the WN wind appears elongated rather than spherically shaped.

In contrast to the HeII λ4686 and NIV λ7125 lines, the Hα emission likely comes from cooler regions around the system. Figure 3.9 shows that much of this emission is unpolarized; both Stokes parameters are zero within uncertainties in the majority of our observations. This suggests that either the scattering region for

the Hα line is spherically symmetric or that the Hα line emission undergoes little scattering in the system. The deviations from zero polarization do not appear to have a phase-dependent behavior, which suggests that clumping of material within the cooler regions of the system may be responsible for the variable polarization which at times is nonzero (Li et al. 2009). Such clumps are likely transient and unconnected to the orbital period of the system; thus, any polarization produced by scattering in this clumpy wind should be stochastic as suggested in Figure 3.5 (Li et al. 2009).

3.5 Discussion

The evidence for colliding winds within this system is undeniable (see Section 3.1) and suggests that the behavior we see in both the X-rays and polarimetry is due to the distortion of the stellar winds due to the orbital motion of the stars, as well as direct eclipse effects. Our X-ray light curves and spectra have several implications for the geometry of the system. Below we discuss simple models of these data that allow us to draw some basic conclusions about what their behavior means for the V444 Cyg system. We adopt the following parameters in our models: a separation of $a = 35.97\ R_{\odot}$, stellar radii of $R_{O6} = 6.85\ R_{\odot}$ and $R_{WN} = 2.9\ R_{\odot}$, stellar masses of $M_{O6} = 28.4\ M_{\odot}$ and $M_{WN} = 12.4\ M_{\odot}$, stellar mass loss rates of $\dot{M}_{O6} = 5.8 \times 10^{-7}\ M_{\odot}\, yr^{-1}$ and $\dot{M}_{WN} = 6.76 \times 10^{-6}\ M_{\odot}\, yr^{-1}$, and terminal velocities of $v_{O6}^{\infty} = 1700\ km\, s^{-1}$ and $v_{WN}^{\infty} = 2500\ km\, s^{-1}$ (Stevens et al. 1992, Corcoran et al. 1996, Hirv et al. 2006, Eriş & Ekmekçi 2011). We do not calculate formal uncertainties on our models' outputs because of their simplicity; it is clear a

more sophisticated treatment of the system is needed, which we plan to address in a future paper.

All our models assume a 90° inclination angle while the V444 Cyg system's actual inclination angle is $i = 78.3^\circ \pm 0.4^\circ$ (Eriş & Ekmekçi 2011). As such, our models are two dimensional which greatly simplifies the calculations. However, we note that the compactness of the system is high, so that this is likely to be a good approximation in most respects.

3.5.1 Modeling the Hard X-ray Light Curve

In Section 3.3.2 we suggest that the variability of the hard X-ray light curve (see Figures 3.3 and 3.4) is due to the stars physically occulting hot plasma in and around the stagnation point. We used a simple model in order to investigate this possibility. The goal of this analysis is to determine the location of the material responsible for the hard X-ray emission relative to the two stars.

Our simple model consists of a hard X-ray emitting region which we moved to different locations within the system in order to match the eclipse locations in phase, the slopes of the ingress and egress of eclipses, and the eclipse duration. The whole system, both stars and the hard X-ray emitting region, rotates about the system's center of mass, which we calculated using the separation and stellar masses quoted above. We placed initial constraints on the location of the hot plasma by only considering the areas within the system that are eclipsed at both phase 0.0 and phase 0.55. These areas are shown as a hatched region in Figure 3.11. We divided this region into slices that were one solar radius in width and the full height of the region. In order to produce a light curve, we assumed that each unit area of the slice contributes equally to the total flux, which we normalized to a value of one

when the slice is not eclipsed. This causes us to lose the same percentage of flux as area of the slice being eclipsed at any phase. We assumed that each slice in turn was the X-ray emitting region in order to construct a light curve for each scenario. We then compared our resulting light curves with the actual hard X-ray light curves (Figures 3.3 and 3.4) to determine which slice best reproduces the observed data.

The slice that produces the best fit to the *XMM-Newton* hard X-ray light curve (Figures 3.3 and 3.4) is located 5 $R_\odot$ away from the center of mass on the WN star side, but is not centered on the line connecting the centers of the stars. This region is marked by a solid (black plus grey areas) rectangle in Figure 3.11 and produces the black dotted light curve in Figure 3.12. The location of hard X-ray emitting region implies that the wind momentum ratio for a pure hydrodynamic ram-pressure balance in the system is $\eta = 0.67$. The actual wind momentum ratio is $\eta = 0.058$ (Usov 1992; using the parameters listed above) which implies that radiative forces within the system are very important.

The best fit light curve in Figure 3.12 qualitatively matches many key characteristics of the observed hard X-ray light curves (Figures 3.3 and 3.4). In particular, the modeled secondary eclipse has the same asymmetry as the observed eclipse; the ingress is shorter than the egress. Additionally, the minimum in our modeled light curve is centered on phase 0.55. This is the same phase at which the hard X-ray light curve (Figures 3.3 and 3.4) has a minimum. The modeled secondary eclipse also begins at the same phase (0.45) as the eclipse in the *XMM-Newton* data.

Our best-fit slice creates a light curve that differs from the hard X-ray light curve in several ways. First the secondary eclipse lasts longer than it should; it does not return to a non-eclipse value until phase 0.72, 0.1 in phase later than the *XMM-Newton* hard X-ray light curves. Also, the primary eclipse is much too short and

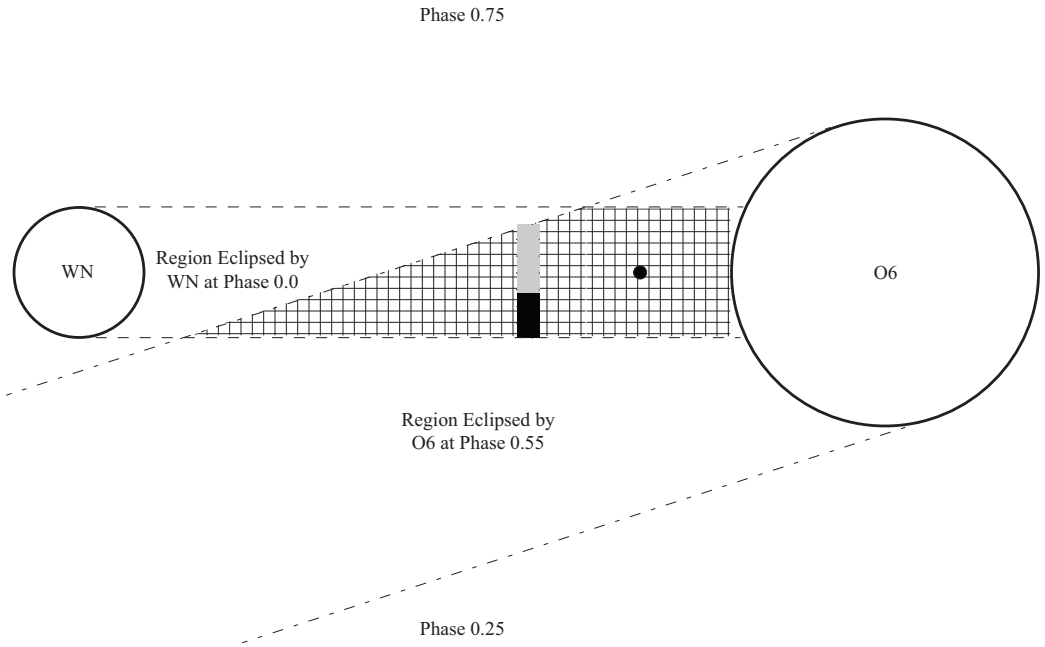

Figure 3.11 Sketch of the geometry of the V444 Cyg system we used in our hard X-ray modeling. The system is viewed from a polar perspective. Dashed lines denote the WN star's shadow at phase 0.0, while dot-dashed lines indicate the region eclipsed by the O star at phase 0.55. The hatched area represents the region of the system occulted during both eclipses. The black dot indicates the center of mass of the system, calculated using the parameters given in Section 3.4. The solid shaded rectangle (black plus grey areas) within the area occulted during both eclipses indicates the region we found to be responsible for the hard X-ray emission using our model (see Section 3.4.1).

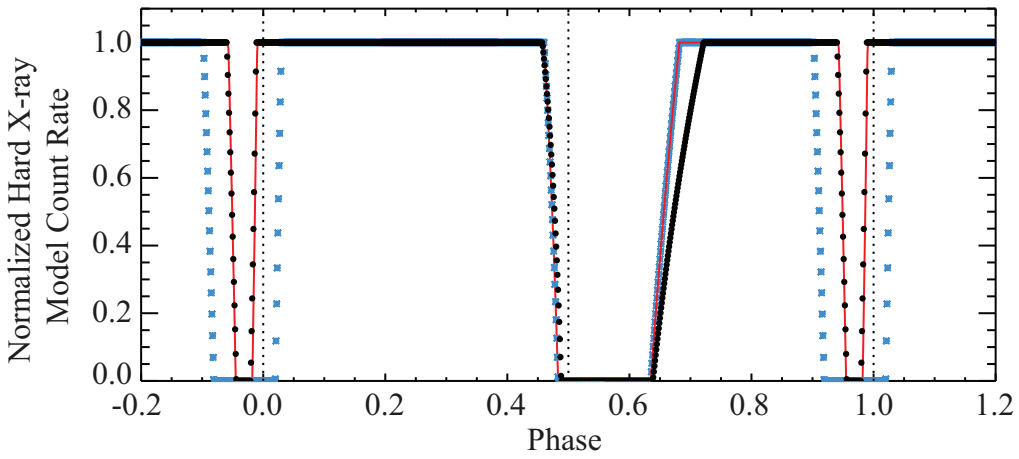

Figure 3.12 Hard X-ray light curve produced using our best fit-model described in Section 3.4.1. The dashed vertical lines represent phases 0.0, 0.5, and 1.0. The data have been wrapped so that more than one complete cycle is shown. The black dots show the modeled light curve using the parameters stated in Section 3.4 and an emitting slice from Figure 3.11 that includes both black and grey rectangles. The red line represents the light curve produced by only the grey rectangle, while the blue asterisks use the grey region and an enlarged WN star (see Section 3.4.1).

is not centered about phase 0.0. We can begin to solve some of these problems by adjusting our model parameters. If we shorten our hard X-ray slice to only the grey region of Figure 3.11 (black region removed), the secondary eclipse recovers to a non-eclipse value by phase 0.68 while still retaining a minimum centered around phase 0.55, an eclipse start at approximately phase 0.45, and the correct asymmetry in enter and exit times (see the red line in Figure 3.12).

In Section 3.3.2 we point out that the depth and duration of the hard X-ray eclipses suggest that the WN star has an apparent radius larger than the value obtained from visual light curve analysis due to its dense wind (Cherepashchuk et al. 1984, St.-Louis et al. 1993). Using the WN stellar radius listed above, our simple model does not produce a primary eclipse long enough to match what is seen in Figures 3.3 and 3.4. We do not try to make an estimate of the apparent size of the

WN star (WR star plus the dense wind region causing the wind eclipse) based on these data but, we do note that making the WN star larger, allowing us to take into account the dense wind region causing the wind eclipse, will lengthen the eclipse around phase 0.0 in our simple model. However, it will not cause the eclipse to be centered around phase 0.0 as seen in the hard X-ray light curves. The blue asterisks in Figure 3.12 show the effects on our model light curve if the WN star has an apparent radius of 8.7 $R_{\odot}$, three times our original adopted size.

3.5.2 Modeling the Absorption of the Hard Component

In Section 3.3.1 we discuss the possibility of a wide opening angle for the shock. We explored this further by using a model to calculate the density of material summed over different lines of sight which correspond to phases. Because the amount of X-ray light absorbed is proportional to density, we can use this model to match the phase-dependent behavior of the absorption parameter we derived for the 2.0 keV spectral fit component (Figure 3.2). With these models, we aim to reproduce three different features of the absorption curve: the long, low absorption column density that runs from approximately phase 0.27 to phase 0.75, the decrease to the low absorption column density, and the slopes of the ingress and egress of the long, low region (phases 0.05 to 0.3 and 0.75 to 0.05; Figure 3.2). We do not try to match the exact column density determined through the spectral fitting; rather, we try to best match the general trends listed above.

We placed the peak of our shock cone where the line of centers of the two stars in the system intersects the location of the hard X-ray emitting region (Section 3.4.1 and Figure 3.11). Therefore it is located 15.9 $R_{\odot}$ from the O star and 20.0 $R_{\odot}$ from the WN star. For simplicity, we did not offset the peak above or below the

line connecting the centers of the stars despite finding that the hard X-ray emitting region is likely not symmetric about the line of centers (Section 3.4.1). We varied the opening angle of the shock and location of its edges by changing the angles α (between 25° and 105°) and β (between 25° and 90°) independently in Figure 3.13 in 5° steps. We assumed a 90° inclination angle for simplicity and summed the density from the peak of the shock cone out to ten times the orbital separation of the stars using the following equation

$$density = \sum_{i=0}^{10R_*} \frac{\dot{M}_*}{4\pi r_i^2 v_*^{\infty}(1 - \frac{R_*}{r_i})}$$

using 1 $R_{\odot}$ steps for sight lines around the binary that correspond to different phases. We use the mass loss rate, radius, and terminal velocity that correspond to the O star for phases where we are looking within the shock cone, and the same values for the WN star for all other phases.

Figure 3.14 shows the model that best reproduces (based on a χ^2 approach) the features of the 2.0 keV absorption column density from Section 3.3.1. It reproduces the long region of low density between phases 0.3 and 0.75 and gives a higher density outside of those phases. Therefore, the overall global trend is well reproduced. However, our model has peaks for sight lines that pass near the surface of both stars. This is acceptable for the phase regions where the WN star's wind dominates the absorption behavior because it produces a peak in the density near the highest column density. However, this behavior is not seen around phase 0.5 but is in our model. Additionally, our model does not produce the dip in column density seen near phase 0.6. In our best fit model the angles α and β are 90° and 70° respectively. This large shock opening angle is necessary to produce the long, low

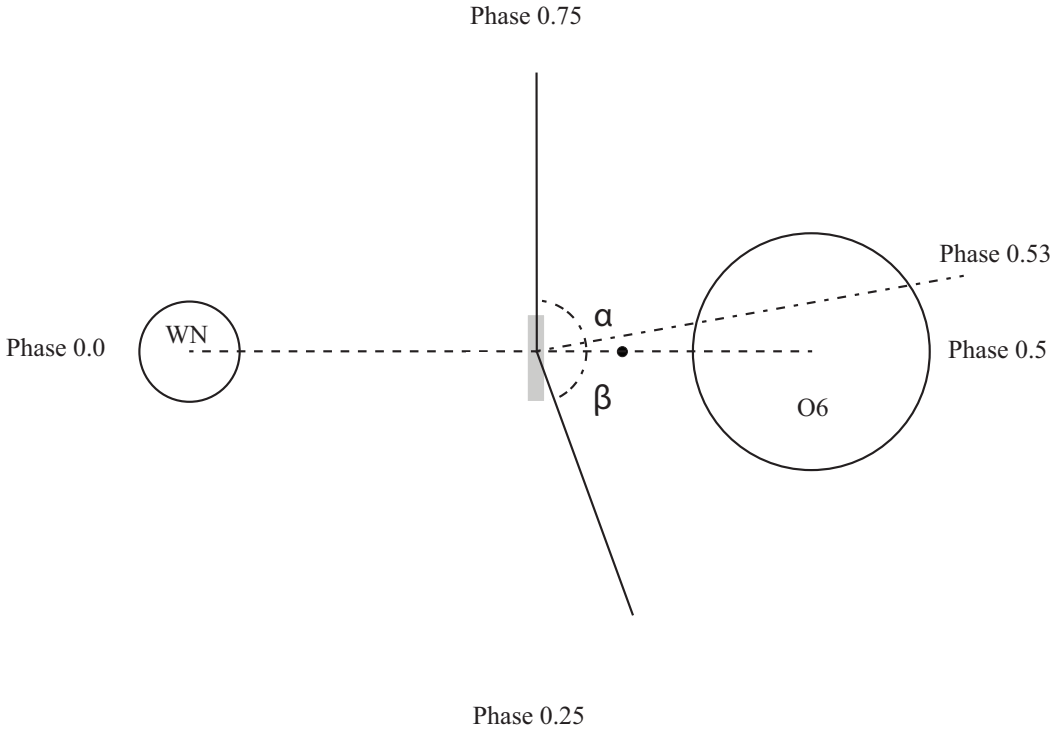

Figure 3.13 Polar view sketch of the geometry used for the absorption model. The dashed line represents the line of centers between the two stars. The dot marks the system's center of mass. The grey rectangle represents the hard X-ray emitting region from the best fit model in Section 3.4.1 (Figures 3.11 and 3.12). The two solid lines represent the walls of the shock cone determined by our absorption modeling. Our best-fitting values for the angles α and β, measured from the line of centers (dashed line), are 90° and 70° respectively. The dot-dash line indicates the shock cone axis.

absorption between phases 0.3 and 0.75 seen in Figure 3.2. These angles are close to identical because the absorption is fairly symmetric about phase 0.5. However, as we mentioned before, the absorption is not enough to understand the changes in the soft light curve (Section 3.3.2) since many factors, including the O star wind being an additional source of soft X-rays, are at play within the system.

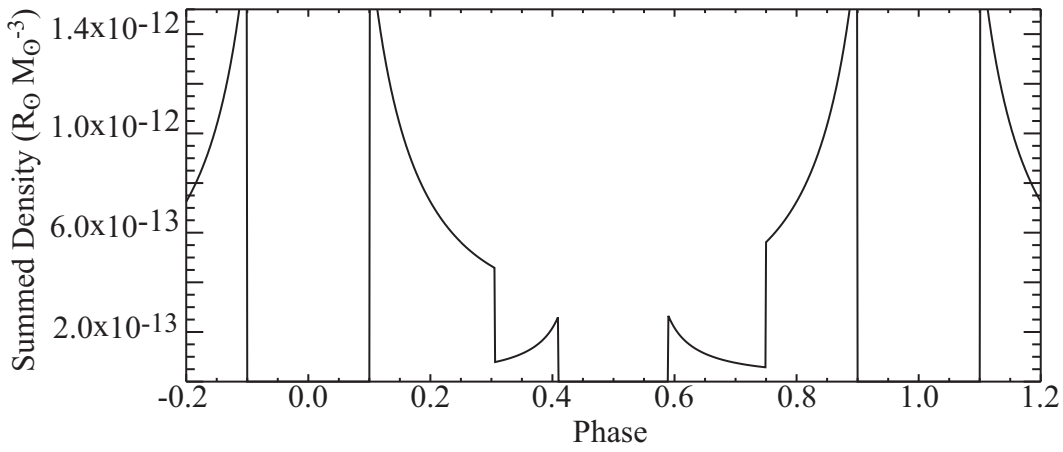

Figure 3.14 Wind density (summed from the center of mass of the system out to ten times the orbital separation) as a function of phase from the best-fit model described in Section 3.4.2. Phases between 0.95–0.05, and 0.37–0.63 are automatically placed at zero density so we do not have to sum through a star. The geometry we used for this model is shown in Figure 3.13. Qualitatively, this result can be compared with Figure 3.2.

3.5.3 Preliminary Polarization Modeling

The polarization observed from the V444 Cyg system is quite complex. In order to properly model the system, several different components need to be taken into account. First, because the system is a binary there should be the normal BME-type variations (Brown et al. 1978). This is complicated by polarization created by electron scattering in the ionized shock and a distortion of the winds from spherical symmetry (St.-Louis et al. 1993). We have conducted preliminary radiative transfer modeling to determine the contribution to the polarization from electron scattering in the shock using a Wilkin-type model (Wilkin 2000). In this case we assumed the WN star's wind is like a dense interstellar medium moving at $v_{WN}^{\infty} = 2500$ km s^{-1} and that the standoff distance between the shock and the O star is the distance implied by the location of the stagnation point from the hard X-ray models (see Sec-

tion 3.4.1). This preliminary work suggests that polarization from the shock alone cannot explain the observed line polarization because it does not predict a polarization of more than 0.1%. However, the result that at least a portion of the polarization is caused by scattering in the shock further suggests that radiative forces are important in V444 Cyg since photons are interacting with the shock material. If radiative breaking or inhibition were not important we would find no net polarization from the shock since photons would not be interacting and scattering with that material. The remainder of the polarization is likely due to scattering within the WN wind which is distorted due to the orbital motion of the system and the cavity described in Section 3.3.3. We are continuing to refine this model to account for eclipse effects, density enhancements within the wind and shock, and emission from sources other than the O star (where our current model assumes it arises) and will report findings in a future contribution. However, we caution that linear line polarization can also be caused by magnetic fields as a secondary effect to circular polarization. Since HPOL cannot measures the Stokes *V* parameter we cannot completely rule out that effect.

3.5.4 Comparison with Other Observational Estimates and Theoretical Predictions

The expected value of the shock half-angle with no radiative inhibition or braking can be calculated using Equation 3 from Eichler & Usov (1993):

$$\theta \simeq 2.1 \left(1 - \frac{\eta^{\frac{2}{5}}}{4}\right) \eta^{\frac{1}{3}}$$

where $\eta = \frac{\dot{M}_{O6} V_{O6}^{\infty}}{\dot{M}_{WN} V_{WR}^{\infty}} \simeq 0.058$ using the system parameters listed above. This gives us a half-opening angle of approximately 42° similar to the estimates of (Shore & Brown 1988; 40°). This is significantly smaller than the half-opening angle we found for the shock using our simple model (approximately 80°; Section 3.4.2). However, our larger value agrees with earlier observational estimates. Flores et al. (2001) find a similar shock opening angle of 70° using the HeII λ4686 line, while Marchenko et al. (1994) initially found an opening angle between 82° and 108° using absorption features in a HeI line and later refined this estimate to 50-60° (Marchenko et al. 1997). Additionally, in their 1997 analysis, Marchenko et al. suggest that one of the bow shock arms crosses our line of sight near phase 0.73. This is very close to when our model suggests a bow shock arm crosses our line of sight (phase 0.75) and further supports the large opening angle interpretation.

Gayley et al. (1997) considered V444 Cyg in their investigation of radiative braking, where the WN star wind may be decelerated through interactions with radiation originating from the O-star in the system. They find that this can significantly affect both the location and opening angle of the shock. In a case of strong raditative braking, the opening angle of the shock can be large; for example, Figure 3c from Gayley et al. (1997) shows a case in which the interaction region between the O and WN stars winds is nearly planar. Although this study assumed slightly different parameters for the V444 Cyg system than ours, the large opening angle we find is consistent with this result and may suggest that strong radiative inhibition or braking is at work in this system. In fact, the results of more recent modeling work that included relatively weak radiative braking (the WN wind still collides with the O-star surface) are comparable to our findings (Pittard & Stevens 1999, Pittard 2002). The models have an opening angle of 120° (compared to our 160°) and one

of the bow shock arms crosses crosses our line of sight at phase 0.72 (we find phase 0.75).

Shore & Brown (1988) found that the projected shock axis should cross our line of sight between phases 0.55 and 0.57, around the same phase as the O star's eclipse of the stagnation point (phase 0.55 from the hard X-ray light curve; Section 3.3.2). Pittard & Stevens (1999) and Pittard (2002) find a similar skew angle (19°) for the shock cone which places the shock axis at about 0.553 in phase. Our absorption model predicts a shock axis near phase 0.53 (Figure 3.13) which is not near the phase where the peak in soft X-ray emission occurs. However, we made several simplifying assumptions in our models, including straight shock cone walls, which do not occur in reality. Proper modeling of the system will eliminate the use of some of these simplifying assumptions.

Combining our data and model information together suggests that the stagnation point is not located at the peak of the shock cone. It is possible that this is because we made the assumption that the shock cone peak lies on the line of centers of the two stars while we have shown that the stagnation point is not symmetric about this line, i.e. if we allow the shock cone peak to be located off the line of centers there may no longer be a difference between the phase location of the shock peak and the stagnation point. However, our data alone suggests that they are likely not located at the same position; the hard X-ray light curve's secondary eclipse (phase 0.55, Figures 3.3 and 3.4) does not occur in the exact middle of the long low absorption feature (Figure 3.2). We expect that further future modeling will clear up this matter by determining their locations in a more precise manner.

Modeling using radiative braking also suggests that the location of the stagnation point is at $1.6R_*$ from the center of the O-star although we note that this result

is from modeling that used slightly different system parameters from what we use here (Gayley et al. 1997). Using our parameters, this gives a location very close to the center of mass of the system (see Figures 3.11 and 3.13). In the case of no or low radiative braking the WN star wind would collide directly with the O-star, so while our stagnation point location is not formally consistent with that found in Gayley et al. (1997) which is partially due to the small difference in system parameters, it still suggests that the WN star wind is strongly affected by radiation from the O-star.

The use of appropriate stellar wind parameters for both stars in models is important to give adequate descriptions of the X-ray and polarimetric behaviors of the system. Over the years a wide range in the wind parameters has been found for the system. In our two X-ray models different mass loss rates and terminal velocities would not significantly affect our results. The hard X-ray model is not dependent on wind parameters since it considers eclipse effects only. However, the model of the hard component's absorption does depend on wind parameters. In this case, the results are not effected because a higher (lower) mass loss rate would only increase (decrease) the density we calculate and a faster (slower) terminal velocity would decrease (increase) the calculated densities. Therefore, only the winds' relative densities would change (raising or lowering different sections of the curve in Figure 3.14). They do not affect the locations of the walls of the shock cone which is what we are most interested in and are controlled by the α and β parameters within our model. However, more complex X-ray models of the system will rely on accurate determinations of the wind parameters. Polarimetric models also need these to be accurately determined since they will affect the number of scatterers in each star's wind. Therefore, a dedicated investigation of these parameters is needed.

3.6 Summary

We have presented a new data set of X-ray observations of V444 Cyg in the 0.4 to 10 keV energy range which we used to create the most complete set of X-ray light curves of the system to date. Supporting polarimetric observations of the system for several emission lines are also presented.

From our X-ray spectral fitting, we found the absorption of the cold component to be low due to that emission forming in the winds of the system far from the stars. Additionally, the normalization of the cold component increases when the O star is in front because the intrinsic emission of the O star wind becomes visible. We found the variation of the absorption of the hard component is due to the orientation of the system; a higher absorption occurs when the WN star is in front and the duration of the low absorption implies a wide shock opening angle.

Our polarization results suggest that the shock creates a cone of missing material in the HeII and NIV shells around the WN star. Additionally, they are suggestive of a large opening angle for the shock which is consistent with our X-ray spectral analysis and shows radiative forces are present within the system.

We created X-ray light curves of the system in three energy bands: 0.4 to 2 keV, 2 to 10 keV, and 0.4 to 10 keV. We found the variation in the soft count rate to be due to both a varying emission and varying absorption of the X-rays; when the less dense wind (O star wind) is in front there is a higher count rate because of a lower absorption of those photons. We have detected the effects of Coriolis distortion in the V444 Cyg: we found an asymmetry in the variation of the soft count rate due to the orbital motion of the system. Additionally, we found that the variations in the hard X-ray light curve are due to physical eclipses of the stagnation point. The

depth of the primary eclipse is explained by the wind of WN star in addition to the star itself occulting the hard X-ray emitting region. We found the asymmetry of the phase 0.55 eclipse of the hard count rate is due to the emitting region not lying symmetrically about the line of centers of the two stars due to Coriolis distortion. Our models of the hard X-ray light curve are consistent with this result. We also modeled the absorption of the soft X-ray component from our spectral fits and found the shock cone to be asymmetric about the line of centers as well.

Our results suggest that radiative braking plays an important role in both the location and opening angle of the shock. We expect that future, more complete modeling of our data sets and higher signal to noise spectropolarimetric observations will provide additional geometric and radiative insights into the V444 Cyg system and other short period colliding wind systems like it.

Chapter 4

RXTE Monitoring of the WR 140 Colliding Wind Binary

Jamie R. Lomax, Michael F. Corcoran, Andy M. T. Pollock, and Jennifer L. Hoffman (in prep.)

4.1 Abstract

We present results of light curve and spectral analysis from eleven years of X-ray monitoring of the WR 140 system with the *Rossi X-ray Timing Explorer* in addition to compiling all existing optical spectropolarimetric observations of the system. We find evidence for intrinsic hard X-ray emission from the system possibly due to inverse Compton scattering. An alternate scenario in which the low-energy thermal tail causes the observed hard X-rays is also considered. We find significant polarimetric variability within two of the three existing data sets and argue that higher

cadence polarimetric monitoring of the system, particularly in and around the next periastron passage, is needed to better understand the formation of dust in WR 140.

4.2 Introduction

WR 140 is a massive, colliding wind binary made up of an evolved WC7 star (19 $M_\odot$) and a more massive (50 $M_\odot$) O4-5 main-sequence companion (Marchenko et al. 2003). The mass loss rates of both stars are high, 1.2×10^{-6} $M_\odot$ yr^{-1} for the O star and 3.8×10^{-5} $M_\odot$ yr^{-1} for the WC star (Zhekov & Skinner 2000), while the terminal velocities are similar, 3200 km s^{-1} for the O star and 2860 km s^{-1} for the WC star (Zhekov & Skinner 2000), which causes a shock to form between the two stars.

Its high eccentricity (0.88) and long period (7.9 years) (Marchenko et al. 2003) are what make WR140 interesting; the system's stellar separation varies anywhere from 2 AU at periastron to 30 AU at apastron, and causes variations to be seen in many wavelength regimes (Fahed et al. 2011, Dougherty et al. 2005, Taranova & Shenavrin 2011). Episodic dust formation has been detected in the infrared and observations also show periodic non-thermal radio emission from the system (Dougherty & Williams 2000, Dougherty et al. 2005, Williams et al. 2009, Taranova & Shenavrin 2011). These variations are tied to the changing characteristics of the shocked gas caused by the orbit of WR 140. Therefore, studying the phase dependence of the shock's characteristics is extremely important in trying to understand the mass loss of the WR 140 system.

WR 140 was first detected in X-rays by *EXOSAT* and has since been observed by *ASCA*, *XMM-Newton*, *Suzaku*, and *Chandra*. As expected for a colliding wind

binary with a high eccentricity, all of these observations show that the X-ray variability can be qualitatively explained by phase-locked variations in the emission measure and absorbing wind column densities. The *EXOSAT* observations were the first to reveal the strong absorption of X-rays when the WR star is in front (phase 0.008) compared to other phases (Williams et al. 1990). This was later confirmed with the *ASCA*, *XMM-Newton*, *Chandra*, and *Suzaku* observations (Zhekov & Skinner 2000, Pollock et al. 2005, De Becker et al. 2011, Sugawara et al. 2011). WR 140's X-ray emission does not follow the expected inverse distance trend in any set of observations near periastron passage (De Becker et al. 2011, Sugawara et al. 2011); in order to fully understand the shock properties more complex modeling of the system is needed, including 3D hydrodynamical and radiative transfer models (De Becker et al. 2011). Additionally, the *Suzaku* observations hint at high energy X-ray emission from the system due to inverse Compton scattering (Sugawara et al. 2011). If confirmed with would be only the second colliding-wind binary for which such emission has been detected.

Recently, high cadence X-ray monitoring of the WR 140 system was conducted using the *Rossi X-ray Timing Explorer* (*RXTE*). The goal of these observations were to study the X-ray flux variations in order to better understand the response of the shock to changes in density (Corcoran et al. 2011). These observations have created the fullest light curve of the system to date, and clearly show an absorption feature when the WR wind is in front of the shock.

Schulte-Ladbeck et al. (1995) obtained the earliest polarimetric observations of the WR 140 system. Their monitoring started in 1985 with seven observations taken over three years with the Lyot instrument (Lupie & Nordsieck 1987, Whitney & Clayton 1989, Nook et al. 1990) at Pine Bluff Observatory (PBO). They

later continued monitoring efforts with the University of Wisconsin's Half-Wave Spectropolarimeter (HPOL) at the same observatory (Wolff et al. 1996). Starting in 1989 and continuing through 1993 they obtained an additional twelve observations. Robert et al. (1990) also monitored WR 140 in both 1985 and 1986 and were able to observe the system significantly more often than Schulte-Ladbeck et al. (1995). Even though both monitoring campaigns resulted in poor coverage of a significant portion of the total light curve, Schulte-Ladbeck et al. (1995) showed that the system appeared to be more variable just after the 1985 periastron passage than before the 1993 periastron passage and concluded that polarimetric variability is likely due to scattering in dust blobs.

In order to gain new information about the dynamics within the shock, we use the data from the *RXTE* monitoring campaign to study the possibility of high energy X-ray emission due to inverse Compton scattering originating from within the system. Additionally, we combine all archival spectropolarimetric observations from WR 140 into one light curve in an attempt to better understand the signatures seen within those data. In the next sections of this paper we present the details of the *Rossi X-ray Timing Explorer* (*RXTE*) monitoring and polarimetric observations of the system (Section 4.3), discuss the results of those observations (Section 4.4), and propose some interpretations of those data (Section 4.5). In Section 4.6 we summarize our findings.

4.3 Observations

This study makes use of observations from two separate data sets. Our first data set consists of a large number of X-ray spectral observations taken with *RXTE*

(Corcoran et al. 2011). The second set consist of optical spectropolarimetric data taken with the Lyot and HPOL instruments at the University of Wisconsin's Pine Bluff Observatory (PBO) from Schulte-Ladbeck et al. (1995). We combine these data with archival polarimetric observations previously published by Robert et al. (1990).

We calculated phases for all the observations using the ephemeris given by

$$T_{peri} = 1985.2 + 7.9318E$$

where E is the number of orbits since the periastron passage occurring on 1985.2 in decimal years. This ephemeris was calculated from the *RXTE* data (Corcoran et al. 2011) and is two days shorter than the previous best estimate (Marchenko et al. 2003).

4.3.1 *Rossi X-ray Timing Explorer*

WR 140 was observed with *RXTE* 553 times between December 2000 and December 2011. Observations ranged in length from 521 seconds to 3010 seconds with the mean and median exposure times being 1083 seconds and 949 seconds respectively. The interval of time between observations changed over the 11 years of observations in order to provide appropriate phase coverage. Between December 2000 and March 2003 observations were conducted approximately once a week. Observations resumed in March 2005 and were conducted once every two weeks through June 2007. Between July 2007 and July 2008 observations were again conducted once a week. Then starting on 7 August 2008 observations were conducted on approximately a daily basis until 23 March 2009. Weekly observations resumed

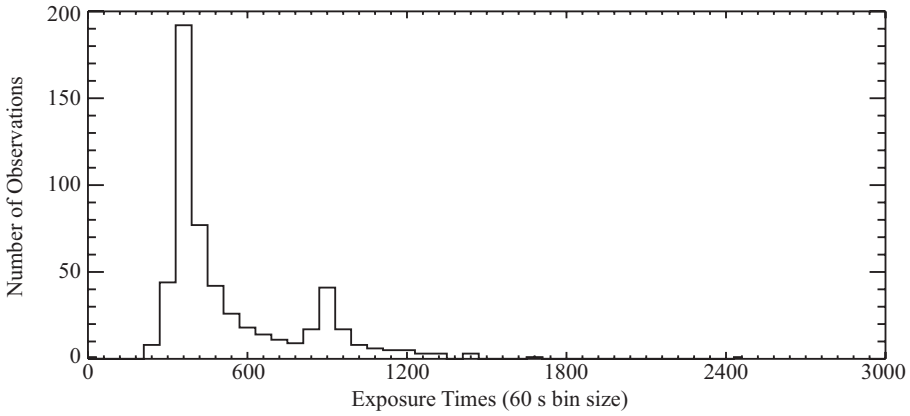

Figure 4.1 Histogram of exposure times for the *RXTE* observations with 60 second bins.

on 31 March 2009 and ended in December 2009. Between January 2000 and December 2011 observations were conducted every other week again. At that time monitoring of WR 140 with *RXTE* ceased due to discontinued operations of the satellite. Figure 4.1 gives a histogram of the exposure times for the *RXTE* data.

We use data from *RXTE* taken with the proportional counter array (PCA) which is made up of five single element proportional counters (PCUs 0 through 4). Damage to the propane layer in two PCUs has caused their backgrounds to be less well known and have a higher variability than normal. Similarly, two other PCUs were not turned on for every observation in order to attempt to preserve the instrument's longevity. PCU2 was the only one on with an adequate understanding of the background for the entire set of *RXTE* observations. In the sections below we present all the data in the light curves, but the large amount of scatter in the non-PCU2 data can be attributed to these factors. In our spectral fitting we only present PCU2 data.

Additionally, the PCA instrument was designed to provide high time resolution data (on the order of microseconds). This, in combination with the fact that the detectors are proportional counters means that the spectral resolution of the in-

strument is low. Additionally, since the observations were designed to monitor the flux variations from WR 140 on daily, monthly, and yearly timescales integration times were not high enough to result in low errors on the count rate at high energies despite observations occurring within the 2-60 keV band.

4.3.2 Pine Bluff Observatory Polarimetry

A portion of the polarimetric observations presented here were conducted with two separate polarimeters at PBO and originally published in the IAU proceedings by Schulte-Ladbeck et al. (1995). We have seven observations taken with the Lyot polarimeter between 1985 and 1987 spanning the 4600-7200Å wavelength range. Further details about the Lyot polarimeter at PBO can be found in Lupie & Nordsieck (1987), Whitney & Clayton (1989) and Nook et al. (1990). Twelve additional observations were taken with HPOL at PBO between 1989 and 1993 using a Reticon detector. These observations span a larger wavelength range (3200-7600 Å) with a resolution of 15 Å (see Wolff, Nordsieck & Nook 1996 for further instrument information). The Lyot and HPOL instruments differ in that HPOL is a low-resolution spectropolarimeter while the Lyot polarimeter observed sources at a few distinct wavelengths across the optical spectrum. All HPOL observations were reduced using the REDUCE software package (described by Wolff et al. 1996). Table 4.1 lists the orbital phases, along with the civil and heliocentric Julian dates for the midpoints of the HPOL and Lyot observations.

4.3.3 MINIPOL Polarimetry

In addition to the polarimetric observations taken at PBO we have also made use of archived observations taken with the MINIPOL polarimeter at Mount Lemmon and Mount Bigelow observatories in the 1985 and 1986 years. A blue Corning filter was used with a central wavelength of 4700 Å and a full width half maximum of 1800 Å. Further details of these observations can be found in Robert et al. (1989) and Robert et al. (1990).

None of the observations are corrected for interstellar polarization (ISP). While the observed polarization behavior is contaminated with ISP, any deviations in the light curve from a constant are due to variations in the scattering of light from WR 140 because the ISP is not variable on the same time scale as the system.

Table 4.1: Date and Phase Information for Midpoints of the WR140 HPOL and Lyot Observations

Date	HJD	Phase	Instrument	Observer
1985 Jun 06	2446222.50	0.0229	Lyot	···
1985 Jul 03	2446249.50	0.0322	Lyot	···
1986 Jun 23	2446604.50	0.1548	Lyot	···
1986 Aug 09	2446651.50	0.1710	Lyot	···
1986 Aug 16	2446658.50	0.1734	Lyot	···
1987 Apr 04	2446889.50	0.2532	Lyot	···
1987 Jul 17	2446993.50	0.2891	Lyot	···
1989 Aug 18	2447756.25	0.6330	HPOL	Mary J. Taylor
1989 Aug 25	2447763.21	0.6351	HPOL	Mary J. Taylor
1991 May 31	2448407.36	0.8575	HPOL	Graham Knopp
1991 Dec 24	2448614.09	0.9293	HPOL	Graham Knopp
1992 May 07	2448749.35	0.9753	HPOL	Mike Wolff

Continued on Next Page...

Table 4.1 – Continued

Date	HJD	Phase	Instrument	Observer
1992 Aug 09	2448843.38	0.0077	HPOL	Debra Shepherd
1992 Sep 19	2448884.15	0.0223	HPOL	Shawn Diamond
1992 Dec 21	2448977.10	0.0544	HPOL	Nicolle Zellner
1993 Apr 03	2449080.43	0.0896	HPOL	Erich Kleditz
1993 Apr 04	2449081.41	0.0900	HPOL	Shawn Diamond
1993 May 06	2449113.34	0.1014	HPOL	Nicolle Zellner
1993 Dec 11	2449332.12	0.1770	HPOL	Jaime Hanson

Phases were calculated using the ephemeris in Section 4.3. Information about the Lyot instrument can be found in Lupie & Nordsieck (1987), Whitney & Clayton (1989) and Nook et al. (1990). Similarly, HPOL information is in Wolff et al. (1996).

4.4 Results

Due to *RXTE*'s large field of view, WR 140 is not the only X-ray source observed. An active galactic nucleus (AGN; IGR J20216+4359) is located 17' away (therefore has a lower count rate than if it were on axis due to *RXTE*'s relative transmittance) from WR 140 within the *RXTE* field of view and contaminates the PCA data at high (greater than 20 keV) energies. Bikmaev et al. (2008) discovered this AGN in *INTEGRAL* observations. In the analysis of both the *RXTE* spectra and light curves, we take steps to account for this extra X-ray emission and describe the details of this analysis in their respective sections below.

4.4.1 *RXTE* Spectra

For each *RXTE* observation, we fit the the data with the XSPEC software package (Arnaud 1996; v12.7.1) using the following two-component model:

$$(wabs \times apec) + (wabs \times powerlaw)$$

where $wabs$ is the photo-electric absorption of the X-rays, $apec$ is an X-ray emission spectrum, $powerlaw$ is a photon power law. The first term accounts for X-ray emission and absorption from WR 140 and the second term accounts for emission and absorption from the AGN.

For each observation we place several constraints on the free parameters within our fits to ensure realistic results. Bikmaev et al. (2008) fit the *INTEGRAL* observations of the nearby AGN (1.6×10^{-11} erg s^{-1} cm^{-2}) with a power law whose photon index was 2. Their analysis of *ASCA* observations used a similar photon index (1.7) and revealed the absorption column density to be high ($13 \pm 2 \times 10^{22}$ cm^{-2}). Therefore, we limit the range of the photon index of the second component to be between 1.5 and 2.5, and constrain the range of the absorption column to be 11-15$\times 10^{22}$ cm^{-2}.

Using the following system parameters we also place constraints on the free parameters in the first component of our model spectrum: terminal velocities of 2860 km s^{-1} (WR star) and 3200 km s^{-1} (O star); mass loss rates of 3.8×10^{-5} M$_{\odot}$ yr^{-1} (WR star) and 1.2×10^{-6} M$_{\odot}$ yr^{-1} (O star); and stellar radii of 12 R$_{\odot}$ (O star) and 13 R$_{\odot}$ (WR star) (Pollock et al. 2005, Zhekov & Skinner 2000). A collision at

these terminal velocities produces a shock with a temperature of

$$T_s = \frac{3}{16}\mu V_\infty^2 R^{-1} \approx 1.55 \times 10^8 \mathrm{K} \approx 13\mathrm{keV}$$

where R is the gas constant, and $\mu = 4$ is the mean molecular weight (Castor 1987). In an abundance of caution, we use double this value as a maximum possible temperature for the shock and constrain the minimum to be no less than 2.5 keV. This is due to the unknown response of the instrument below 2 keV because no data exist there. Similarly, we place constraints on the column density using the equation

$$n_H = \int_r^\infty \frac{\dot{\mathrm{M}}}{4\pi r^2 v(r) \mu m_H} dr$$

where $v(r) = v_\infty(1 - \frac{R_*}{r})^\beta$, m_H is the mass of the hydrogen atom, $\beta = 1$, and μ is the mean molecular weight of the material in the wind. We assume a distance to WR 140 of 1.1 kpc (van der Hucht 2001) and a mean molecular weight of $\mu = 4$ (helium) for the WR wind since it is the denser wind. This gives us a column density of $n_H = 14 \times 10^{22}$ cm^{-2}. Again, we double the value to obtain an upper limit for the column density (30×10^{22} cm^{-2}) since the estimate was only calculated from the WR surface outward and never through the shock. We use an average interstellar medium value (0.5×10^{22} cm^{-2}) as a lower limit.

Figure 4.2 shows two sample spectra from the *RXTE* observations at phases 0.534 and 1.000 and their model spectra that resulted from our fitting procedure. Most of the changes in the spectra and their fits occur at low energies (below 4 keV) but the fits also vary from each other at higher energies (between 7 and 20 keV) despite the data appearing to be similar. At low energies the spectra show

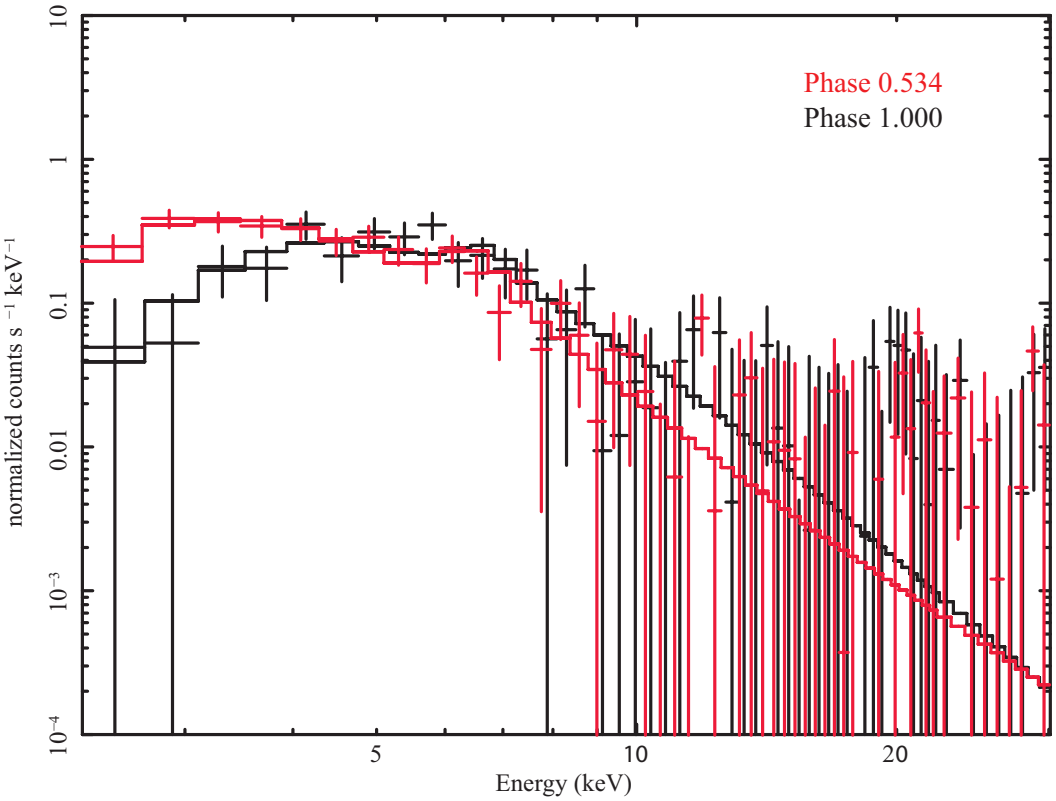

Figure 4.2 Sample *RXTE* spectrum for observations at phases 0.534 (red) and 1.000 (black). Data points are represented by crosses and the model from the fitting procedure is shown as a solid line.

strong absorption effects when the WR star wind is in front causing a lower count rate. At higher energies the changes are not as clear but the fits differ slightly.

Figures 4.3 and 4.4 display the phase variability of the parameters from both components of our spectral fits to the data from PCU2 on board *RXTE*. In Figure 4.3 the column density and temperature of the thermal component show all of their variability near periastron passages and low constant behaviors outside of periastron. Both components increase and peak just after periastron passage before returning to the low constant behavior. The constant behavior is partially an arti-

fact of our imposing upper and lower limits on these parameters. Both the column density and the temperature reach the lower limit outside periastron, but only the column density reaches the upper limit. It does so for a brief period just after periastron passage.

In contrast to the column density and temperature, the normalization of the thermal component in Figure 4.3 shows a low, but smooth and slow variability outside of periastron passage. Just before periastron passage the normalization peaks before undergoing a sharp drop whose minimum occurs just after periastron. The normalization recovers from this minimum, but does not come back to the same value before returning to the smooth and slow variability. Figure 4.5 shows the same parameters around periastron. Both the column density and temperature start to vary at the first quadrature phase while the normalization begins its quick variations before that. The maximum column density and temperature occur after the conjunction when the WR star is in front in our line of sight (phase 0.008), and return to their constant behavior at about the same phase and before the next quadrature.

The behavior of the thermal component of our model spectrum is consistent with previous X-ray studies of the system (Williams et al. 1990, Zhekov & Skinner 2000, Pollock et al. 2005, Sugawara et al. 2011, De Becker et al. 2011, Corcoran et al. 2011). The increase in column density just after periastron passage can be explained by the X-ray emission being absorbed in the WR wind, which is in front of the shock in our line of sight at those phases. The normalization tracks an increase in emission measure (the normalization is just the emission measure scaled by 4π times the distance) near periastron passage and the increase in the absorbing column just after periastron passage, and shows a behavior very similar to the light curves of the system (Section 4.4.2).

Figure 4.4 shows the resulting parameters for the powerlaw (2nd) component of our spectral fitting. The normalization shows all of its variability around periastron passage and is relatively constant at other phases. The photon index and column density show more variability and are often pegged at either the upper or lower limit. The column density is mostly at the lower limit that we placed on the power law component, but when it does reach the upper limit it appears to not be a phase dependent behavior. Most of the scatter in the column density between the two limits occurs near periastron passages. The photon index shows similar behavior: it gets pegged at both the upper and lower limits in a random manner. Similarly to the column density, the photon index also shows scatter between the two imposed limits mostly around periastron passage.

Figure 4.6 shows the same data but only for the phase region around periastron passage to make the variability easier to see. All of the scatter away from an upper or lower limit in the column density occurs just after the phase when the WR star is in front in our line of sight. The normalization shows significant phase-locked variability. It first peaks between the first quadrature and periastron, then reaches a minimum after conjunction (when the WR star is in front) and peaks again before returning to its outside of periastron passage behavior. This variability is qualitatively similar to the behavior of the normalization of the thermal component which has analogous peaks and troughs. We discuss the behavior of the power law component more in Section 4.5.1 where we compare it to the behavior of the system's light curves.

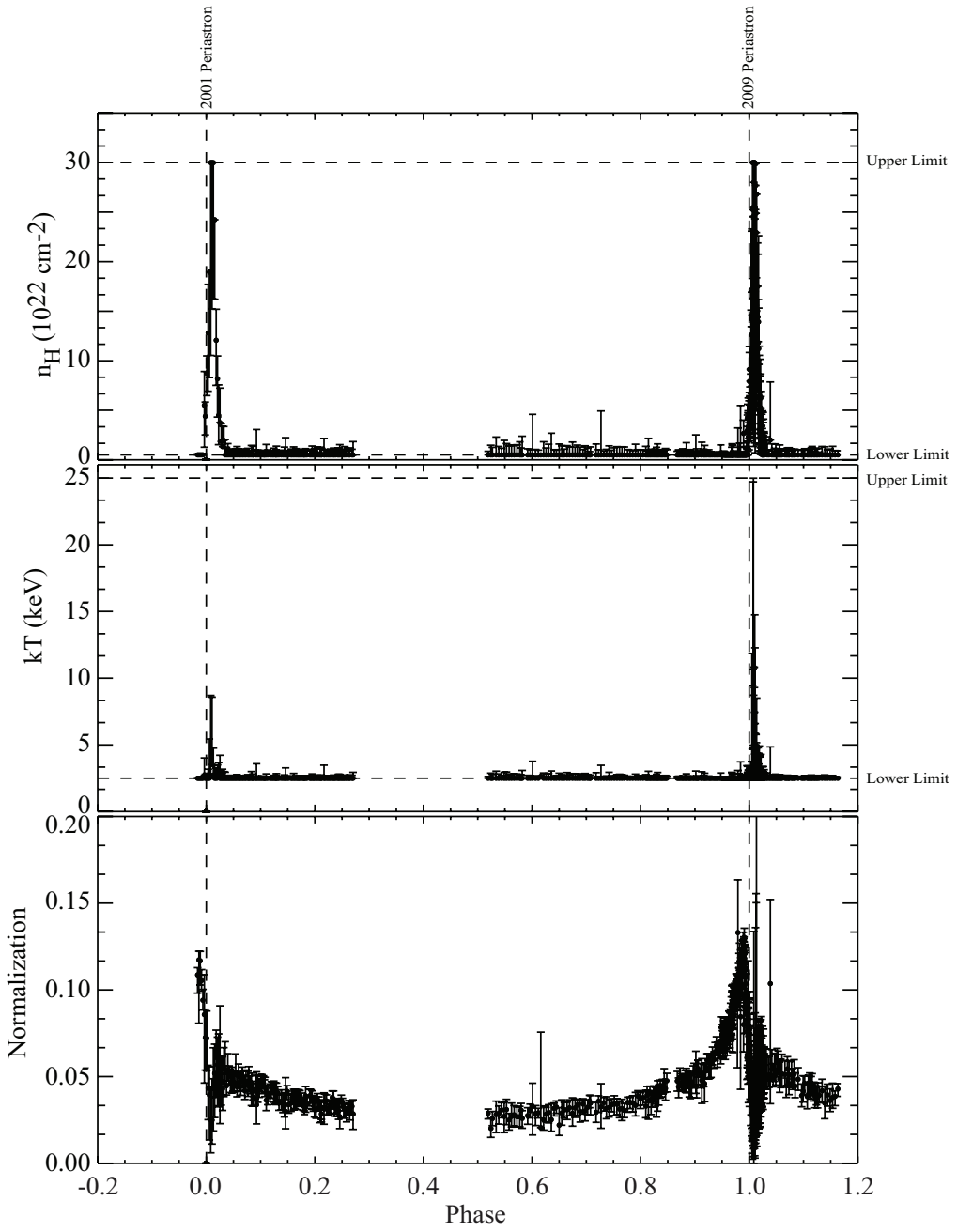

Figure 4.3 Parameters from the thermal component of the spectral fits of the PCU2 data. *From top:* Column density, temperature, and normalization versus phase. Vertical dashed lines mark the 2001 and 2009 periastron passages (phases 0.0 and 1.0) while horizonal dashed lines show the upper and lower limits we imposed on our fitted parameters (see Section 4.4.1).

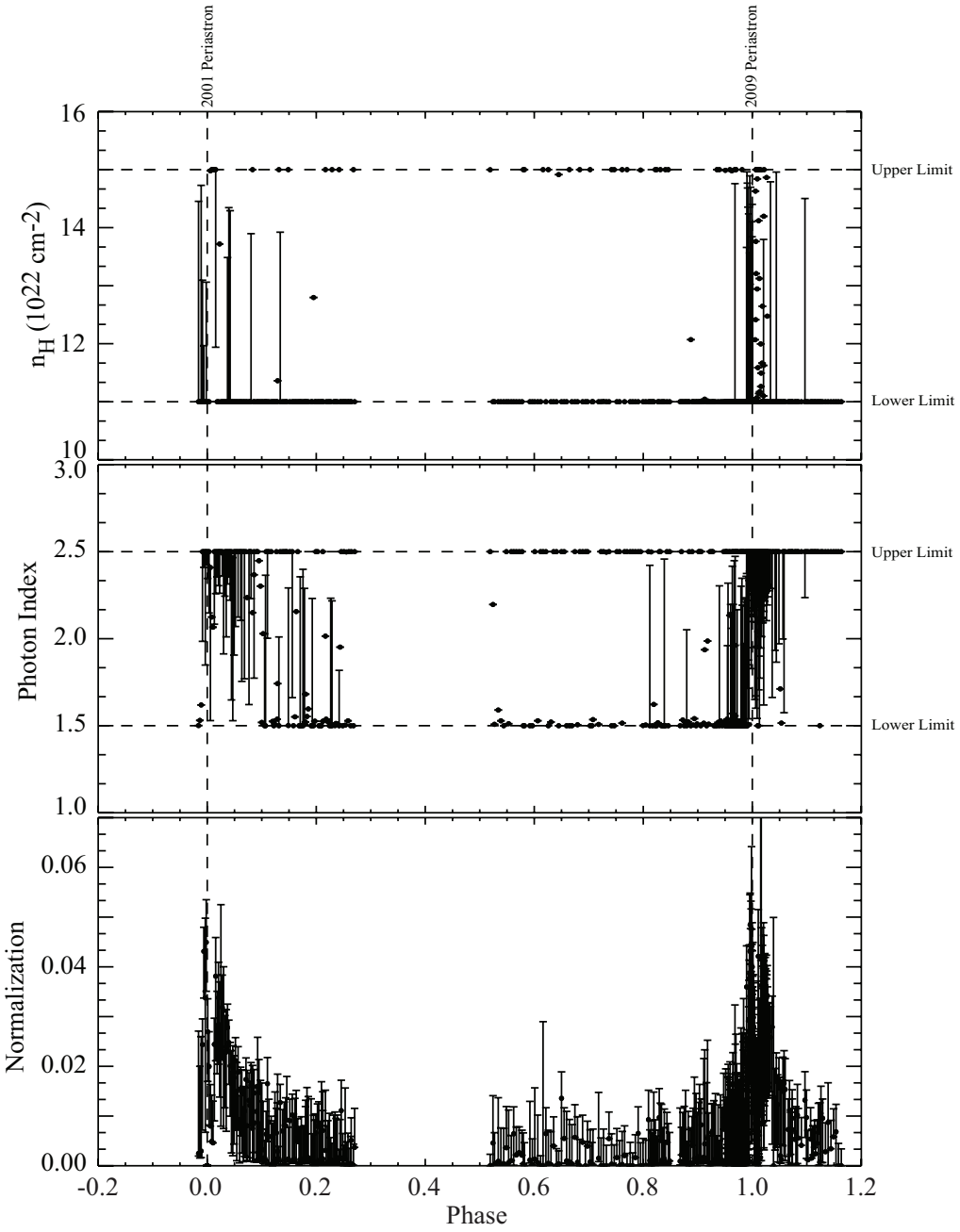

Figure 4.4 Parameters from the power law component of the spectral fits of the PCU2 data. *From top:* Column density, photon index, and normalization versus phase. Vertical dashed lines mark the 2001 and 2009 periastron passages (phases 0.0 and 1.0) while horizonal dashed lines show the upper and lower limits we imposed on our fitted parameters (see Section 4.4.1).

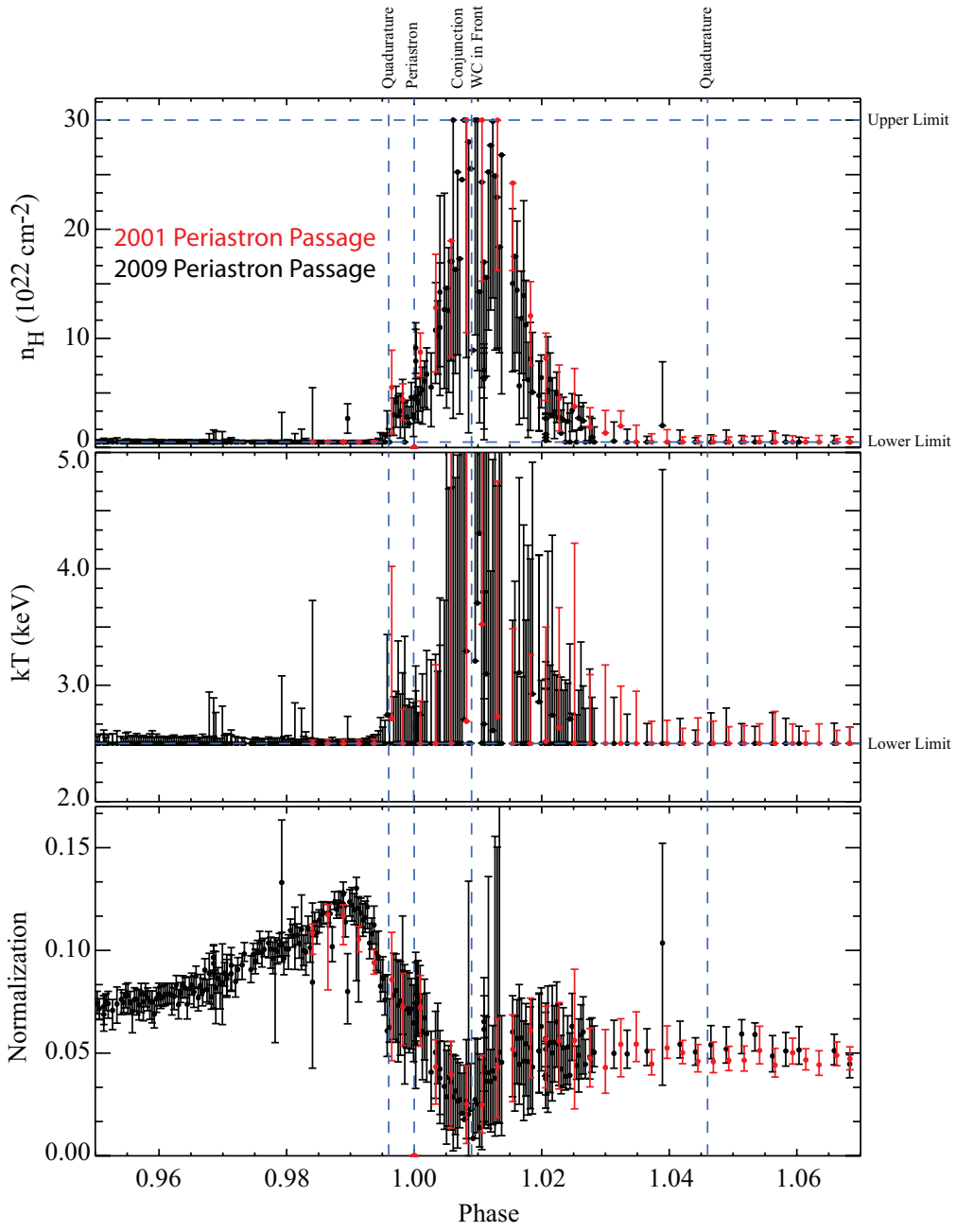

Figure 4.5 Same as Figure 4.3 but zoomed into the region around periastron passage. Data points have been wrapped so that both the 2001 (red) and 2009 (black) periastron passages are shown. Vertical dashed lines mark periastron (phase 1.0), both quadratures (phases 0.996 and 1.046), and when the WR star is in front in our line of sight (phase 0.004).

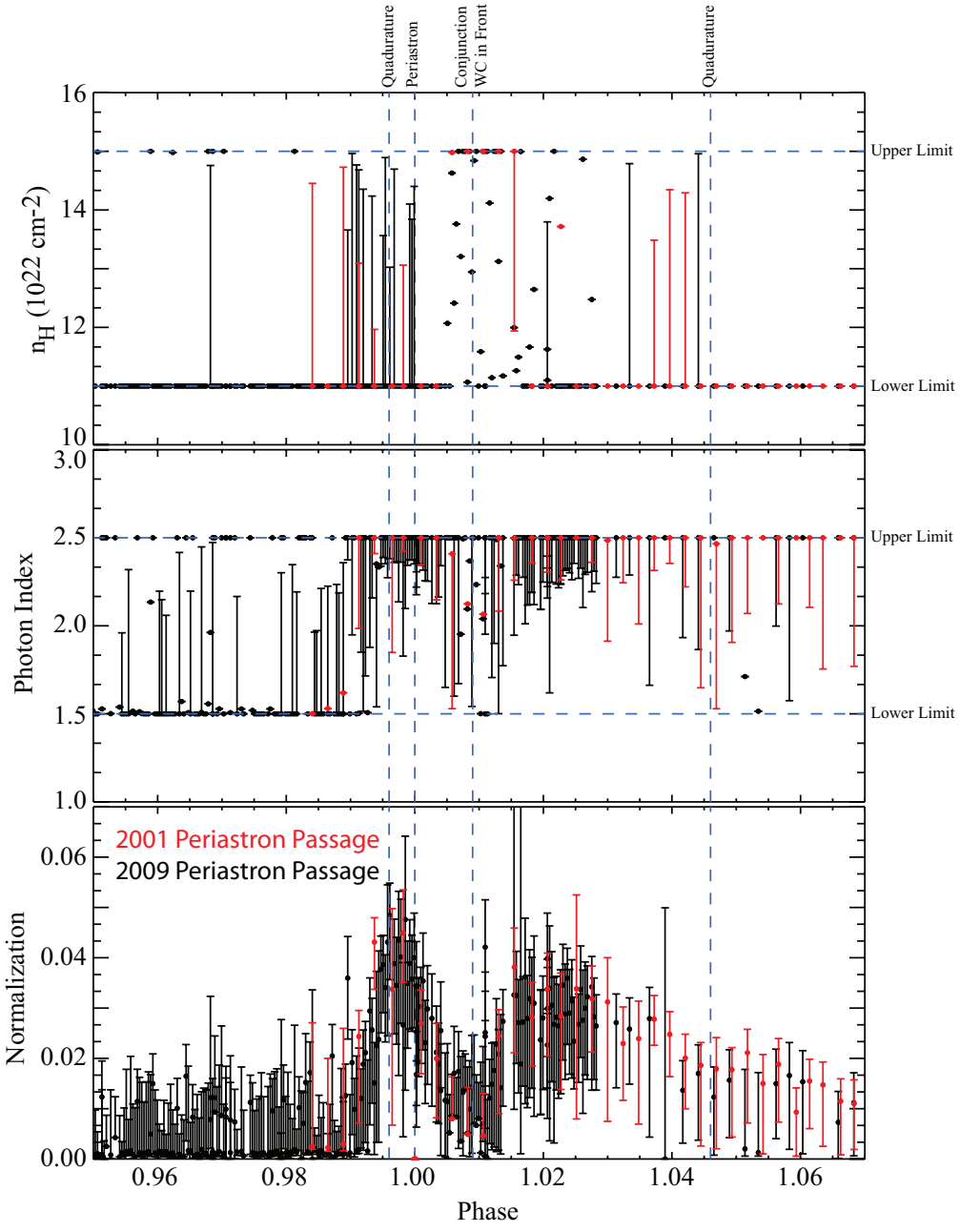

Figure 4.6 Same as Figure 4.4 but zoomed into the region around periastron passage. Data points have been wrapped so that both the 2001 (red) and 2009 (black) periastron passages are shown. Vertical dashed lines mark periastron (phase 1.0), both quadratures (phases 0.996 and 1.046), and when the WR star is in front in our line of sight (phase 0.004).

4.4.2 *RXTE* Light Curves

Figure 4.7 shows the 2-10 keV light curve of the WR 140 system. At phases near apastron (2.5 to 2.6) the count rate is constant. However, as periastron approaches, the count rate increases, until just before periastron where a sharp drop in the count rate occurs. The X-ray flux increases after periastron passage, but not to the same count rate before declining back to apastron values. The sharp drop around periastron passage occurs when the WR star's wind is in our line of sight causing significant absorption of the emitted X-rays, while the increase to maximum occurs as the shock gets stronger when the stars' orbital separation drops. This result is consistent with previous X-ray observations despite their sparse of phase coverage compared to this data set (Pollock 1985, Zhekov & Skinner 2000, Pollock et al. 2005, De Becker et al. 2011, Sugawara et al. 2011). It is also consistent with the results of our spectral fitting (Section 4.4.1). The scatter in PCUs other than PCU2 are due to a poor understanding of the background due to damage to the detectors.

To better understand how the light curve behaves at different energies, we extracted the source and background counts from each *RXTE* observation in the 2-5 keV, 5-7.5 keV, 7.5-10 keV, 10-15 keV, 15-20 keV, and 20-60 keV energy ranges. We then calculated the count rate in each band for all the observations with the following equation

$$\text{count rate} = \frac{\text{source counts} - \text{background counts}}{\text{exposure length}}$$

where the exposure length is in seconds. Figure 4.8 shows the resulting 2-5 keV, 5-7.5 keV, and 7.5-10 keV light curves and Figure 4.9 shows the light curves of the remaining three bands. To improve uncertainties we binned the data to 0.01 in

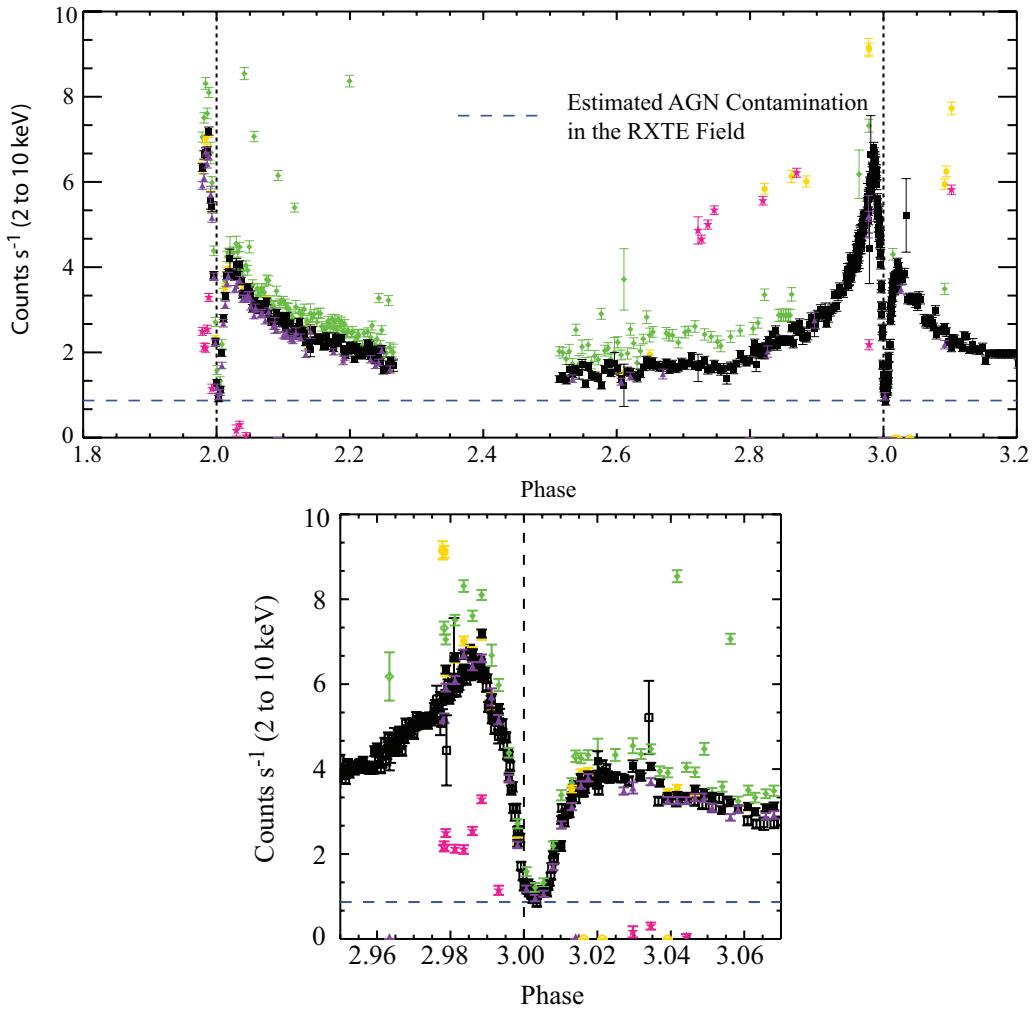

Figure 4.7 X-ray count rate from the *RXTE* observations. Colors and point styles represent the different PCU's within the PCA instrument (green diamonds=PCU0, yellow circles=PCU1; black squares=PCU2; pink stars=PCU3; and purple triangles=PCU4). Vertical dotted lines indicate periastron passages (2001 passage is at phase 1.0 and the 2009 passage is at phase 3.0). Dashed blue horizontal lines represent the estimated AGN contamination in the *RXTE* field for WR140. The top panel is the full light curve while the bottom panel shows a zoomed in portion near periastron passage. In the bottom panel open points represent data from the 2009 periastron passage while filled in points are from the 2001 passage.

phase. This bin size preserves overall trends within the data, but specific details of the absorption feature, such as the exact location of the minimum and both maxima, are lost. As expected, the count rate drops as the energy increases. Qualitatively all of the light curves, except that of the 20-60 keV and possibly the 15-20 keV bands, follow the same trends that we described earlier for the 2-10 keV light curve. The 10-15 keV band is the hardest light curve that still has a clear absorption feature near periastron passage.

In order to determine how the AGN discovered by Bikmaev et al. (2008) impacts our light curves, we convert the flux they found (1.6×10^{-11} erg s^{-1} in the 17-60 keV energy range) into a *RXTE* count rate for each of our energy bands using a power low with a photon index of 2, their absorption column density, and the WebPIMMS software (Mukai 1993). Additionally, we account for the collimator's relative transmittance for a source that is off axis for *RXTE* (Figure 4.3 in the *RXTE* technical appendix). We assumed WR 140 was on axis which puts the AGN at 17' off axis and results in approximately 80% transmittance. We display our resulting AGN count rates in Figures 4.7 through 4.9 as a dashed line. In several energy ranges our calculation is a clear overestimate of the AGN contribution. The 7.5-10 keV, 10-15 keV and 15-20 keV light curves all have count rates below what we estimate for the AGN. These same energy bands sometimes includes phase-locked variability that is obviously due to WR 140. Our overestimate is possibly at least partially due to the fact that we extrapolated the X-ray count rates to energies much lower than those in which the AGN X-ray flux was measured.

The 20-60 keV range shows an estimated AGN count rate that is consistent with the observed count rate regardless of phase. In this band the AGN count rate is a fair estimate because the X-ray flux was measured in a band with almost the same

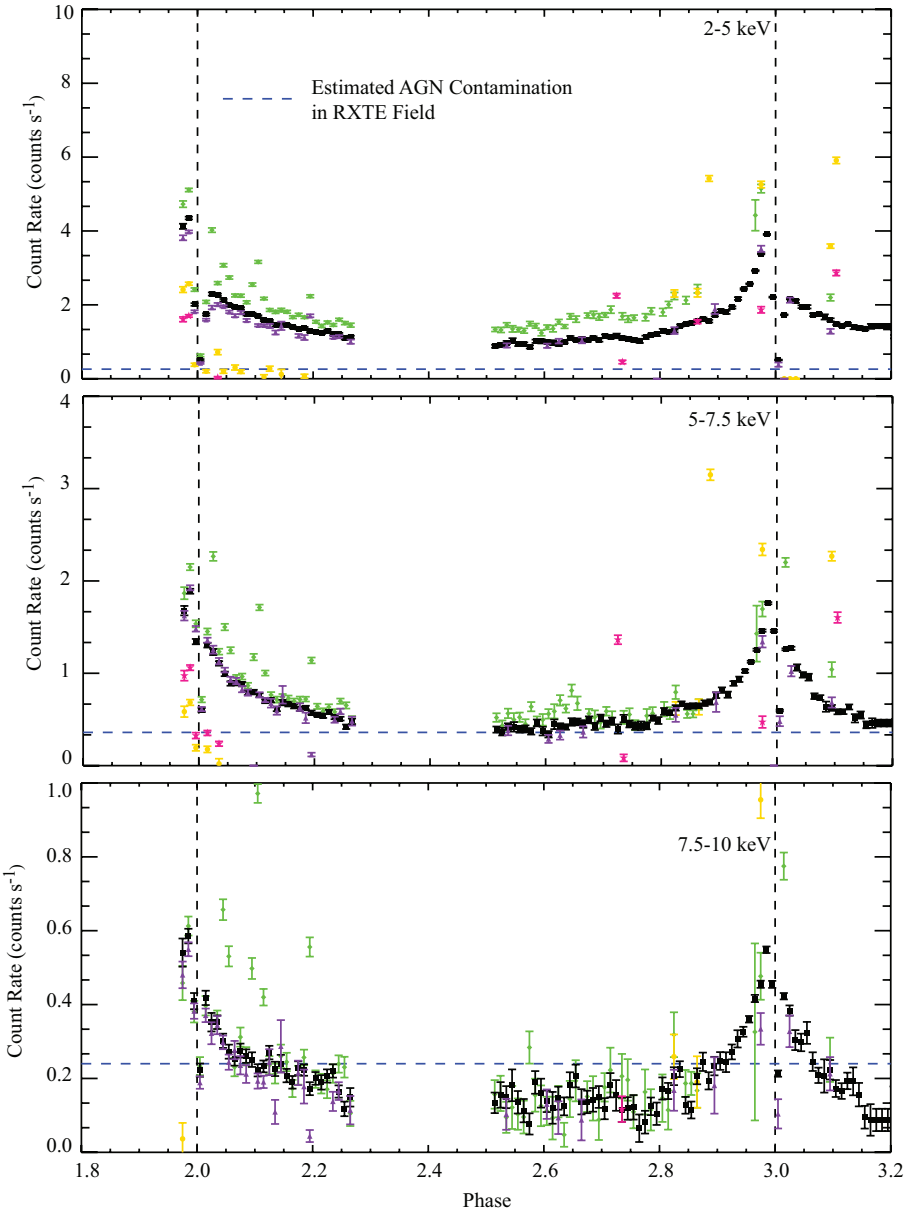

Figure 4.8 X-ray count rate from the *RXTE* observations. *From top:* 2-5 keV, 5-7.5 keV, 7.5-10 keV. Colors and point styles represent the different PCU's within the PCA instrument (green diamonds=PCU0, yellow circles=PCU1; black squares=PCU2; pink stars=PCU3; and purple triangles=PCU4). Vertical dotted lines indicate periastron passages (2001 passage is at phase 1.0 and the 2009 passage is at phase 3.0). Dashed blue horizontal lines represent the estimated AGN contamination in the *RXTE* field for WR140. Observations are binned to 0.01 in phase.

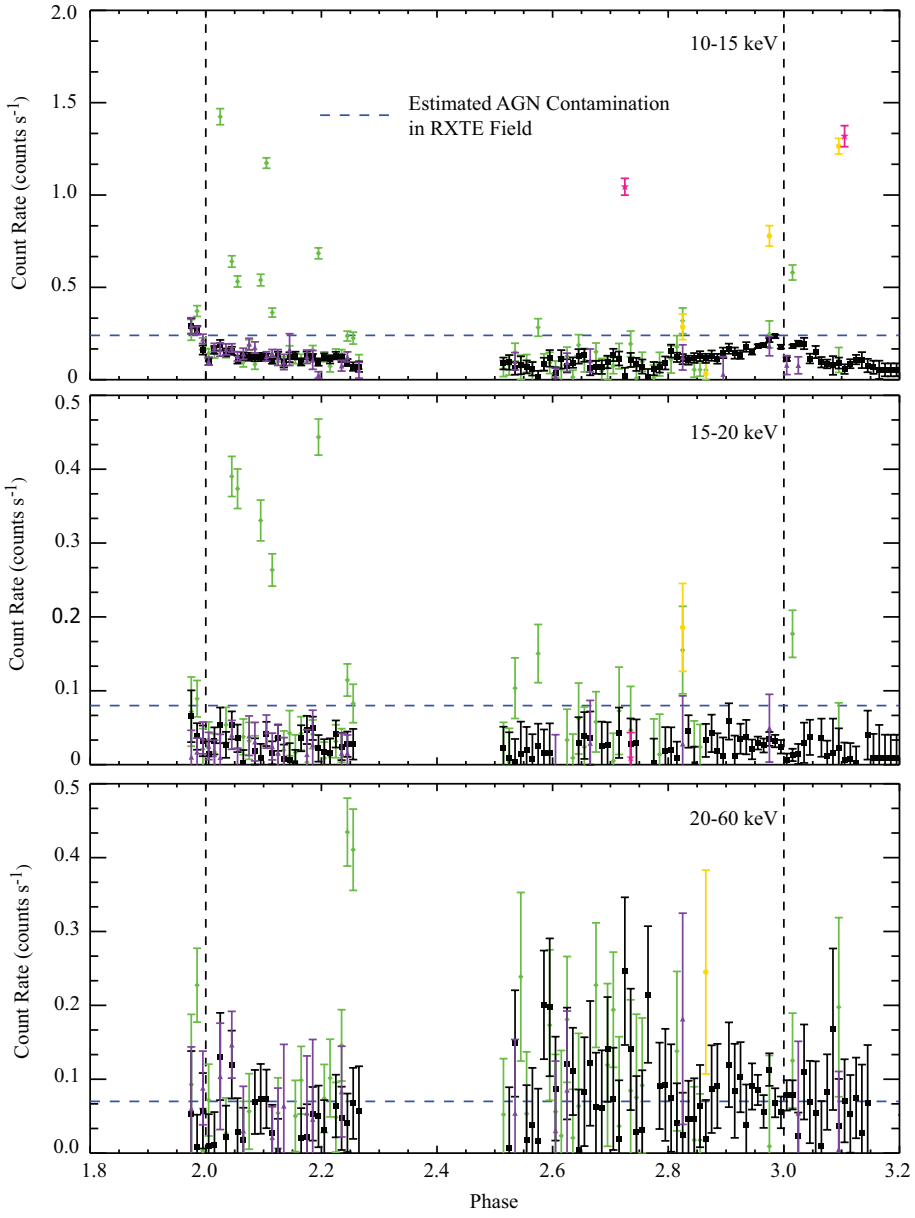

Figure 4.9 Same as Figure 4.7. *From top:* 10-15 keV, 15-20 keV, 20-60 keV.

energy range. Additionally, the light curve shows no phase-dependent variations, although the uncertainties are lower near phase 3.0 (2009 periastron passage) due to the large number of observations conducted in a small amount of time resulting in better statistics. We therefore conclude that in the 20-60 keV band all of the observed X-rays are due to contamination from the AGN.

We discuss the behavior of these light curves more in Section 4.5.1 where we compare their results with the results of the spectral fitting.

4.4.3 Optical Polarimetry

In order to explore the polarimetric variability seen in WR140 by Schulte-Ladbeck et al. (1995) we combined their observations with those taken by Robert et al. (1990) since they have never been compared before. Figure 4.10 shows all of these observations. In general, the variations within each data set are at a 0.1–0.15% level in percent polarization. The Lyot data have a greater amount of scatter, closer to 0.2%. Similar overall trends appear in the position angle for the system. The Lyot data have a greater scatter (on the order of 10°) than the other data (close to 5°). In Stokes % Q each data set shows a different amount of scatter (HPOL$\approx$ 0.15%; MINIPOL$\approx$ 0.1%; Lyot$\approx$ 0.4%), however, in the Stokes % U parameter they all scatter by about the same amount.

We calculated the error-weighted mean and standard deviation for the HPOL data since that instrument has low errors and is well characterized. Other data were not included due to concerns over comparison between instruments and because the optical wavelength ranges covered by the each instrument are slightly different. Not surprisingly, the mean position angle is the same as the ISP estimate from Schulte-Ladbeck et al. (1995). They used the HPOL observations to calculate their ISP

estimate due to their relatively constant trend compared to the Lyot data. Several Lyot and MINIPOL observations deviate significantly from the HPOL data. All of these deviations are within the first two years after the 1985 periastron passage. This suggests that those variations are linked to processes that occur during that passage. We feel that this deviation is real and not an instrumental stability issue since it occurs in bot the Lyot and MINIPOL data. In Section 4.5.2 we discuss possible processes responsible for the polarimetric variations.

We also explored the possibility of the emission lines being polarized in the HPOL data, but found they are polarized the same as the continuum. This suggests either that the lines are polarized by electron scattering like the continuum or that interstellar polarization dominates the observed polarization signal. A combination of both scenarios could also explain this result.

4.5 Discussion

4.5.1 Intrinsic Hard X-ray Flux Absorption?

Our observations show hard X-ray emission that has a phase dependent behavior (Figure 4.9). This raises the question of whether that emission turns off near periastron or is just absorbed. In order to better answer this question, we calculated the width of the absorption feature for each of the light curves in Figures 4.8 and 4.9 without binning using the PCU2 data. We did not include the 20-60 keV band because of its constant behavior. If WR 140's hard X-ray component does not turn off and is absorbed near periastron the width of the absorption feature should decrease with energy. This is because hard X-rays are not as readily absorbed as soft

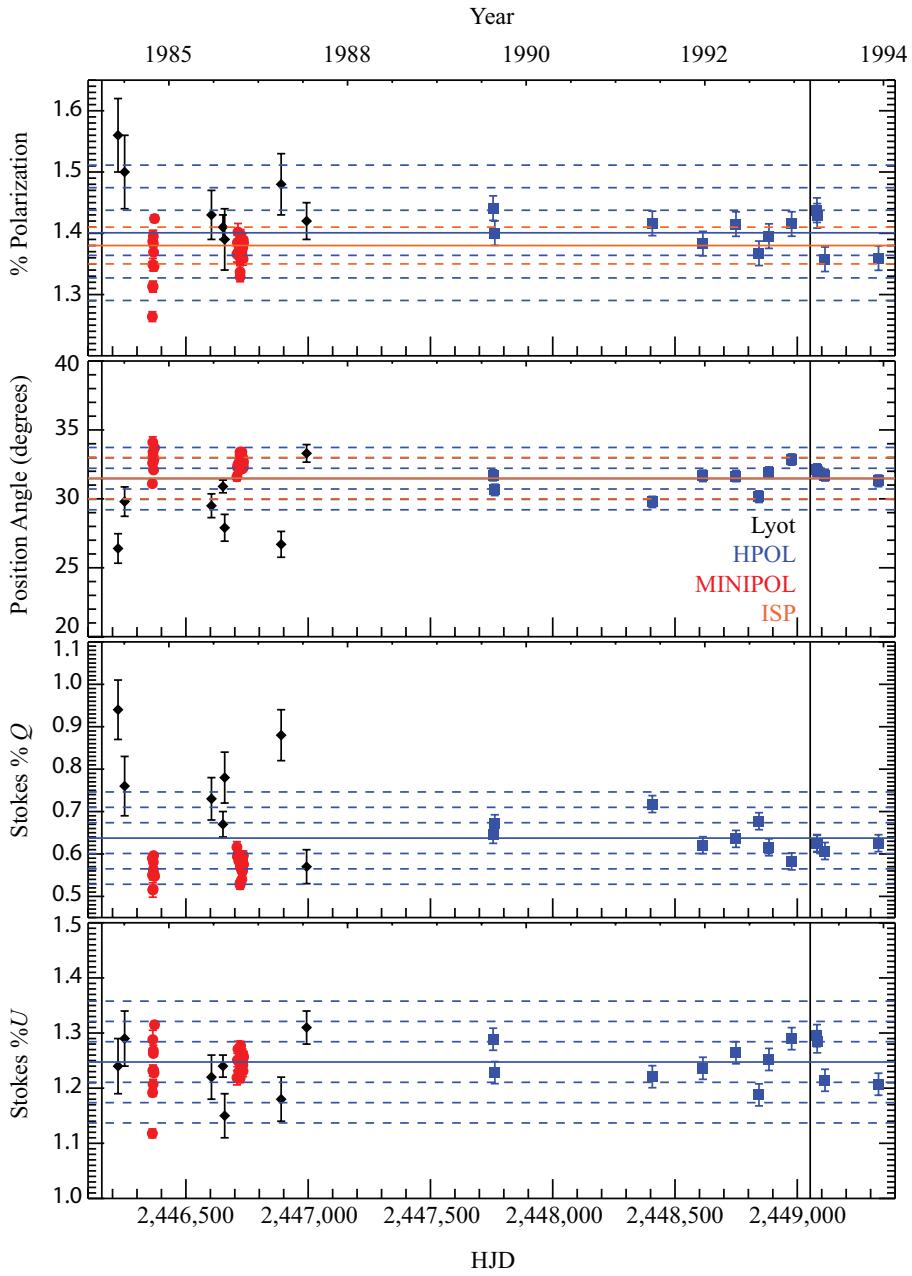

Figure 4.10 Broadband polarimetric variability of WR 140. *From Top:* Percent polarization, position angle, Stokes $\%Q$, and Stokes $\%U$ with time. All published polarimetric data are shown here (Lyot=black diamonds; HPOL *V* band=blue squares; and MINIPOL=dark red). Solid vertical lines mark the 1985 and 1993 periastron passages. Solid horizontal blue lines mark the HPOL error-weighted mean polarization, position angle, Stokes $\%Q$, and Stokes $\%U$ values. Dashed blue lines mark one, two, and three standard deviations from those error weighted means for their respective panels. In the top two panels, we display the ISP estimate in orange given by Schulte-Ladbeck et al. (1995) derived from the HPOL data and their errors (dashed).

X-rays, so the phase interval where the column density is high enough to cause a significant absorption of photons at high energies is smaller than at low energies. However, if the hard X-ray emission component intrinsic to WR 140 turns off we expect the width of the absorption feature to have a behavior other than a constant fall off with energy.

Our first method (observational count rate method) of calculating the width of the absorption feature was to simply find the observation with the highest count rate between phases 0.8 and 0.01 (1.8 and 2.01 for the 2001 periastron passage, and 2.8 and 3.01 for the 2009 periastron passage) and subtract that observation's phase from the phase of the observation with the highest count rate in the 0.01 to 0.06 phase range (2.01 to 2.06 for 2001; 3.01 to 3.06 for 2009). We did not calculate formal uncertainties on the results but do note that during the 2001 periastron passage observations were conducted weekly, and in 2009 daily. We display the results (open squares) of this calculation in Figure 4.11. In general they show a trend that decreases with energy, suggesting that the high energy component's variability is due to absorption. However, because we are simply choosing the observation with the highest count rate, this method could artificially lengthen or shorten the calculated width of the absorption feature if an observation is significantly different than the global trend. Therefore, we used a second method (Fourier fit method) to calculate the width as well.

In this case we performed a Fourier fit with the Period04 program (Lenz & Breger 2005) to the PCU2 data to represent the overall trend of the light curves. Since we are only interested in the region around periastron passages, we did not concern ourselves with how well these fits matched data outside of the region near periastron. We then calculated the width of the absorption feature by finding the

phase difference of the first maxima on either side of the minimum. Additionally, we could only perform Fourier fits for energy bands where the data were good enough; lack of observations and high uncertainties prevented us from being able to fit the 15-20 keV data and the 2001 10-15 keV periastron passage. Again, we did not calculate formal uncertainties for these width estimates. We display the data and Fourier fits of the regions around periastron passage for those bands that we were able to fit in Figure 4.12. The resulting widths are displayed as filled diamonds in Figure 4.11. Using this method, we found that the width of the absorption feature is constant between 5 and 15 keV. This suggests that there is some intrinsic hard X-ray emission that does not turn off. However, the data also match the large-scale downward trend of the 2001 widths which may suggest the true trend for the Fourier fit method is also decreasing with energy.

The results of our spectral fitting only complicate the issue further. If the parameters in the power law component of the fit were strictly fitting the AGN behavior as we assumed, the normalization should not show phase-dependent behavior. However, Figure 4.6 clearly shows that the 2001 and 2009 periastron passages exhibit similar behavior, indicating the variations are due to WR 140; it is highly unlikely that the AGN is variable on the same timescale as WR 140. Thus, the phase-dependent variations are likely caused by a high energy inverse Compton scattering component (as opposed to contamination from the low energy thermal tail which should show a trend that appears as the inverse of the thermal normalization).

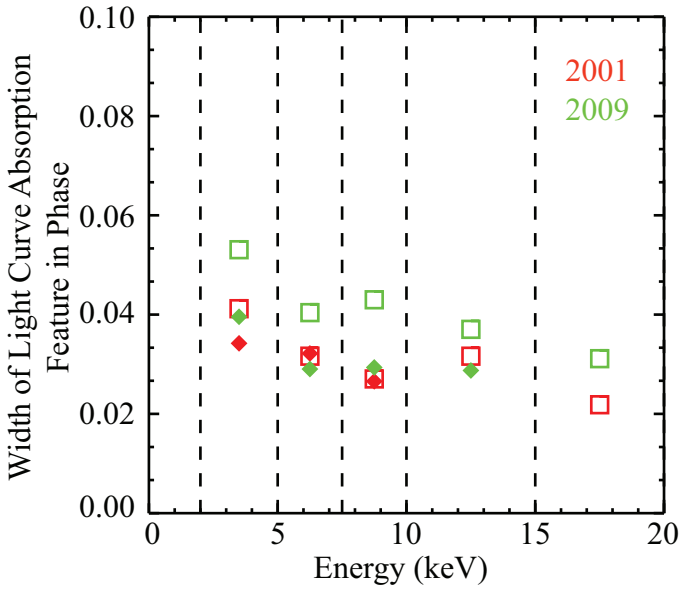

Figure 4.11 Width of the absorption feature in different energy bands (Figures 4.8 and 4.9). Dotted vertical lines mark the edges of the energy bands used that correspond to our light curves in Section 4.4.2. Open symbols represent the width of the feature calculated from the highest observational count rate method while filled symbols used the Fourier fit method (Section 4.5.1). Red points represent the 2001 periastron absorption feature while green points are from the 2009 periastron.

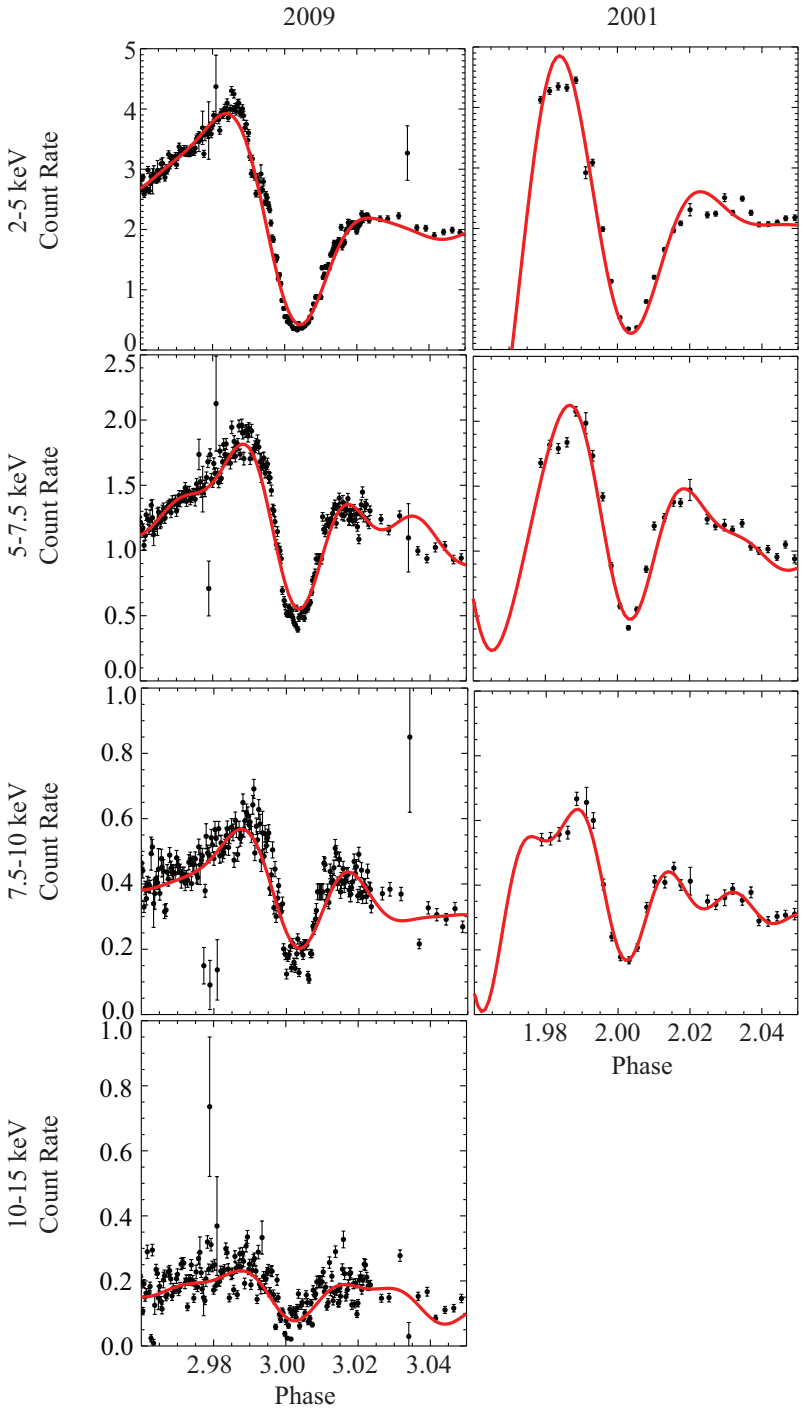

Figure 4.12 Light curves of the bands for which Fourier fits were performed. The first column is the 2009 periastron passage and the second column is data from the 2001 periastron passage. Data points and their respective uncertainties are depicted in black while Fourier fits are red curves.

4.5.2 Cause of the Polarization

The steady behavior seen in our polarimetric observations can be caused by several different scenarios. Schulte-Ladbeck et al. (1995) assumed that all of the polarization observed by the HPOL instrument must be due to the interstellar medium. However, it would be hard to distinguish that from a scenario in which interstellar polarization contributes but electron scattering within the system also causes a constant polarimetric behavior especially if the emission lines are scattered in the same manner as the continuum. Unfortunately, WR 140 does not have good probe stars nearby to help determine the interstellar polarization component of the observed polarization.

Schulte-Ladbeck et al. (1995) suggested that the variability seen in their Lyot data was due to dust scattering within clouds receding from the system after periastron passage. This is constant with infrared observations that show the formation and ejection of dust from the system just after periastron passage (Williams et al. 2009) and infrared light curves that also show evidence of dust (Taranova & Shenavrin 2011). Regular polarimetric monitoring with a higher cadence than the Lyot and HPOL data is needed to better understand the nature of the dust within the WR 140 system, particularly around periastron passage.

4.6 Summary

We have presented the results of eleven years worth of monitoring efforts of WR 140 using *RXTE*. Spectral and light curve analysis of those data provide evidence for the nature of the hard X-rays detected from the system. They may be due inverse

Compton scattering of UV photons to X-ray energies within the shock (Section 4.5.1).

The variability of the polarization after the 1985 periastron passage suggests that light is scattering in dust clouds. In order to better understand the formation and ejection of dust from WR 140 regular polarimetric monitoring of the system is needed.

Chapter 5

Conclusions and Future Work

5.1 Beta Lyrae

New modeling efforts have also inferred the presence of a hot spot in the β Lyr system since the publication of Chapter 2 (Lomax et al. 2012, Mennickent & Djurašević 2013). Additionally, the system was used as a prototype for a theoretical study of the evolution of binaries undergoing mass transfer (Deschamps et al. 2013). In light of these new results I discuss possible follow-up investigations of the β Lyrae system below. These are aimed at better understanding the multiwavelength behavior of the system and the relationship between the outflows and hot spot.

5.1.1 Can we confirm the hot spot interpretation?

In Chapter 2, I discussed the results of my spectropolarimetric study of β Lyr which indicated the presence of a hot spot on the disk (Lomax et al. 2012). The hot spot acts to randomize the polarization arising from the disk edge and manifests itself as a secondary minimum in polarization that is not centered on phase 0.5.

More recent results accurately reproduce the total light curve of the β Lyr system only when a hot spot is included on the disk edge (Mennickent & Djurašević 2013). In fact, the location of the hot spot derived by (Mennickent & Djurašević 2013; near phase 0.4) is consistent with the location I found in Chapter 2 (approximately at phase 0.47), and their size estimate (26 $R_{\odot}$) falls in the middle of the size range derived by (Lomax et al. 2012; 22-33 $R_{\odot}$). In order to match the light curve, their proposed hot spot must be hotter than the ambient disk temperature as expected for a region of the disk that likely has deceleration shocks. They find that the hot spot with a temperature of 9900 K and a disk edge temperature 8200 K best reproduce the total light curve. Mennickent & Djurašević (2013) also conclude that a second hot spot must exist on the opposite side (near phase 0.8) covering 30% of the disk.

Beta Lyr is a known X-ray source; both *ROSAT* HRI and *Suzaku* have detected strong and variable emission from the system (Berghofer & Schmitt 1994, Ignace et al. 2008). However, neither set of observations has provided information on the origin of the X-ray emission. The *Suzaku* observations of β Lyr were aimed at constraining the flux variations from the system. This data set consists of three observations of approximately 14 ksec each taken in the same epoch but at different phases. Surprisingly, emission below 10 keV shows no eclipse effects and is largely attributed to shocks in the winds of the two stars within the β Lyr system (Ignace et al. 2008). Perhaps even more interesting is the detection of a variable hard X-ray source within the system (Table 5.1; Ignace et al. 2008). The observation with the highest observed hard X-ray count rate occurred at phase 0.55 when, according to the model I proposed in Chapter 2, the hot spot should be most visible (Lomax et al. 2012). Intense heating of the gas in the hot spot is expected to occur due to deceleration shocks; however, the hot spot temperature of 9900 K found by

Mennickent & Djurašević (2013) is much too low to account for any of the X-ray emission observed from the system. A complete X-ray light curve of the system will provide important information about any relationship between the hot spot and the variable hard X-rays, in addition to providing better statistics to determine the actual variability and location of the hard X-ray emitting region within β Lyr. We have proposed for such observations in the past with *Suzaku*, but have yet to gain X-ray observing time. We plan to propose for them again.

Table 5.1: β Lyr 10-60 keV *Suzaku* Count Rate

Phase	**Exposure (ks)**	**Count Rate (cps)**	**Background (cps)**
0.55	14.7	0.623± 0.007	0.536± 0.002
0.91	17.0	0.505± 0.005	0.509± 0.002
0.24	14.1	0.573± 0.006	0.564± 0.002

Note. – Table 3 from Ignace et al. (2008). The observation at phase 0.55 detected a higher count rate than the others, possibly arising from the hot spot in the β Lyr system.

5.1.2 Line Polarimetry Follow-Up Observations

Deschamps et al. (2013) recently performed evolutionary modeling of several different systems, one of which has β Lyr as its prototype. In their modeling, they consider the effects of hot spots on gainer stars which may help to accelerate material out of binary systems through the formation of jets. In this specific analysis, Deschamps et al. (2013) only consider cases where the mass stream impacts and

disrupts the secondary star's photosphere; however an impact on the edge of an accretion disk, such as I hypothesized in Chapter 2 could produce similar outflows (Lomax et al. 2012). The outflows in β Lyr are not well constrained, but may originate from the hot spot (see Chapter 2, Section 2.5.4 for a discussion of this idea; Lomax et al. 2012). However, Deschamps et al. (2013) admit that the connection between hot spots and outflows is not observationally well constrained for any system and that it is unknown whether material in these hot spot originating outflows reach speeds high enough to be ejected from a system.

More spectropolarimetric observations of β Lyr can go a long way toward confirming a connection between the hot spot and outflows in this system. If the outflows do originate from the hot spot, higher signal-to-noise observations would show an offset secondary eclipse in the light curve of the polarized lines. A polarized secondary eclipse in the emission lines occurring after the eclipse in total light would be consistent with the location of the hot spot inferred by my analysis in Chapter 2 (Lomax et al. 2012). Additionally, the analysis of the polarized lines in Chapter 2 suggests that the outflows do not extend far above and below the disk, so that this material may not be ejected from the system. If this is the case, Deschamps et al. (2013)'s assumption that the material in the jets formed by hot spots is eventually removed from the system may not be valid for systems similar to β Lyr. Additional spectropolarimetric observations, particularly around secondary eclipse so that it is well covered, can also address this issue because they can determine the size of the scattering region within outflows. We can conduct these new observations with longer exposures with the new HPOL at Ritter Observatory or propose for time on the Keck spectropolarimeter at specific phases.

5.2 V444 Cyg

It is apparent from Chapter 3 that new, detailed studies of the V444 Cyg system are warranted. Below I outline the next steps my collaborators and I plan on taking to better understand the physical processes governing the behavior of the winds and wind collision region in the system.

5.2.1 Complete X-ray light curve of the system

Currently, the light curve is fairly well characterized, but the observations that covered the second half of the orbit (see Chapter 3; revolution numbers 2272, 2275, 2283, and 2292) revealed unexpected behavior. In particular, we expected to see asymmetric eclipse effects at phase 0.5, not a peak in the soft X-rays at phase 0.63 and a hard eclipse centered on phase 0.55. Since these results were surprising, full coverage of the system's X-ray light curve is needed to make sure the behavior of the system is well understood.

In light of this, I plan to propose for another *XMM-Newton* observation, that would cover the entire orbit of the system in the next observing cycle. The results of that observation will allow my collaborators and me to determine which of the variations are cycle-to-cycle as opposed to repeatable and what, if any, other important behavior is missing from the current light curve. For example, observation number 0692810401 (revolution 2272; purple in Figures 3.3 and 3.4) does not appear to trend toward observation 0692810501 (revolution 2283; dark green in those same figures) in the hard X-ray light curve. The new observation will allow us to determine whether this is because we are missing an important piece of the light

curve (for example, it may flatten out between the two observations) or whether this behavior is just due to stochastic variations.

5.2.2 X-ray Modeling

Clearly modeling of the X-ray data is needed. Future plans to model the system by one of my collaborators, Christopher Russell at the University of Delaware, will further determine the extent to which radiative processes affect the location of the shock and in turn the observed the X-ray behavior of the system. He will be using both smoothed particle hydrodynamics and finite-difference codes to model the system in three dimensions synthesize the continuum and line X-ray properties from the colliding wind shocks. This will provide a better determination of the location of the apex of the shock cone, the amount of distortion due to the Coriolis force, and quantify the effects of radiative braking on the system. This is part of the NASA ADAP project (grant number NNH12ZDA001N) for which we were awarded funding in 2012.

5.2.3 Spectropolarimetric Observations and Modeling

The results of Chapter 3 suggest that more spectropolarimetric observations of the system are needed in order to better understand the geometry of the shock and WN-star wind. Currently the polarized light curve of the emission lines have poor phase coverage, especially around phase 0.5 where interesting effects are seen in the broadband polarization (Robert et al. 1989, St.-Louis et al. 1993) and poor signal to noise. In particular, observations with higher wavelength resolution will be useful for understanding the polarimetric behavior of blended lines by resolving polari-

metric line profiles. Polarimetric line profile variations near the phases where the polarimetric behavior changes (phases 0.3 and 0.7, Chapter 3) would be particularly interesting. A study of this type would provide valuable insight into the locations of the line scattering regions since many of the lines have varying emission and absorption components in total light due to the winds, shock, and photospheres in the system. My collaborators and I could propose for these types of observations with the Keck spectropolarimeter or HiVIS.

Future planned modeling of the V444 Cyg system by my collaborators, Jennifer Hoffman and Hilding Neilson, will allow us to determine the relative contributions of the different scattering regions to the measured polarization signal (WN-star wind versus wind collision region). Additionally, it can provide and independent determination of the opening angle of the system. We plan on accomplishing this by using three dimensional Monte Carlo techniques that include a shock geometry.

5.3 WR 140

The potentially contradicting results of the *RXTE* observations of WR 140 make it apparent that further study of the system is needed, particularly in regards to the possible existence of hard ($>$ 10 keV) X-ray emission from the system. In the following sections I discuss a soon-to-be-published study of WR 140 whose results will help shed light on the question of hard X-ray emission from the system. Additionally, I suggest that polarimetric monitoring of the system is needed.

5.3.1 Hard X-ray Emission?

The only observatories besides *RXTE* capable of reaching hard X-ray wavelengths are *Suzaku*, *Swift*, and *NuSTAR*. My collaborators and I expect that once the results from *Suzaku* observations from the 2009 periastron passage are published (with the AGN taken into account) they will provide interesting new results in terms of the possible existence of hard X-ray emission in the system. Future observations of the next periastron passage (in 2017) will also help to clear up this question.

5.3.2 Higher Cadence Polarimetric Monitoring

Future polarimetric monitoring of the system could be used to help determine the nature of the dust near periastron passage. Observations need to have a much higher cadence than previous studies which likely missed much of the variation from the 1985 periastron passage and all of the 1993 variations. Of particular importance are the few months around periastron where the system is undergoing quick changes.

If the dust truly is the only source of variable polarization from the system, then the phases leading up to periastron passage should only be important for determining the constant baseline. Observations once a month for several months prior to periastron passage would provide a sufficient cadence for such a measurement. However, after periastron, dust is known to form and change quickly. Williams et al. (2009) suggest that the dust nucleation is complete by phase 0.03 and that the morphology of the dust changes quickly thereafter. Daily observations for the first month or so after periastron would catch the formation of dust blobs in action and

determine when they are first detectable through polarimetric methods. After this, weekly or biweekly observations of the system until at least phase 0.35 would provide adequate coverage for a polarimetric study of the changing morphology of the dust. Since broadband polarimetry would be sufficient for these types of observations an instrument such as HPOL could be used for the follow-up.

5.4 Overall Conclusions

Correlating the multiwavelength behavior of massive binary stars forms a detailed picture of the characteristics of their interactions. This kind of information is important to understanding the physics behind mass and angular momentum loss from systems. Since most massive stars are in binary systems (see Chapter 1), our inadequate understanding of the details of these processes is no longer acceptable if we want to truly understand massive star evolution.

Orbital motion is an important factor in the formation of the mass-loss structures in all three systems I have studied as part of this dissertation. In the case of β Lyr, orbital motion helps control the location of the hot spot by influencing the location of the mass stream relative to the disk in the system. Even stronger effects are seen in V444 Cyg and WR 140. The stellar motion in V444 Cyg causes a distortion of the wind collision region due to Coriolis forces and the high eccentricity of WR 140 causes the shock structure to continually change over the course of an orbit. It is obvious that orbital motion cannot be ignored if we are to understand the details of mass loss structures.

Studying more systems in the same manner that I have for my dissertation will provide a statistical approach to understanding how differences in mass transfer

rates, orbital motions, and mass loss rates affect the structures of material within binary systems. By studying other β Lyrae-like systems we can start to answer questions like the following: What is the rate of occurrence of accretion hot spots due to mass transfer in Roche-lobe overflow systems? Is there a mass transfer rate cutoff below which hot spots do not form, and if so what is it? How important is the density of the disk for the formation of a hot spot? That is, do denser disks have a higher occurrence of hot spots than less dense disks? What is the lower limit on the density for a formation of a hot spot? Similar questions can be asked of systems like WR 140. What causes eccentric colliding wind binaries to not produce X-ray luminosity that is inversely proportional to their separation? Does the $\frac{1}{D}$ relationship only hold for certain separation ranges? Additionally, it is important to study other systems similar to V444 Cyg to determine the importance of processes like radiative braking and inhibition in close colliding wind binaries. Below I identify other important objects which should be studied in order to begin answering these questions.

5.4.1 Additional Objects

Beta Lyrae-Like: V356 Sgr, V367 Cyg

V356 Sgr is a Roche-lobe overflow system with a A2 supergiant (12 $M_{\odot}$) star which is transferring mass to its brighter B-type companion (5 $M_{\odot}$). Unlike beta Lyrae its disk is optically thin, its period is shorter (8.89 days), and its mass transfer rate is lower (approximately 10^{-7} $M_{\odot}$ yr^{-1}). A University of Denver (DU) team has recently determined that the system shows two polarized flux eclipses in contrast to β Lyr's one (Malatesta et al. 2013). This suggests that either a circumbinary disk

surrounds both stars in the system or the mass stream is an important scattering region in the system. Currently, there are not enough data to look for a polarimetric signature of a hot spot on the disk edge, but future observations will help in this respect.

V367 Cyg is another system which will be of importance in answering the questions I outlined above. It is likely made up of an A and a B-type star (22 $M_{\odot}$ + 11 $M_{\odot}$) with an 18 day period and close to edge on inclination (Elias 1993). Circumbinary material exists in a ring around the system which is undergoing Roche-lobe overflow. Significant archival HPOL observations exist (66) which could also be used for determining the occurrence rate of hot spots. Analysis of these data are underway at DU to characterize the ISP and compare the data to the results for Elias (1993) (J.L. Hoffman, priv. comm.).

Other Colliding Wind Binaries: WR 133, CQ Cep

WR 133's high eccentricity (0.39, 112 day period) is reminiscent of the very eccentric (e = 0.88) WR 140 system whose expected X-ray brightness deviates from the $\frac{1}{D}$ behavior near periastron (Corcoran et al. 2011). WR 133 is also comparable to WR 11. Both systems have periods (WR 11 is about 80 days) and despite high eccentricities (e = 0.3 for WR 11). WR 11 does not follow the $\frac{1}{D}$ behavior (Schild et al. 2004). Explaining why these systems do and do not show an X-ray luminosity that is dependent on binary separation is a significant challenge and currently there is no explanation for this behavior. Determining WR 133's intrinsic X-ray luminosity variation as a function of the separation of the two stars is important for determining whether the X-ray emission from the wind collision region is qualitatively similar to emission we see from WR 140 (X-ray emission inversely proportional to

stellar separation except near periastron) or the X-ray emission from WR 11 (which show no separation dependence). The new information provided by an X-ray study of the system will begin to reveal the physics responsible for the consistency of the X-ray emission in this class of WR+O systems and be a significant step toward explaining the lack of intrinsic X-ray variations. This can be accomplished by using *XMM-Newton* or *Suzaku* to observe the system several times over the course of it's orbit.

CQ Cep is a colliding stellar wind system that has not been observed in X-rays other than one detection by *ROSAT* (Pollock et al. 1995, Marchenko et al. 2003). It is has a short 1.6-day period. Obtaining an X-ray light curve (again, using something like *XMM-Newton* or *Suzaku*) to supplement the existing polarimetric light curves of the system will allow us to probe both the hot wind collision region and the warm gas to better understand the movement of material and its loss from another close, short period system (Villar-Sbaffi et al. 2005, Harries & Hilditch 1997).

RY Scuti: An Important Transition Object

RY Scuti is in an important phase of its evolution. It is believed to be a direct progenitor of a V444 Cyg-like system currently undergoing Roche-lobe overflow (Smith et al. 2002). It has recently undergone mass ejection events suggesting that even a concrete understanding of Roche-lobe overflow is not enough to determine how these systems evolve to colliding wind binaries (Smith et al. 2001). With that in mind, it is important to investigate all types of mass loss and transfer, not just those studied in this dissertation, in order to understand the processes that effects

the future evolution of binary systems. Only then will their role in the formation of supernovae and their affects on the enrichment of the ISM be clear.

As a long term project, studying RY Scuti and systems like it with multiwavelength techniques would provide detailed clues to how systems evolve from Roche-lobe overflow states to colliding wind binaries. Eruptive events, like what formed the rings around RY Scuti, between these evolutionary phases of relatively constant mass loss may be important and mass lost from such events should not be ignored if we want to thoroughly understand the massive binary star evolutionary sequence.

Chapter 6

Bibliography

Abt, H. A., Jeffers, H. M., Gibson, J., & Sandage, A. R. 1962, ApJ, 135, 429

Ak, H., et al. 2007, A&A, 463, 233

Aldering, G., Humphreys, R. M., & Richmond, M. 1994, AJ, 107, 662

Anders, E., & Grevesse, N. 1989, Geochim. Cosmochim. Acta, 53, 197

Appenzeller, I. 1965, ApJ, 141, 1390

Appenzeller, I., & Hiltner, W. A. 1967, ApJ, 149, 353

Arnaud, K. A. 1996, Astronomical Data Analysis Software and Systems V, 101, 17

Berghofer, T. W., & Schmitt, J. H. M. M. 1994, A&A, 292, L5

Bhatt, H., Pandey, J. C., Kumar, B., Singh, K. P., & Sagar, R. 2010, MNRAS, 402, 1767

Bikmaev, I. F., Burenin, R. A., Revnivtsev, M. G., et al. 2008, Astronomy Letters, 34, 653

Bisikalo, D. V., Harmanec, P., Boyarchuk, A. A., Kuznetsov, O. A., & Hadrava, P. 2000, A&A, 353, 1009

Bouret, J.-C., Lanz, T., & Hillier, D. J. 2005, A&A, 438, 301

Brown, J. C., McLean, I. S., & Emslie, A. G. 1978, A&A, 68, 415

Castor J.I. 1987, Instabilities in Luminous Early-Type Stars, 159

Chandrasekhar, S. 1960, New York: Dover, 1960,

Cherepashchuk, A. M., Khaliullin, K. F., & Eaton, J. A. 1984, ApJ, 281, 774

Corcoran, M. F., Stevens, I. R., Pollock, A. M. T., et al. 1996, ApJ, 464, 434

Corcoran, M. F., Pollock, A. M. T., Hamaguchi, K., & Russell, C. 2011, arXiv:1101.1422

De Becker, M., Pittard, J. M., Williams, P., & WR140 Consortium 2011, Bulletin de la Societe Royale des Sciences de Liege, 80, 653

De Greve, J. P., & Doom, C. 1988, A&A, 200, 7

De Greve, J. P., & Linnell, A. P. 1994, A&A, 291, 786

De Loore, C., De Greve, J. P., & Lamers, H. J. G. L. M. 1977, A&A, 61, 251

de Mink, S. E., Pols, O. R., & Glebbeek, E. 2007, Unsolved Problems in Stellar Physics: A Conference in Honor of Douglas Gough, 948, 321

de Mink, S. E., Pols, O. R., Langer, N., & Izzard, R. G. 2009, A&A, 507, L1

de Mink, S. E., Pols, O. R., Langer, N., & Izzard, R. G. 2010, IAU Symposium, 266, 169

Deschamps, R., Siess, L., Davis, P. J., & Jorissen, A. 2013, arXiv:1306.1348

Dougherty, S. M., & Williams, P. M. 2000, MNRAS, 319, 1005

Dougherty, S. M., Beasley, A. J., Claussen, M. J., Zauderer, B. A., & Bolingbroke, N. J. 2005, ApJ, 623, 447

Eichler, D., & Usov, V. 1993, ApJ, 402, 271

Elias, N. M., II 1993, ApJ, 410, 785

Elias, N. M., II, Koch, R. H., & Holenstein, B. D. 1996, BAAS, 28, 913

Elias, N. M., II, Jones, C. E., Schmitt, H. R., Jorgensen, A. M., Ireland, M. J., & Perraut, K. 2008, arXiv:0811.3139

Eriş, F. Z., & Ekmekçi, F. 2011, Astronomische Nachrichten, 332, 616

Fahed, R., Moffat, A. F. J., Zorec, J., et al. 2011, MNRAS, 418, 2

Fauchez, T., De Becker, M., & Nazé, Y. 2011, Bulletin de la Societe Royale des Sciences de Liege, 80, 673

Flores, A., Auer, L. H., Koenigsberger, G., & Cardona, O. 2001, ApJ, 563, 341

Forbes, D. 1981, PASP, 93, 441

Fullerton, A. W., Massa, D. L., & Prinja, R. K. 2006, ApJ, 637, 1025

Gaskell, C. M., Cappellaro, E., Dinerstein, H. L., et al. 1986, ApJ, 306, L77

Gayley, K. G., Owocki, S. P., & Cranmer, S. R. 1997, ApJ, 475, 786

Gies, D. R., & Lambert, D. L. 1992, ApJ, 387, 673

Goodricke, J., & Englefield, H. C. 1785, Royal Society of London Philosophical Transactions Series I, 75, 153

Hamann, W.-R., & Schwarz, E. 1992, A&A, 261, 523

Harmanec, P., & Scholz, G. 1993, A&A, 279, 131

Harmanec, P., et al. 1996, A&A, 312, 879

Harmanec, P. 2002, Astronomische Nachrichten, 323, 87

Harries, T. J., & Hilditch, R. W. 1997, MNRAS, 291, 544

Harries, T. J., Hillier, D. J., & Howarth, I. D. 1998, MNRAS, 296, 1072

Heger, A., Langer, N., & Woosley, S. E. 2000, ApJ, 528, 368

Hellings, P. 1983, Ap&SS, 96, 37

Hillier, D. J. 1991, A&A, 247, 455

Hirv, A., Annuk, K., Eenmäe, T., et al. 2006, Baltic Astronomy, 15, 405

Hoffman, J. L., Nordsieck, K. H., & Fox, G. K. 1998, AJ, 115, 1576

Hoffman, J. L., Whitney, B. A., & Nordsieck, K. H. 2003, ApJ, 598, 572

Holenstein, B. D. 1991, Ph.D. Thesis

Horne, J. H., & Baliunas, S. L. 1986, ApJ, 302, 757

Huang, S.-S. 1963, ApJ, 138, 342

Hubeny, I., & Plavec, M. J. 1991, AJ, 102, 1156

Iben, I., Jr. 1991, ApJS, 76, 55

Ignace, R., Oskinova, L. M., Waldron, W. L., Hoffman, J. L., & Hamann, W.-R. 2008, A&A, 477, L37

Izzard, R. G., Ramirez-Ruiz, E., & Tout, C. A. 2004, MNRAS, 348, 1215

Kasen, D., Nugent, P., Thomas, R. C., & Wang, L. 2004, ApJ, 610, 876

Kippenhahn, R., & Weigert, A. 1967, ZAp, 65, 251

Koenigsberger, G., & Auer, L. H. 1985, ApJ, 297, 255

Krause, O., Birkmann, S. M., Usuda, T., et al. 2008, Science, 320, 1195

Kron, G. E., & Gordon, K. C. 1950, ApJ, 111, 454

Kurosawa, R., Hillier, D. J., & Pittard, J. M. 2002, A&A, 388, 957

Kurucz, R. L., Peytremann, E., & Avrett, E. H. 1974, Washington : Smithsonian Institution : for sale by the Supt. of Docs., U.S. Govt. Print. Off., 1974.,

Lauterborn, D. 1970, A&A, 7, 150

Lemaster, M. N., Stone, J. M., & Gardiner, T. A. 2007, ApJ, 662, 582

Lenz, P., & Breger, M. 2005, Communications in Asteroseismology, 146, 53

Leyder, J.-C., Walter, R., & Rauw, G. 2010, A&A, 524, A59

Li, Q.-K., Cassinelli, J. P., Brown, J. C., & Ignace, R. 2009, Research in Astronomy and Astrophysics, 9, 558

Linnell, A. P., Hubeny, I., & Harmanec, P. 1998, ApJ, 509, 379

Linnell, A. P. 2000, MNRAS, 319, 255

Lomax, J. R., Hoffman, J. L., Elias, N. M., II, Bastien, F. A., & Holenstein, B. D. 2012, ApJ, 750, 59

Lubow, S. H., & Shu, F. H. 1975, ApJ, 198, 383

Lupie, O. L., & Nordsieck, K. H. 1987, AJ, 93, 214

Maeda, Y., Koyama, K., Yokogawa, J., & Skinner, S. 1999, ApJ, 510, 967

Malatesta, M., Lomax, J. R., & Hoffman, J. L. 2013, American Astronomical Society Meeting Abstracts, 221, #144.18

Marchenko, S. V., Moffat, A. F. J., & Koenigsberger, G. 1994, ApJ, 422, 810

Marchenko, S. V., Moffat, A. F. J., Eenens, P. R. J., Hill, G. M., & Grandchamps, A. 1995, ApJ, 450, 811

Marchenko, S. V., Moffat, A. F. J., Eenens, P. R. J., et al. 1997, ApJ, 485, 826

Marchenko, S. V., Moffat, A. F. J., Ballereau, D., et al. 2003, ApJ, 596, 1295

Maund, J. R., Smartt, S. J., Kudritzki, R. P., Podsiadlowski, P., & Gilmore, G. F. 2004, Nature, 427, 129

Mennickent, R. E., & Djurašević, G. 2013, MNRAS, 432, 799

Meynet, G., & Maeder, A. 2000, A&A, 361, 101

Mihalas, D. 1978, San Francisco, W. H. Freeman and Co., 1978. 650 p.,

Moffat, A. F. J., Firmani, C., McLean, I. S., & Seggewiss, W. 1982, Wolf-Rayet Stars: Observations, Physics, Evolution, 99, 577

Moffat, A. F. J. 2008, Clumping in Hot-Star Winds, 17

Monnier, J. D., Tuthill, P. G., & Danchi, W. C. 1999, ApJ, 525, L97

Mukai, K. 1993, Legacy, vol. 3, p.21-31, 3, 21

Nazarenko, V. V., & Glazunova, L. V. 2006, Astronomy Reports, 50, 369

Nazé, Y. 2009, A&A, 506, 1055

Nelemans, G., Voss, R., Nielsen, M. T. B., & Roelofs, G. 2010, MNRAS, 405, L71

Nieuwenhuijzen, H., & de Jager, C. 1990, A&A, 231, 134

Nomoto, K., Suzuki, T., Shigeyama, T., et al. 1993, Nature, 364, 507

Nomoto, K. I., Iwamoto, K., & Suzuki, T. 1995, Phys. Rep., 256, 173

Nook, M. A., Cardelli, J. A., & Nordsieck, K. H. 1990, AJ, 100, 2004

Nordsieck, K. H., & Harris, W. 1996, Polarimetry of the Interstellar Medium, 97, 100

Nugis, T. 1996, Liege International Astrophysical Colloquia, 33, 283

Öhman, Y. 1934, Nature, 134, 534

Oskinova, L. M. 2005, MNRAS, 361, 679

Owocki, S., Castor, J. I., & Rybicki, G. B. 1987, Sixth International Solar Wind Conference, 177

Owocki, S. P., & Gayley, K. G. 1995, ApJ, 454, L145

Owocki, S. P., & Puls, J. 1999, ApJ, 510, 355

Packet, W. 1981, A&A, 102, 17

Paczynski, B. 1976, Structure and Evolution of Close Binary Systems, 73, 75

Parkin, E. R., & Gosset, E. 2011, A&A, 530, A119

Parkin, E. R., & Sim, S. A. 2013, ApJ, 767, 114

Peel, M. 1997, MNRAS, 284, 148

Pittard, J. M., & Stevens, I. R. 1999, Wolf-Rayet Phenomena in Massive Stars and Starburst Galaxies, 193, 386

Pittard, J. M. 2002, Interacting Winds from Massive Stars, 260, 627

Pittard, J. M., & Parkin, E. R. 2010, MNRAS, 403, 1657

Podsiadlowski, P., Joss, P. C., & Hsu, J. J. L. 1992, ApJ, 391, 246

Podsiadlowski, P., Hsu, J. J. L., Joss, P. C., & Ross, R. R. 1993, Nature, 364, 509

Poelarends, A. J. T., Herwig, F., Langer, N., & Heger, A. 2008, ApJ, 675, 614

Pollock, A. M. T. 1985, Space Sci. Rev., 40, 63

Pollock, A. M. T. 1987, ApJ, 320, 283

Pollock, A. M. T., Haberl, F., & Corcoran, M. F. 1995, Wolf-Rayet Stars: Binaries; Colliding Winds; Evolution, 163, 512

Pollock, A. M. T., Corcoran, M. F., Stevens, I. R., & Williams, P. M. 2005, ApJ, 629, 482

Puls, J., Markova, N., Scuderi, S., et al. 2006, A&A, 454, 625

Robert, C., Moffat, A. F. J., Bastien, P., Drissen, L., & St.-Louis, N. 1989, ApJ, 347, 1034

Robert, C., Moffat, A. F. J., Bastien, P., St.-Louis, N., & Drissen, L. 1990, ApJ, 359, 211

Roxburgh, I. W. 2004, A&A, 428, 171

Russell, C. M. P., Corcoran, M. F., Okazaki, A. T., Madura, T. I., & Owocki, S. P. 2011, Bulletin de la Societe Royale des Sciences de Liege, 80, 719

Ryder, S. D., Murrowood, C. E., & Stathakis, R. A. 2006, MNRAS, 369, L32

Sana, H., de Mink, S. E., de Koter, A., et al. 2012, Science, 337, 444

Schild, H., Güdel, M., Mewe, R., et al. 2004, A&A, 422, 177

Schmitt, H. R., et al. 2009, ApJ, 691, 984

Schonberner, D., Herrero, A., Becker, S., et al. 1988, A&A, 197, 209

Schulte-Ladbeck, R. E., Nordsieck, K. H., Bjorkman, K. S., Meade, M. R., & Babler, B. L. 1995, Wolf-Rayet Stars: Binaries; Colliding Winds; Evolution, 163, 506

Serkowski, K. 1965, ApJ, 142, 793

Shakhovskoi, N. M. 1963, Soviet Astronomy, 6, 587

Shore, S. N., & Brown, D. N. 1988, ApJ, 334, 1021

Shulov, O. S. 1967, Proc. Astr. Obs. Leningrad Univ., 24, 38

Skulskii, M. Y. 1992, Soviet Ast.Letters, 18, 287

Smartt, S. J. 2009, ARA&A, 47, 63

Smith, N., Gehrz, R. D., & Goss, W. M. 2001, AJ, 122, 2700

Smith, N., Gehrz, R. D., Stahl, O., Balick, B., & Kaufer, A. 2002, ApJ, 578, 464

Smith, N., & Owocki, S. P. 2006, ApJ, 645, L45

Smith, N., Li, W., Filippenko, A. V., & Chornock, R. 2011, MNRAS, 412, 1522

Stevens, I. R., Blondin, J. M., & Pollock, A. M. T. 1992, ApJ, 386, 265

Stevens, I. R., & Pollock, A. M. T. 1994, MNRAS, 269, 226

St.-Louis, N., Moffat, A. F. J., Lapointe, L., et al. 1993, ApJ, 410, 342

Stokes, G. G. 1852, Trans. Camb. Philos. Soc., 9, 399

Sugawara, Y., Maeda, Y., Tsuboi, Y., et al. 2011, Bulletin de la Societe Royale des Sciences de Liege, 80, 724

Sweet, I. P. A., & Roy, A. E. 1953, MNRAS, 113, 701

Sytov, A. Y., Kaigorodov, P. V., Bisikalo, D. V., Kuznetsov, O. A., & Boyarchuk, A. A. 2007, Astronomy Reports, 51, 836

Taranova, O. G., & Shenavrin, V. I. 2011, Astronomy Letters, 37, 30

Thorne, K. S., & Zytkow, A. N. 1975, ApJ, 199, L19

Tuthill, P. G., Monnier, J. D., & Danchi, W. C. 1999, Nature, 398, 487

Underhill, A. B., & Fahey, R. P. 1987, ApJ, 313, 358

Usov, V. V. 1992, ApJ, 389, 635

van der Hucht, K. A. 2001, New A Rev., 45, 135

Villar-Sbaffi, A., St-Louis, N., Moffat, A. F. J., & Piirola, V. 2005, ApJ, 623, 1092

Wellstein, S., Langer, N., & Braun, H. 2001, A&A, 369, 939

Whitney, B. A., & Clayton, G. C. 1989, AJ, 98, 297

Wilkin, F. P. 2000, ApJ, 532, 400

Wilking, B. A., Lebofsky, M. J., & Rieke, G. H. 1982, AJ, 87, 695

Williams, P. M., van der Hucht, K. A., Pollock, A. M. T., et al. 1990, MNRAS, 243, 662

Williams, P. M., Marchenko, S. V., Marston, A. P., et al. 2009, MNRAS, 395, 1749

Wilson, R. E. 1974, ApJ, 189, 319

Wilson, R. E., & van Hamme, W. 1999, MNRAS, 303, 736

Wolff, M. J., Nordsieck, K. H., & Nook, M. A. 1996, AJ, 111, 856

Woosley, S. E., Eastman, R. G., Weaver, T. A., & Pinto, P. A. 1994, ApJ, 429, 300

Zhao, M., et al. 2008, ApJ, 684, L95

Zhekov, S. A., & Skinner, S. L. 2000, ApJ, 538, 808